

**THE INFLUENCE OF TISSUE SPECIFIC CARDIAC AND SKELETAL MUSCLE  
EXTRACELLULAR MATRIX ON MUSCLE REMODELING**

by

Matthew Thomas Wolf

Bachelor of Science in Bioengineering, University of Pittsburgh, 2008

Submitted to the Graduate Faculty of  
Swanson School of Engineering in partial fulfillment  
of the requirements for the degree of  
Doctor of Philosophy

University of Pittsburgh

2014

UNIVERSITY OF PITTSBURGH  
SWANSON SCHOOL OF ENGINEERING

This dissertation was presented

by

Matthew Thomas Wolf

It was defended on

December 19, 2013

and approved by

Stephen F. Badylak, DVM, PhD, MD, Professor, Department of Surgery

Fabrisia Ambrosio, PhD, MPT, Assistant Professor, Department of Physical Medicine and

Rehabilitation

Sanjeev Shroff, PhD, Professor, Department of Bioengineering

William R. Wagner, PhD, Professor, Department of Surgery

Douglas J. Weber, PhD, Associate Professor, Department of Bioengineering

Dissertation Director: Stephen F. Badylak, DVM, PhD, MD, Professor, Department of

Surgery

Copyright © by Matthew Thomas Wolf

2014

**THE INFLUENCE OF TISSUE SPECIFIC CARDIAC AND SKELETAL MUSCLE  
EXTRACELLULAR MATRIX ON MUSCLE REMODELING**

Matthew Thomas Wolf, PhD

University of Pittsburgh, 2014

Volumetric muscle loss (VML) in skeletal muscle and loss of cardiac function after myocardial infarction lack viable treatment options for functional tissue restoration. Previously investigated strategies such as synthetic graft placement and cell therapy are limited in their ability to restore function to these tissues. Biologic scaffolds composed of extracellular matrix (ECM) have been prepared from numerous source tissues including small intestine, urinary bladder, liver, and dermis. When properly prepared, ECM scaffolds implanted into a site of injury are rapidly infiltrated by host cells, subjected to degradation, and often remodel into site appropriate host tissue. The ECM of tissues and organs represents the secreted products of resident cells, a process which provides a unique microenvironmental niche that influences cell behavior during homeostasis and injury. The objective of the present study was to develop and characterize muscle tissue specific scaffolds composed of skeletal (M-ECM) and cardiac muscle (C-ECM), and to determine whether a muscle tissue ECM scaffold preferentially promotes muscle restoration compared to non-muscle ECM.

A method of skeletal and cardiac muscle decellularization was developed that efficiently removed cells while preserving native ECM components, including basement membrane proteins, glycosaminoglycans, and growth factors. Degradation products produced by pepsin digestion of M-ECM, C-ECM, and non-muscle ECM derived from small intestinal submucosa (SIS-ECM) decreased proliferation and promoted the myogenic differentiation of perivascular

stem cells *in vitro*. Although M-ECM was more rapidly degraded than both C-ECM and SIS-ECM, all ECM scaffolds showed a similar increase in functional skeletal myogenesis.

These studies show that M-ECM and C-ECM can be prepared in a manner that preserves muscle ECM specific components and biologic activity. M-ECM promoted stem cell myogenic activity in a non-tissue specific manner *in vitro*, and both muscle and non-muscle ECM promoted functional myogenesis to a similar extent *in vivo*. These results indicate that M-ECM is not a preferred substrate for skeletal muscle remodeling compared to C-ECM and SIS-ECM.

## TABLE OF CONTENTS

<b>TABLE OF CONTENTS .....</b>	<b>VI</b>
<b>LIST OF TABLES .....</b>	<b>X</b>
<b>LIST OF FIGURES .....</b>	<b>XI</b>
<b>PREFACE.....</b>	<b>XVII</b>
<b>1.0 INTRODUCTION.....</b>	<b>1</b>
<b>1.1 SKELETAL AND CARDIAC MUSCLE INJURY .....</b>	<b>1</b>
<b>1.1.1 Clinical incidence and significance of muscle injury.....</b>	<b>1</b>
<b>1.1.2 Skeletal muscle injury response .....</b>	<b>3</b>
<b>1.1.3 Cardiac muscle injury response .....</b>	<b>7</b>
<b>1.2 EXTRACELLULAR MATRIX (ECM) AS A BIOLOGIC SCAFFOLD .....</b>	<b>9</b>
<b>1.2.1 The role of ECM in tissues and organs.....</b>	<b>9</b>
<b>1.2.2 ECM as a biologic scaffold.....</b>	<b>10</b>
<b>1.2.3 Clinical applications of ECM scaffolds.....</b>	<b>12</b>
<b>1.3 TISSUE SPECIFIC ECM SCAFFOLDS IN TISSUE ENGINEERING .....</b>	<b>14</b>
<b>1.3.1 The tissue specific ECM hypothesis .....</b>	<b>14</b>
<b>1.3.2 Considerations in evaluating ECM tissue specificity .....</b>	<b>14</b>
<b>1.3.3 Studies that support a tissue specific hypothesis .....</b>	<b>16</b>
<b>1.3.4 Studies that do not support a tissue specific hypothesis.....</b>	<b>21</b>
<b>1.3.5 Limitations in determining ECM tissue specificity .....</b>	<b>24</b>

<b>1.4</b>	<b>HYPOTHESIS AND SPECIFIC AIMS.....</b>	<b>25</b>
1.4.1	Motivation and central hypothesis.....	25
1.4.2	Specific aim 1 .....	26
1.4.3	Specific aim 2 .....	26
1.4.4	Specific aim 3 .....	27
<b>2.0</b>	<b>DEVELOPMENT AND CHARACTERIZATION OF A BIOLOGIC SCAFFOLD COMPOSED OF SKELETAL AND CARDIAC MUSCLE EXTRACELLULAR MATRIX .....</b>	<b>28</b>
<b>2.1</b>	<b>INTRODUCTION .....</b>	<b>28</b>
<b>2.2</b>	<b>METHODS.....</b>	<b>30</b>
2.2.1	Overview of experimental design .....	30
2.2.2	Skeletal muscle decellularization protocol .....	31
2.2.3	Conventional small intestine decellularization and muscle decellularization method.....	32
2.2.4	Verification of muscle decellularization .....	33
2.2.5	Scanning electron microscopy .....	34
2.2.6	Cell culture and metabolism on M-ECM scaffolds .....	34
2.2.7	Acute evaluation of an M-ECM scaffold in a rat abdominal wall defect model.....	36
2.2.8	Protein extraction and growth factor quantification .....	37
2.2.9	ECM staining and immunolabeling .....	38
2.2.10	Sulfated glycosaminoglycan quantification.....	39
2.2.11	Statistical analysis.....	39
<b>2.3</b>	<b>RESULTS .....</b>	<b>40</b>
2.3.1	Verification of decellularization .....	40
2.3.2	Scanning electron microscopy .....	41
2.3.3	Cell culture and metabolism on M-ECM scaffolds .....	44

2.3.4	Acute evaluation of an M-ECM scaffold in a rat abdominal wall defect model.....	48
2.3.5	Application of the skeletal muscle decellularization method to cardiac and small intestine tissues.....	51
2.3.6	Protein extraction and growth factor quantification .....	52
2.3.7	ECM staining and immunolabeling .....	53
2.3.8	Sulfated glycosaminoglycan quantification.....	58
2.4	DISCUSSION.....	59
3.0	THE EFFECT OF SKELETAL AND CARDIAC MUSCLE EXTRACELLULAR MATRIX DEGRADATION PRODUCTS ON SKELETAL AND CARDIAC MUSCLE PERIVASCULAR STEM CELLS.....	65
3.1	INTRODUCTION .....	65
3.2	METHODS.....	67
3.2.1	Overview of experimental design .....	67
3.2.2	Preparation of ECM degradation products .....	67
3.2.3	Skeletal and cardiac perivascular stem cell (PVSC) isolation and culture conditions.....	69
3.2.4	PVSC myogenic differentiation.....	70
3.2.5	BrdU incorporation assay for PVSC proliferation.....	73
3.2.6	Statistical analysis.....	77
3.3	RESULTS .....	77
3.3.1	PVSC myogenic differentiation.....	77
3.3.2	BrdU incorporation assay for PVSC proliferation.....	83
3.4	DISCUSSION.....	85
4.0	COMPARISON OF ECM SCAFFOLDS PREPARED FROM SKELETAL AND CARDIAC MUSCLE FOR TREATMENT OF VOLUMETRIC MUSCLE LOSS IN A RODENT MODEL.....	91
4.1	INTRODUCTION .....	91

<b>4.2</b>	<b>METHODS</b> .....	<b>93</b>
4.2.1	Overview of experimental design .....	93
4.2.2	Tissue decellularization and device preparation .....	93
4.2.3	Surgical creation of the VML defect and ECM device implantation .....	95
4.2.4	Histologic analysis of ECM remodeling in a VML defect.....	97
4.2.5	Electromyography (EMG) of innervated muscle in the VML defect .....	99
4.2.6	Statistical analysis.....	102
<b>4.3</b>	<b>RESULTS</b> .....	<b>102</b>
4.3.1	Histologic analysis of ECM remodeling in a VML defect.....	102
4.3.2	Electromyography (EMG) of innervated muscle in the VML defect .....	110
<b>4.4</b>	<b>DISCUSSION</b> .....	<b>114</b>
<b>5.0</b>	<b>SYNOPSIS, CONCLUSIONS, AND FUTURE DIRECTIONS</b> .....	<b>121</b>
<b>5.1</b>	<b>SYNOPSIS</b> .....	<b>121</b>
<b>5.2</b>	<b>CONCLUSIONS</b> .....	<b>123</b>
<b>5.3</b>	<b>FUTURE DIRECTIONS</b> .....	<b>123</b>
5.3.1	Hydrogel formulations of M-ECM and C-ECM .....	123
5.3.2	ECM/Synthetic “biohybrid” devices for cardiac repair .....	126
<b>APPENDIX A. IMAGEJ SCRIPT USED FOR BRDU QUANTIFICATION</b> .....		<b>129</b>
<b>BIBLIOGRAPHY</b> .....		<b>134</b>

## LIST OF TABLES

Table 1. Examples of clinical products composed of decellularized tissues. ....	13
Table 2. Summary of each ECM group's tissue source and the decellularization method. ....	30
Table 3. Summary of the steps in the decellularization of skeletal muscle tissue including the chemical treatment and time of exposure. ....	32

## LIST OF FIGURES

- Figure 1. Overview of the mammalian muscle regeneration cascade following injury. Muscle injury activates quiescent Pax7+ stem cells to undergo asymmetric division, and produce proliferative MyoD+ myoblasts. Myoblasts continue to proliferate, differentiate and align, and fuse to form multinucleate myofibers. The specific time course varies depending upon the extent and type of injury as well as the species in which injury occurs. .... 6
- Figure 2. Residual DNA content of M-ECM scaffolds after decellularization for each batch tested in the study (n=7) compared to native muscle (n=2). Histologic appearance after H&E staining of (A) M-ECM and (B) native muscle tissue, and after DAPI staining of (C) M-ECM and (D) native muscle, bar represents 100  $\mu$ m. The DAPI stained M-ECM is overexposed and imaged multispectrally displaying scaffold autofluorescence as grey and nuclei as blue. (E) Results of the PicoGreen analysis for double stranded DNA extracted per mg dry weight of scaffolds  $\pm$  SD. (F) Extracted DNA from several batches of M-ECM separated via 2% agarose gel electrophoresis and compared with native muscle and a 100 bp ladder. .... 41
- Figure 3. SEM images of M-ECM and native muscle tissue. M-ECM was imaged at (A) 25X, (B) 500X, (C) 1,000X, and (D) 10,000X magnifications and compared to native muscle cross sections at (E) 500X and (F) 5,000X. Long fibrils with a collagen-like banding pattern were observed in the M-ECM scaffold. .... 43
- Figure 4. *In vitro* cell compatibility histology of (A,C) C2C12 myoblasts and (B,D,E) perivascular stem cells cultured for 7 days on the surface of M-ECM (A,B,E) or SIS (C,D). Representative images of (A-D) H&E cross sections and (E) fluorescent imaging labeling with phalloidin for actin (red) or DAPI for nuclei (blue). Scale bar represents 100  $\mu$ m..... 45
- Figure 5. *In vitro* cell compatibility histology of (A-B) NIH 3T3 fibroblasts, (C-D) human microvascular endothelial cells, and differentiated C2C12 myoblasts (E-F) after 7 days of culture on (A,C,E) M-ECM or (B,D,F) SIS sheets. H&E stained. Scale bar represents 100  $\mu$ m..... 46
- Figure 6. Alamar Blue assay for cellular metabolism of (A) C2C12 myoblasts and (B) perivascular stem cells seeded on the surface of M-ECM sheets, SIS sheets, or tissue culture plastic (TC) controls for 1, 3, and 5 days. Results normalized to standard curve of cells assayed on TC 4 hours after seeding. Significance defined as  $p < 0.05$

and \* denotes a difference from day 1 within a group, # denotes a difference from SIS within a timepoint, and † denotes a difference from M-ECM within a timepoint.  
 ..... 47

- Figure 7. *In vivo* response to implanted (A-B,E-F,I-J) M-ECM and (C-D,G-H,K-L) SIS after (A-D) 14 and (E-L) 35 days. Low magnification (100X) images (A,C,E,G,I,K) are presented with black boxes denoting regions of interest for high magnification (400X) images presented directly to the right (B,D,F,H,J,L). Sections were stained with (A-H) Masson’s Trichrome or (I-L) immunolabeled for fast (red) and slow (brown) myosin heavy chain (MHC). There are obvious scaffold remnants at 14 days for both scaffolds (asterisks), and multinucleate cells around M-ECM scaffold regions (arrowheads). Scale bars represent 100  $\mu$ m. .... 49
- Figure 8. Areas of incomplete (A) M-ECM and (B) SIS scaffold degradation after 35 days *in vivo* after Masson’s Trichrome staining. Scattered M-ECM scaffold remnants (asterisks) are apparent in some regions of the defect, but such regions are smaller and more diffuse for SIS. M-ECM scaffold remnants are also associated with multinucleate cells (arrowheads). Scale bar represents 100  $\mu$ m. .... 50
- Figure 9. *In vivo* remodeling response to an unrepaired partial thickness abdominal wall defect after 35 days. Images were acquired at low magnification (A, 100X) with a black box denoting a region of interest for a high magnification (B, 400X) image . Scale bars represent 100  $\mu$ m. .... 51
- Figure 10. Native porcine psoas major skeletal muscle, left ventricle, and small intestine sheets (A-C) were decellularized using the muscle protocol to yield acellular ECM scaffolds (D-F). .... 52
- Figure 11. Biochemical growth factor analysis of M-ECM, C-ECM, SIS-M, and SIS compared to their native tissues. (A) Vascular endothelial growth factor (VEGF) and (B) basic fibroblast growth factor (bFGF) were quantified by ELISA from urea heparin extracted protein. .... 53
- Figure 12. Herovici’s Polychrome staining of native muscle (A), M-ECM (B), C-ECM (C), SIS-M (D), and SIS (E). Type I collagen fibers stain as pink/purple and Type III collagen stains blue. Scale bar represents 100  $\mu$ m. .... 54
- Figure 13. Movat’s Pentachrome staining of native muscle (A), M-ECM (B), C-ECM (C), SIS-M (D), and SIS (E). Dense protein regions stain red and elastin stains black and is highlighted by arrows. Scale bar represents 100  $\mu$ m. .... 55
- Figure 14. Fibronectin immunolabeling of native muscle (A), M-ECM (B), C-ECM (C), SIS-M (D), and SIS (E). Positive staining is indicated by brown ECM staining. Scale bar represents 100  $\mu$ m. .... 56
- Figure 15. Type IV collagen immunolabeling of native muscle (A), M-ECM (B), C-ECM (C), SIS-M (D), and SIS (E). Positive staining is indicated by brown ECM staining and is highlighted with arrows. Scale bar represents 100  $\mu$ m. .... 57

- Figure 16. Laminin immunolabeling of native muscle (A), M-ECM (B), C-ECM (C), SIS-M (D), and SIS (E). Positive staining is indicated by brown ECM staining and is highlighted with arrows. Scale bar represents 100  $\mu\text{m}$ . ..... 58
- Figure 17. Sulfated GAG content of each ECM scaffold following enzymatic digestion. (\*) indicates a difference from all other groups ( $p < 0.05$ ). ..... 59
- Figure 18. *In vitro* culture conditions for skeletal and cardiac muscle PVSC myogenic differentiation. PVSCs were plated, grown to confluency, changed to myogenic pre-conditioning media (with and without ECM degradation products) and finally changed to low serum fusion media (with and without ECM degradation products). Cardiac PVSCs were grown to confluence, pulsed with 5-azacytidine, and cultured in high serum cardiac differentiation media (10% FBS). ..... 71
- Figure 19. Summary of *in vitro* culture conditions for PVSC BrdU incorporation assays in serum free (A) and high serum (B) media with or without ECM supplementation. PVSCs in the low serum assay were serum starved for 18 hours and pulsed with ECM and BrdU for the following 18 hours. The high serum assay was conducted in high serum corresponding to the differentiation conditions in the respective skeletal and cardiac muscle differentiation assays. .... 75
- Figure 20. Example outputs of a PVSC seeded well stained and analyzed for BrdU incorporation using a custom ImageJ algorithm. The original mosaic image (A) was split into blue and green color channels, processed, and size gated to count the number of nuclei (B) and BrdU staining nuclei (C) from the ImageJ output mask images. Only blue/green colocalized masks were counted as positive BrdU incorporation (D). ... 76
- Figure 21. The initial skeletal and cardiac muscle PVSC phenotype prior to myogenic differentiation conditions. PVSCs co-expressed pericyte markers CD146 (A) and NG2 (B), while not expressing MyoD (C), GATA4 (D), or sarcomeric MHC (E). Scale bar represents 100  $\mu\text{m}$ . ..... 78
- Figure 22. Skeletal muscle PVSC expression of GATA4 and MyoD following differentiation without ECM. Nearly all cells expressed GATA4 (A-B, green), while there was only extremely rare expression of MyoD (C-D, green). These results were also typical following each ECM treatment. Nuclei were labeled with DAPI (blue). Scale bars represent 100  $\mu\text{m}$ . ..... 79
- Figure 23. Cardiac MHC expression (green) in skeletal muscle PVSCs following differentiation in pepsin control buffer (A), ECM degradation products (M-ECM (B), C-ECM (C), SIS (D), and SIS-M (E)), or purified Type I collagen (F). Nuclei were labeled with DAPI (blue). Scale bar represents 100  $\mu\text{m}$ . ..... 80
- Figure 24. Fast skeletal muscle MHC expression (green) in skeletal muscle PVSCs following differentiation in pepsin control buffer (A), ECM degradation products (M-ECM (B), C-ECM (C), SIS (D), and SIS-M (E)), or purified Type I collagen (F). Nuclei stained with DAPI (blue). Scale bar represents 100  $\mu\text{m}$ . ..... 81

- Figure 25. Skeletal muscle PVSC fusion analysis using sarcomeric MHC expression after exposure to pepsin buffer, M-ECM, C-ECM, SIS-M, or SIS degradation products, or Type I collagen. Fused cells (A, green) were analyzed for total number of fused MHC+ cells (B), total nuclei within MHC+ cells (C), and total MHC+ cell area (D). Statistically significant differences were determined by two-way ANOVA ( $p < 0.05$ ) and denoted with (\*). Scale bar represents 100  $\mu\text{m}$ . ..... 82
- Figure 26. Cardiac PVSCs did not express mature myogenic markers. Scale bar represents 100  $\mu\text{m}$ . ..... 83
- Figure 27. BrdU incorporation in skeletal muscle (A) and cardiac muscle (B) PVSCs with ECM exposure in low serum conditions. Each treatment was applied at 100, 50, and 25  $\mu\text{g/ml}$  concentrations. Values were normalized to untreated cells without ECM or pepsin buffer. Statistically significant differences were determined by two-way ANOVA ( $p < 0.05$ ) and denoted with (\*). Bars over groups of concentrations indicate that there was a difference due to treatment group, but not due to a concentration or interaction effect. .... 84
- Figure 28. BrdU incorporation in skeletal muscle (A) and cardiac muscle (B) PVSCs with ECM exposure in high serum conditions. Statistically significant differences were determined by one-way ANOVA ( $p < 0.05$ ) and denoted with (\*). Each treatment resulted in a significant decrease in BrdU incorporation compared to pepsin buffer control. .... 85
- Figure 29. Schematic representation of the VML model in the mouse quadriceps muscle. The defect (red region) consists of a full thickness resection in the *tensor fascia latae* muscle and a partial thickness resection of the *rectus femoris* in the mouse hindlimb. A size matched ECM particulate device is then implanted within the defect. .... 96
- Figure 30. Representative images of an SIS particulate device with overlaid sheet within the VML defect at the time of implantation. The ECM fills the defect and is held in place with a sheet of ECM sutured at the distal and proximal defect borders. .... 97
- Figure 31. EMG recording setup for evaluating muscle function after 180 days. A schematic (A) of the recording equipment and electrode placement within the quadriceps muscle and a representative image of the electrode placement *in situ* during testing. .... 100
- Figure 32. Representative muscle recruitment curve for uninjured muscle highlighting the recruitment parameters evaluated in this study. The thresholds of stimulation were calculated at the minimum, half maximal, and maximal  $V_{pp}$  amplitude of the CMAP response. Muscle recruitment rate was calculated as the slope of linear region of the recruitment curve. .... 101
- Figure 33. Masson's Trichrome stained images of the VML defect after 56 days. Untreated defects (A) were filled with adipose tissue (white tissue) while the ECM devices (B-E, blue) were still visible and undergoing the remodeling process. All images are oriented such that underlying uninjured quadriceps are along the bottom of each image. Scale bar represents 200  $\mu\text{m}$ . .... 104

- Figure 34. Masson's Trichrome stained images of the VML defect after 180 days. Untreated defects (A) were filled with adipose tissue (white tissue) while the ECM devices (B-E, blue) were still visible and undergoing the remodeling process. All images are oriented such that underlying uninjured quadriceps are along the bottom of each image. Scale bar represents 200  $\mu\text{m}$ . ..... 105
- Figure 35. Desmin immunolabeling (brown) within the VML defect after 56 days. Desmin expressing cells did not migrate from the defect border in untreated animals (A, positive staining represents native tissue), while ECM treatment encouraged desmin positive cell accumulation in the area of remodeling near the ECM periphery (B-E). Each ECM image is located several fields of view away from the defect border, while the untreated image is located in proximity to the border to show that there are no desmin expressing cells migrating from native muscle. Scale bar represents 100  $\mu\text{m}$ . ..... 106
- Figure 36. Fast (pink) and slow (brown) skeletal muscle MHC immunolabeling within the VML defect after 56 days. MHC expressing cells did not migrate from the defect border in untreated animals (A, positive staining represents native tissue), while ECM treatment encouraged desmin positive cell accumulation in the area of remodeling near the ECM periphery (B-E). Each ECM image is located several fields of view away from the defect border, while the untreated image is located in proximity to the border to show that there are no myosin expressing cells migrating from native muscle. Scale bar represents 100  $\mu\text{m}$ . ..... 107
- Figure 37. CD31 expression of blood vessels within the remodeling defect after 14 (A), and 35 days post ECM implantation. These images are representative of all ECM scaffolds. Scale bar represents 100  $\mu\text{m}$ . ..... 108
- Figure 38.  $\beta$ III tubulin staining (green) of nerve fibers within the area of ECM remodeling. Innervation was observed following each ECM treatment including M-ECM (A), C-ECM (B), and SIS-M (C). Both transverse (A,C) and longitudinal nerve sections (B) were observed. Cell nuclei are labeled with DAPI (blue). Scale bar represents 100  $\mu\text{m}$ . ..... 109
- Figure 39. Representative image of non-neuronal  $\beta$ III tubulin expression (green, arrows) in mononuclear cells within the ECM scaffold. Cell nuclei are labeled with DAPI (blue). Scale bar represents 100  $\mu\text{m}$ . ..... 110
- Figure 40. Representative waveforms of the CMAP response (A-B) at increasing nerve stimulation intensities (0.3-2.0 V for uninjured and 2.0-8.0V for untreated) and the averaged recruitment curves for uninjured and untreated VML defects after 180 days. The amplitude of the CMAP waveform at each stimulation intensity was used to generate muscle recruitment curves. The initial biphasic wave before 1 ms represents stimulation artifact. .... 111
- Figure 41. Muscle fiber recruitment parameters from EMG recordings of the CMAP within the VML defect after 180 days. The amplitude of the CMAP response (A) was

calculated as the peak-to-peak voltage ( $V_{PP}$ ) and root mean square voltage ( $V_{RMS}$ ). Muscle recruitment rate was defined as the slope of muscle recruitment during the linear region of the recruitment curve (B). Stimulation efficacy (C) was evaluated as the minimum nerve stimulation intensity required to evoke a minimum threshold, half maximal, and maximal amplitude response from the recruitment curve. Statistically significant differences from untreated animals as determined by Kruskal-Wallis non-parametric analysis of variance (ANOVA) with a post-hoc Mann-Whitney U Test and Sidak correction ( $p < 0.05$ ) are denoted with (\*). No significant differences were found between ECM treatment groups or healthy animals..... 113

Figure 42. C- ECM (A) was prepared by decellularizing intact porcine hearts and then by performing pepsin digestion to prepare degradation products, which could then be used to create a C-ECM hydrogel (B) when brought to physiologic pH and temperature *in vitro*. ..... 125

Figure 43. Rheological characterization of the mechanical properties of M-ECM and UBM hydrogels over time (A) and with varying shear stress frequency (B,C). Pepsin digested ECM was neutralized and brought to 37°C at time 0, and after a brief lag phase, storage modulus ( $G'$ ) rapidly increases, indicating hydrogel formation. The storage and loss modulus ( $G''$ ) was then characterized over a range of oscillatory shear strain frequencies. .... 126

Figure 44. An ECM-PEUU biohybrid device for cardiac repair. (A) PEUU was electrospun concurrently with electrosprayed dermal ECM pepsin digest, which formed an ECM hydrogel component of the device. (B) Electrospinning parameters were optimized to provide anisotropic biaxial mechanical properties such as those seen in the native heart. Images and mechanics courtesy of a collaboration with Dr. Antonio D'Amore and the Wagner lab..... 128

## **PREFACE**

My doctoral studies in the Badylak laboratory have given me a breadth of experiences that were invaluable in my development as a scientist. I was intimately involved with basic science, preclinical studies, translation, clinical implementation, and commercialization aspects of regenerative medicine. Dr. Stephen Badylak, was an exceptional advisor who taught me more than I could have imagined when I started my graduate work at the University of Pittsburgh, and he left me with a unique perspective of medical innovation.

Each and every member of the Badylak lab has been selfless with their time, assistance, and advice, and I could not begin to recount all of those contributions here. Dr. Kerry Daly and Dr. Christopher Dearth were always supportive postdoctoral mentors. Dr. Christopher Carruthers was an exceptional leader, and someone who I could always count on during a hard deadline. Fellow graduate students Brian Sicari, Christopher Medberry, Vineet Agrawal, Lisa Carey, Denver Faulk, Ricardo Londono, and Tim Keane were as friendly and tightly knit of a group of lab members that I have ever been a part of. Former graduate students Drs. Brennan-Pierce, Valentin, Brown, and Wainwright gave me advice and direction during my early years in the lab.

Several funding sources have facilitated my research and training during my graduate career. Much of my training was supported by the NIH-NHLBI training grant (T32-HL76124-6) entitled “Cardiovascular Bioengineering Training Program” through the University of Pittsburgh Department of Bioengineering. Funding for the muscle decellularization optimization work was provided by the Advanced Regenerative Medicine (ARM III) grant W81XWH-07-1-0415 and in

vivo studies provided by the Armed Forces Institute for Regenerative Medicine (AFIRM) grant W81XWH-08-2-0032. Joan Schanck's indomitable spirit and enthusiasm for tissue engineering education and development gave me multiple opportunities to travel and network with other scientists around the country as part of the AFIRM research group.

I would also like to thank those who provided me with much of my technical knowledge of histologic staining and imaging techniques. Jennifer DeBarr, Deanna Rhoads, and Lori Walton of the McGowan Histology Center were invaluable for histologic section preparation, and whose expertise expedited much of this work. I would like to thank the Center for Biologic Imaging at the University of Pittsburgh for access to imaging facilities, and Jonathan Franks for scanning electron micrograph interpretation.

Numerous faculty members at the University of Pittsburgh have been instrumental in not only my education, but also my maturity as a scientist. My first lab experience as an undergraduate was with Dr. Timothy Corcoran of the Division of Pulmonary, Allergy, and Critical Care Medicine laid the foundation for my scientific career. Dr. Corcoran was an incredibly patient and instructive mentor, and I still remember and refer to lessons learned while working under his guidance. Several of my undergraduate professors were also instrumental in my science education. The late Drs. Peter Siska and Alec "Doc" Stewart greatly impacted the way that I view science and education, and their loss will be sorely missed. Faculty in the department of bioengineering including (but not limited to) Drs. Harvey Borovetz, Steve Abramowitch, William Wagner, and Sanjeev Shroff, continued with this tradition of exceptional training in my advanced bioengineering coursework.

I would like to thank my committee members for their guidance and support during my doctoral studies. Each of these members was instrumental in the formation of my dissertation.

But more importantly, each was also a collaborator and mentor. Dr. Ambrosio has been a great collaborator along with postdoctoral fellow Dr. Kristen Stearns in the development and characterization of muscle extracellular matrix scaffolds. Dr. William Wagner was an influential professor, as well as a collaborator in developing ECM/synthetic hybrid devices. Dr. Douglas Weber, despite a busy schedule, was always available to discuss methods and interpretation of electrophysiologic testing. And a special thanks to Dr. Sanjeev Shroff; who has an inspirational enthusiasm for teaching and administered the aforementioned T32 training grant “Cardiovascular Bioengineering Training Program”, (CBTP) that funded much of my training and facilitated unique educational opportunities, notably a clinical internship in electromyography.

My accomplishments in the Badylak lab were in no small part facilitated by undergraduate and rotational students. I have had the opportunity to mentor several students who ultimately made invaluable contributions to my work. Olivia Burnsed, Katie McAndrews, Elizabeth “Abby” Stahl, Stephane Brasseur, and Nicholas Siebenlist are all exceptional and enthusiastic young scientists who are going to have stellar careers of their own.

Last, but definitely not least, I would like to thank my family. My parents Donald and Louise both encouraged me to pursue the biomedical sciences, and were always selfless, caring, and supportive of my decisions. They instilled the importance of scholarship and hard work in life, and these are qualities I will always try to carry with me. I owe all of my opportunities and accomplishments to following their example of perseverance. I would also like to thank my brothers Dan and Chris for all of our experiences together and their support.

## **1.0 INTRODUCTION**

### **1.1 SKELETAL AND CARDIAC MUSCLE INJURY**

#### **1.1.1 Clinical incidence and significance of muscle injury**

Volumetric muscle loss injuries and loss of cardiac function after myocardial infarction are two conditions that currently lack viable treatment options for functional tissue restoration. Coronary heart disease, defined as the narrowing of the coronary vessels that perfuse the heart, currently affects approximately 16.3 million Americans, and is the primary precursor to myocardial infarction. There are 610,000 new myocardial infarctions each year costing \$297 billion in direct and indirect medical costs, reflecting a dire need for effective treatments [1]. Cardiac tissue is irreversibly damaged during infarct events, resulting in a loss of cardiac function, which is then followed by further tissue degeneration in a remodeling process that persists for weeks [2, 3]. Most pharmacological and surgical treatments for infarctions focus on improving coronary perfusion to minimize further damage, and do not directly address restoration of previously lost function. Left ventricle dilation may be mitigated by the placement of a nondegradable synthetic patch (e.g. Dacron or polytetrafluoroethylene), which prevents further dilation but does not restore function [4, 5]. Currently, the only successful treatments for endstage heart failure are heart transplantation or ventricular assist device implantation, though there is a critical shortage

in the number of available donor hearts [6, 7] and assist devices are only able to offer temporary support [8, 9].

Volumetric muscle loss (VML) is defined as the loss of a sufficiently large fraction of a skeletal muscle body such that natural regeneration mechanisms are unable to compensate, resulting in a permanent loss of function [10]. Traumatic injuries such as car accidents and gunshot wounds are frequent causes in the civilian setting [11-14], though surgical removal of large volumes of skeletal muscle during tumor resection or after muscle necrosis due to ischemia may also occur [11, 15]. However, incidences of VML are considerably greater in the active military population where high energy impact trauma to the extremities represent the greatest proportion of combat casualties [10, 16-20]. Advances in body armor have greatly reduced the incidence of fatal penetrating wounds to the chest and abdomen, though as a result, extremity injuries in surviving soldiers have increased. Blast injuries from improvised explosive devices (IEDs) are one such cause [16]. These can be highly dynamic and complex injuries involving multiple tissue types, and in combination with a lack of expedient hospital care on the battlefield, creates the potential for devastating soft tissue loss with significant financial consequences [21-25]. In addition to direct tissue loss from the trauma, VML may occur from indirect conditions such as peripheral compartment syndrome (PCS) in both civilian and military populations [26-30]. PCS develops following muscle trauma, resulting in edema and/or bleeding within the enclosed muscle compartment causing an increase in muscle compartment pressure. This pressure eventually exceeds capillary perfusion pressure, which leads to muscle ischemia and necrosis necessitating muscle removal to salvage the limb [28].

Currently, the most common clinical treatment for extremity muscle loss is a muscle autograft transplant to the injury site, such as a free flap transfer procedure [11, 13, 14, 16-18,

20, 31-33]. However, this treatment is limited by the size of the muscle graft that can be successfully incorporated into the recipient site (innervated and vascularized) without necrosis, functional differences between the donor and recipient muscles, and significant donor site morbidity [31, 32]. Muscle defects in the abdominal wall or diaphragm are often repaired with synthetic, nondegradable mesh materials (e.g. polypropylene or Dacron), though these synthetic materials elicit a chronic foreign body response and fibrosis with no functional recovery of the injured muscle serving only to reinforce the remaining tissue to prevent further damage [34-36].

Both skeletal and cardiac muscle injuries are debilitating and potentially life threatening. The primary function of both tissues on the cellular level is force production, and both tissues possess similar intracellular contractile machinery and regulatory mechanisms to translate neuronal stimuli to usable force. Though how these tissues utilize this force differs considerably. Skeletal muscle is primarily responsible for locomotion, as well as breathing and stabilization; loss function consequently leads to reduced mobility and independence. Cardiac tissue on the other hand, utilizes this force to generate cyclic pressure and flow to maintain blood circulation. Alternative clinical strategies are therefore required to restore meaningful function in both cardiac and skeletal muscle tissues following injury. Regenerative medicine approaches to muscle injury are being investigated to promote new muscle tissue growth rather than only focusing on preventing further tissue damage.

### **1.1.2 Skeletal muscle injury response**

Skeletal muscle regeneration following injury has been well characterized in humans and animals. Unlike other tissues, such as the central nervous system [37, 38], skeletal muscle has a relatively robust regenerative capacity [39, 40], capable of fully recapitulating normal tissue

architecture and function after insult. Established muscle injury models such as cardiotoxin injection, cryoinjury, muscle excision, and muscle crush all progress through similar cellular and molecular events [39]. Skeletal muscle regenerative pathways are well understood to progress through a cascade of differentiation via (1) the activation of resident progenitor cells to commit to a differentiated myogenic lineage, (2) proliferation after activation, (3) further myogenic differentiation and exit from the cell cycle, and finally (4) fusion into functional multinucleate myofibers [39, 40]. These steps are summarized in Figure 1.

The most abundant and well studied muscle progenitor is the satellite cell, which is characterized by the expression of the transcription factor Pax-7 [41-43], and is the primary contributor to new muscle fibers following injury. Quiescent satellite cells reside in a well defined stem cell niche during homeostasis that is located directly between the myofiber cell membrane and the basement membrane of the surrounding extracellular matrix (ECM). Satellite cells are the primary source of myofibers during development and after injury; Pax-7 knockouts are embryonic lethal and lack skeletal muscle formation, and recent reports of conditional Pax-7 ablation in adult tissues completely prevents *de novo* muscle formation, which suggests all myogenic cells are required to proceed through a Pax-7+ state during the differentiation cascade [43-45]. After stimulus (e.g. injury) satellite cells are activated to undergo asymmetric division. One daughter cell retains a relatively undifferentiated state and Pax-7 expression in order to maintain the satellite cell pool, while the other daughter cell will differentiate towards a mature myogenic phenotype, the skeletal muscle myoblast [40, 42, 43, 46-48]. These myoblasts are highly proliferative, and downregulate expression of Pax-7 while upregulating the muscle regulatory transcription factors MyoD and Myf5, adhesion molecules such as M-Cadherin, and cytoskeletal proteins such as desmin, indicating commitment to myogenic differentiation [39-

41]. Myoblasts migrate towards sites of damaged muscle and proliferate extensively in response to mitogenic factors present in the wound environment, which is comprised of immune cell secreted cytokines and chemokines and growth factors secreted by damaged myofibers [49, 50]. Further along the muscle regeneration cascade, myoblasts will exit the cell cycle, downregulate MyoD and Myf5, and upregulate the transcription factor Myogenin as fully committed muscle cells [39-41, 51, 52]. These myogenin+ cells will then align linearly, form cell-cell adhesions with neighboring myogenin+ cells, and finally fuse to the pre-existing damaged myofibers or form *de novo* myofibers. Fusion is accompanied by the expression of the late muscle differentiation transcription factor MRF4, cytoskeletal proteins such as dystrophin and dystroglycan, as well as functional contractile proteins such as sarcomeric myosin and skeletal muscle tropomyosin. Newly formed myofibers initially display nuclei located within the center of the cytoplasm (a remnant of cell fusion), which will eventually migrate towards the myofiber periphery during muscle fiber maturity [39]. Other events during final differentiation include myofiber hypertrophy, maturity of muscle-ECM adhesion complexes for force transmission, and formation of neuromuscular junctions with innervating axons and nervous system control [53, 54]. Indeed, functional innervation and formation of a stable neuromuscular junction is necessary for muscle fiber survival and appropriate phenotype. A lack of muscle fiber innervation and neurologic control results in irregular contractile activity and eventually, muscle atrophy [55].

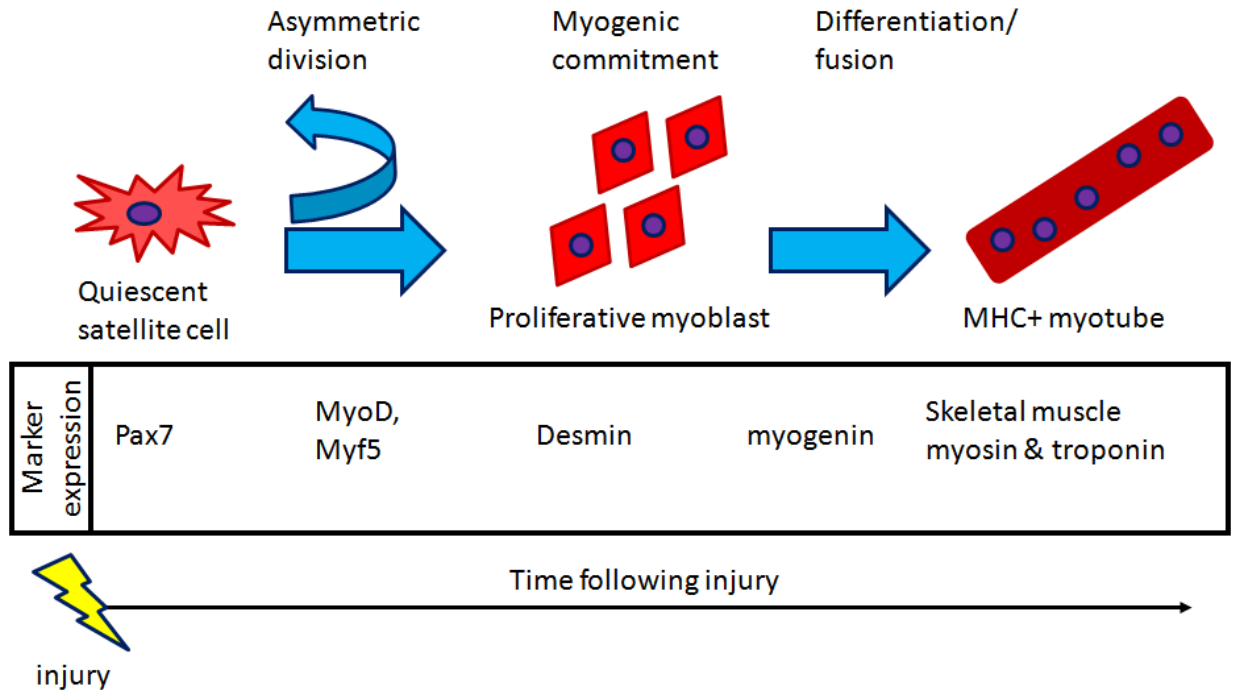


**Figure 1.** Overview of the mammalian muscle regeneration cascade following injury. Muscle injury activates quiescent Pax7+ stem cells to undergo asymmetric division, and produce proliferative MyoD+ myoblasts. Myoblasts continue to proliferate, differentiate and align, and fuse to form multinucleate myofibers. The specific time course varies depending upon the extent and type of injury as well as the species in which injury occurs.

However, there are circumstances where normal muscle regeneration mechanisms are unable to compensate for the injury and muscle regeneration remains incomplete. If the degree of injury is sufficiently large, or if there is significant disruption to the muscle ECM, normal muscle repair mechanisms are inadequate for complete functional restoration [40, 49]. This is true in VML where large muscle masses are removed by trauma or excision, and subsequently only partially replaced with fibrous scar and/or adipose tissue rather than new muscle [10, 50, 56]. Chronic muscle injury, in which small but repeated muscle damage occurs, results in prolonged

tissue healing and scar tissue formation. Certain disease states, such as Duchenne muscular dystrophy, follow this pattern due to the constant muscle injury induced by incomplete myofiber linkage to the ECM [57]. As stated previously, effective muscle repair is dependent on two general cell processes: proliferation of muscle progenitors to create a pool of myogenic cells, and differentiation/fusion to become terminally differentiated and functional myofibers. Either or both of these processes may be potential targets for directing and improving muscle regeneration.

### **1.1.3 Cardiac muscle injury response**

In contrast to skeletal muscle, adult cardiac tissue does not possess a putative progenitor cell type as abundant or functional as the skeletal muscle satellite cell, and does not effectively regenerate following injury. Ischemia from myocardial infarction and resultant left ventricle remodeling is the most well characterized injury response in the heart [2, 3]. The acute ischemic injury causes immediate cell death in the infarct region with concomitant loss of function. This primary injury mechanism, though it may be relatively minor, initiates a sequence of deleterious secondary remodeling events during the following weeks that greatly reduces cardiac function. The primary injury will induce a pro-inflammatory environment with recruitment of multiple immune cell types, and will eventually undergo myofibroblast mediated remodeling into fibrous scar tissue [3]. The loss of contractility in this scar region increases the remaining physical load on remaining cardiomyocytes. Like skeletal muscle fibers, cardiomyocytes are terminally differentiated and post mitotic, requiring adjacent cardiomyocytes to compensate for this increased load via cellular hypertrophy [58]. Consequently, increased stress is applied to the scar region, promoting continued remodeling and ultimately dilation to reduce wall stress, which in turn increases end diastolic and end systolic volumes. The hemodynamic load on remaining

cardiomyocytes increases, creating a feedback loop between negative remodeling and compensatory mechanisms that ultimately leads to abnormal pressure, reduced ejection fraction, and potentially heart failure [3].

Due to the low frequency and/or ineffectual regenerative response, endogenous cardiac regeneration mechanisms in the adult heart are not well understood. Several studies have shown that there is cardiomyocyte renewal during homeostasis in adult heart tissue, though at a very low rate [58]. Much of our understanding of cardiomyogenesis has been derived from studies during fetal development. It is known that differentiating cardiomyocytes express transcription factors such as GATA4, Nkx2-5, TBX5, and MEF2C [59], and terminally differentiated cardiomyocytes also express sarcomeric myosin and cardiac tropomyosin, analogous to skeletal muscle [59, 60]. *In vitro* studies of cardiomyogenic differentiation models, such as embryonic stem cell (ESC) or induced pluripotent stem cell (IPS cell) differentiation, have shown that early expression of these cardiac transcription factors are required for differentiation [61]. Although cardiac stem cells have been identified, they may not be numerous enough or are altered by the injury microenvironment to successfully overcome the fibrotic pathway [58, 62, 63]. These cells have therefore only been extensively studied in *in vitro* contexts where they can be expanded, typically with the goal of implantation for cardiac cell therapy applications [62-65]. The most well characterized cardiac stem cell is the c-kit<sup>+</sup> stem cell population [64], which has shown cardiomyogenic potential *in vitro*, but has not been observed to participate directly to cardiac repair *in vivo*. So unlike skeletal muscle, enhancement of cardiac stem cell regenerative potential is necessary for any degree of regeneration.

## 1.2 EXTRACELLULAR MATRIX (ECM) AS A BIOLOGIC SCAFFOLD

### 1.2.1 The role of ECM in tissues and organs

The extracellular matrix of tissues and organs is composed of a complex milieu of proteins and polysaccharides that provides structural, mechanical, and biological support to its resident cells. Rather than simply acting as an inert support structure, or “glue” which holds cells and tissues together, the ECM is a critical determinant of cell phenotype and function *in vivo*, providing biochemical and biomechanical signals influencing processes such as cell survival, proliferation, migration, differentiation, morphology, secretory profile, metabolism, and other specialized activities. The ECM in turn is composed of the secreted products of its resident cells, creating a feedback loop referred to as “dynamic reciprocity” between the ECM and its resident cells. The ECM has been shown to be a critical factor in histogenesis during development, homeostasis, and wound healing as well as other biological processes [66, 67].

Dynamic reciprocity between the ECM microenvironment and resident cells can also be involved in disease progression in many organ systems. Liver cirrhosis is an example of the progressive remodeling of an ECM to a fibrotic state after repeated chemical or pathogenic injury, which then disrupts function and prevents liver regeneration [68]. There is also evidence that abnormal ECM composition and organization can contribute to the development of certain types of cancer. In some models of breast cancer, tumor formation only occurs when the ECM substrate is disrupted regardless of oncogene expression [67]. Studies of breast cancer development have shown that tumor ECM consists of an altered composition and disrupted organization compared to normal tissue. Such disrupted ECM promotes dysregulation of mammary epithelial cell proliferation and phenotype to one similar to a ductal cell carcinoma *in*

*vitro*, and likewise, tumor cells produce tumor ECM. Conversely, tumor cells cultured on normal ECM will assume a non-cancerous organization and proliferation rate. This demonstrates that ECM-cell signaling is bidirectional [67].

Skeletal and cardiac muscle ECM also play critical roles in tissue function and disease. Mutations in the gene encoding the skeletal muscle ECM protein laminin alpha-2 lead to severe muscular dystrophy, which is due to an inability of muscle fibers to efficiently mechanically couple with the ECM [69, 70]. As stated previously, skeletal muscle satellite cells anatomically reside in a defined niche in direct contact with basement membrane proteins of the muscle ECM, and are required to maintain satellite cell quiescence [41, 42]. Cardiac ECM fibrotic remodeling is a well characterized event following myocardial infarction [2, 3]. Concomitant with cardiomyocyte necrosis is the activation and proliferation of myofibroblasts that contribute to cardiac ECM fibrotic remodeling for weeks after the acute infarction event. The replacement of contractile cardiac tissue with fibrotic scar not only increases the load on remaining tissue, but also results in ventricle wall thinning and dilation, further decreasing cardiac output and efficiency. Therefore, disease state ECM may inhibit regenerative processes by promoting further tissue degeneration and loss of function.

### **1.2.2 ECM as a biologic scaffold**

The potent biologic signals present in the native ECM make scaffolds composed of these materials an attractive option for tissue engineering applications. Indeed, numerous studies have shown that ECM scaffolds alter the default wound healing response when implanted in a site of injury. ECM scaffolds, which are not chemically crosslinked and devoid of cellular remnants, are

rapidly degraded [71, 72] and replaced with well organized site appropriate host tissue, a process termed constructive remodeling, rather than default fibrotic scarring pathways [73, 74].

ECM scaffolds are prepared from decellularized tissues, and have demonstrated efficacy in the repair of numerous soft tissues, including urinary bladder [75-78], esophagus [79-83], liver [84-86], lung [87-89], and muscular tissues [90-123]. Native xenogeneic and allogeneic tissues are decellularized via a series of mechanical, chemical, and/or enzymatic processes to yield an acellular scaffold that ideally maintains ECM composition and structure.

There are several considerations in ECM scaffold production. Adequate decellularization has been shown to be a necessary aspect. Whereas ECM proteins are highly conserved among mammalian species, non-autologous cells present multiple surface and intracellular antigens that would be recognized by the host immune system. For example, the systemic tissue rejection response following organ transplantation is more accurately rejection of the implanted donor cells, and not the ECM [124, 125]. Implanted acellular ECM does induce an immune response, though it is primarily via activation of innate immune pathways, which is highly localized to the site of implantation [94, 124, 126]. Other considerations involve post processing following decellularization, such as chemical crosslinking and sterilization. Crosslinking is often performed to increase ECM mechanical properties and degradation time. However, such treatments inhibit natural proteolytic processes that are necessary for remodeling [72, 127, 128].

There are several factors and mechanisms that can influence the host response to a biologic scaffold, including the source tissue and the processing methods used to decellularize the tissue. The ECM of numerous tissues and organs have been evaluated for soft tissue repair, including dermis, small intestine, urinary bladder, and peritoneum, and each of these tissues are prepared using different decellularization techniques to achieve desired scaffold properties.

Processing methods that yield adequate decellularization, for example, are one of the key parameters to minimizing a pro-inflammatory response and associated poor remodeling outcomes that are elicited by necrotic cell fragments remaining in the scaffold [129, 130]. Therefore, both the tissue source and decellularization method require optimization for use in specific applications such as muscle repair.

### **1.2.3 Clinical applications of ECM scaffolds**

ECM scaffold materials have been successfully utilized in numerous clinical applications, typically for soft tissue repair as shown in Table 1. Ventral hernia repair is one of the most frequent clinical applications of ECM scaffolds. Most surgical mesh devices used for ventral hernia repair are composed of synthetic materials with robust mechanical strength, and are typically incorporated quickly into the host tissue.[131-136] While these mesh materials provide more than enough strength to prevent hernia recurrence, such devices are associated with non-trivial complications including adhesion, infection, fistula formation, and contraction [136-140]. Additionally, the innate immune response to the synthetic materials is classically a chronic pro-inflammatory foreign body reaction that promotes fibrotic encapsulation. This fibrotic encapsulation is associated with long-term patient discomfort, which can lead to revision surgery and surgical mesh removal [136, 141]. The intensity of the inflammatory response to an implanted mesh may be linked to the degree of tissue ingrowth and scar formation, and modulation of this response can have marked downstream effects [142]. Surgical mesh materials composed of naturally occurring allogeneic or xenogeneic extracellular matrix (ECM) have been used as an alternative to synthetic materials to abrogate the foreign body response, prevent infection, and minimize or avoid excessive fibrosis [107, 143-146]. In these circumstances,

facilitating a constructive host remodeling response is an advantage to the dense scar tissue deposition in the response to synthetic mesh materials [73, 146]. This logic has also justified the use of ECM scaffolds in applications such as breast reconstruction, where constructive remodeling is preferred to dense scar tissue.

**Table 1. Examples of clinical products composed of decellularized tissues.**

<b>Product</b>	<b>Tissue Source</b>	<b>Application</b>	<b>Manufacturer</b>
Alloderm®	Human demis	Soft tissue	Lifecell Corp.
AlloMax™	Human demis	Soft tissue	Bard Davol
Allopatch HD™	Human demis	Tendon, breast	Musculoskeletal Transplant Foundation
GraftJacket®	Human demis	Soft tissue	KCI
Strattice™	Porcine dermis	Soft tissue	Lifecell Corp.
Permacol™	Porcine dermis	Soft tissue	Tissue Science Laboratories
TissueMend®	Bovine dermis	Soft tissue	Stryker Corp.
Veritas®	Bovine dermis	Soft tissue	Synovis Surgical
Suspend™	Human fascia lata	Pelvic organ prolapse	Coloplast
Freestyle®	Porcine heart valve	Valve replacement	Medtronic Inc.
Prima Plus	Porcine heart valve	Valve replacement	Edwards Lifesciences Inc.
OrthAdapt®	Equine pericardium	Soft tissue	Synovis Orthopedic and Woundcare Inc.
Lyoplast®	Bovine pericardium	Dura mater	B. Braun Melsungen AG
Surgisis®	Porcine small intestine	Soft tissue	Cook Biotech Inc.
CuffPatch™	Porcine small intestine	Rotator cuff	Athrotek
Restore®	Porcine small intestine	Soft tissue	DePuy Orthopaedics
CorMatrix ECM®	Porcine small intestine	Pericardium, cardiac	CorMatrix® Cardiovascular Inc.
MatriStem®	Porcine urinary bladder	Soft tissue	Acell Inc.

## **1.3 TISSUE SPECIFIC ECM SCAFFOLDS IN TISSUE ENGINEERING**

### **1.3.1 The tissue specific ECM hypothesis**

There have been several recent studies to suggest that the source tissue of an ECM scaffold is a critical determinant of the host remodeling response [74, 84, 85, 88, 147-153]. The ECM of every tissue provides resident cells with a unique microenvironmental niche, which is the sum of numerous bioactive factors including cell adhesion proteins, glycosaminoglycans, and growth factors that are arranged in a tissue specific distribution and architecture. As previously stated, the ECM directly affects its resident cell's phenotype and function, providing numerous biologic signals. In turn, the ECM is also remodeled by these resident cells during homeostasis and injury. The net effect is a healthy matrix and cell population that are fundamentally linked to each other for the maintenance of tissue function.

The presence of healthy ECM signaling is therefore a critical component of a tissues function. It has been hypothesized that ECM scaffold remodeling may benefit from specific microenvironmental factors that are retained in the scaffold after tissue decellularization. It may be advantageous to utilize the tissue specific bioactive factors found in native tissues via the preparation and implementation of homologous ECM scaffolds (i.e. the use of a scaffold prepared from the same tissue that it is intended to treat).

### **1.3.2 Considerations in evaluating ECM tissue specificity**

Liver [84, 85], lung [88], vascular structures [154], bladder [75, 77], cardiac muscle [121, 123], and skeletal muscle [92, 93, 95, 98, 101, 102] have all been evaluated for homologous

implementation using a variety of methods. An important distinction to note is how tissue specificity is defined. *In vitro* assays, in which specialized tissue specific cell populations are cultured on or within a matched ECM scaffold, are often pertinent to evaluate functional characteristics such as transcriptional profile, surface marker expression, morphology, and/or protein secretory profile. Another approach is to expose undifferentiated stem cells to ECM to determine whether the ECM directs differentiation towards a tissue specific phenotype. *In vivo* functional comparisons may be more challenging, though restoration of function is the ultimate goal of an ECM therapy. In some of these cases, animal survival is dependent on immediate functional benefit. This would be true for cardiac replacement following heart failure, where circulatory support can only be maintained for a limited length of time via artificial means. Correspondingly, it would be impractical to implant an acellular scaffold to allow constructive remodeling, which may take months for functional cells to repopulate the scaffold. The whole organ engineering platform aims to reduce this functional gap by repopulating the decellularized organ with autologous host cells and preconditioning the organ in an *in vitro* bioreactor until the tissue reaches functional maturity. This strategy requires homologous ECM transplantation since the ECM structure is intrinsically linked to the physiologic function *in vivo*, and therefore comparisons to non-homologous ECM is not possible.

A potential confounding variable in these studies is the form of the ECM being evaluated. Specifically, the form refers to how altered the ECM meso- and macro- architecture is from the native state. There are several general classifications of ECM form that are present in the literature. These forms include: fully intact ECM (e.g. resulting from whole organ decellelularization), ECM sheets, comminuted ECM particulate, and enzymatically solubilized ECM (e.g. for ECM hydrogel formation). These final forms can be induced before or after

decellularization, i.e. an intact ECM scaffold may be reduced to a particulate for a desired application, or a particulate form of the native tissue can be decellularized. The precise approach depends on the optimal decellularization method for an application and the investigator's desired goals and applications for the study. A final caveat to this classification of form is that the decellularization method will induce some disruption of ECM structure at the micro and, potentially, the meso scales. The relevance of these changes must be evaluated on a case by case basis.

### **1.3.3 Studies that support a tissue specific hypothesis**

#### **1.3.3.1 Lung ECM**

Lung ECM has been among the most well studied sources for tissue specific ECM applications. Particulate forms of decellularized alveoli were first isolated by mechanical disruption with sonication and detergent treatment by Kuttan et al. [155], which was then characterized and shown to retain multiple basement membrane components and glycosaminoglycans found in the native ECM. Later work by Lwebuga-Mukasa et al. [156] decellularized intact alveoli using only detergent-based methods. Pneumocyte culture on alveolar ECM promoted a distinct transition of type II pneumocytes to type I pneumocytes when compared to the basement membrane of decellularized amnion, though the significance of this transition is questionable since culture on tissue culture plastic produces the same effect. More recent studies have also investigated fragmented lung ECM for tissue specificity. A study comparing decellularized lung and liver fragments found that these ECMs preferentially supported primary alveolar cells and hepatocytes, respectively [157]. Alveolar cells increased lung specific gene expression to a greater extent on lung ECM than liver ECM, while

hepatocytes effectively maintained morphology on liver ECM. An advantage of this study is that both tissues were decellularized with the same chemical treatments [157]. There have been numerous other studies that have focused on *in vitro* characterizations of biochemical composition [155-161] and/or mechanical properties [159, 160, 162] of a decellularized lung. These methods generally involve infusion of detergents through the vascular and/or conducting airways to remove cells and produce intact whole lung ECM. In addition to characterization, many of these studies investigated the effects of the lung ECM on cellular or physiologic function, *in vitro* or *in vivo*, respectively. Embryonic stem cell (ESC) derived lung progenitors seeded in intact lung form ciliated epithelium [163], and functional surfactant producing pneumocytes [159] *in vitro*. Furthermore, ESCs were affected by the local ECM environment and adopted lung cell phenotypes in appropriate anatomic locations (proximal vs. distal locations) [147]. Multipotential adult stem cells such as bone marrow derived mesenchymal stem cells (MSCs) were also maintained on lung ECM [160] and shown to respond to specific ECM components. MSCs preferentially migrated to regions of intact Type IV collagen and transiently expressed lung development markers, though they did not fully differentiate into pneumocytes.

Finally, several studies have investigated homologous implantation of lung ECM recellularized with autologous cells in *ex vivo* organ engineering [88, 164, 165]. The goal of this approach is to repopulate the lung ECM with relevant cell lung populations in their proper anatomic location within the ECM. The cells and ECM are then preconditioned *in vitro* with physiologic mechanical and biochemical signals using a bioreactor to promote appropriate cell and, eventually, tissue function prior to implantation (Ott, Price 2010, Nichols, 2013). Recellularized lung ECM has been shown to facilitate gas exchange *in vitro* and *in vivo* where homologous implantation improved partial pressures of arterial oxygen and carbon dioxide

similar to lung transplantation. Pulmonary improvement can be maintained for several hours to one week before edema, inflammation, and fibrosis occurs and function declines. (Ott 2010, Song 2013)

These reports generally support the use of tissue specific lung and liver ECM scaffolds. Such scaffolds maintain cell phenotype and function *in vitro*, and support homologous transplantation of recellularized ECM *in vivo*. These applications are greatly dependent on maintenance of the ECM structure as well as its composition for *in vivo* application and eventual *ex vivo* organ engineering.

### **1.3.3.2 Skeletal muscle ECM**

Skeletal muscle ECM has shown mixed results for *in vivo* constructive remodeling. The first descriptions of decellularized skeletal muscle were used for non-homologous implantation as a peripheral nerve graft [166]. The premise was to use the tubular basement membrane architecture as a conduit to guide regenerating nerve. The muscle supported some axonal growth through the graft, similar to allogeneic nerve grafting. Homologous muscle ECM implantation was first described in a series of studies using a deoxycholate detergent based protocol [92, 93, 95, 98]. The resultant ECM maintained muscle ECM architecture and retained multiple growth factors, though these were not evaluated for full decellularization. The muscle ECM alone, or in combination with VEGF, was not effectively remodeled in muscle injury. Histologic evidence of myogenesis was induced, however, when scaffolds were pre-seeded and cultured with myoblasts prior to implantation. A similar observation was later found by Merritt et al., in which a combination of mesenchymal stem cells and muscle ECM was required for a constructive remodeling response [101, 102]. Combined implementation of support structures may improve the response however. Decellularization of both abdominal wall muscle tissue and its associated

fascia connective tissue layer showed that each had distinct effects on the immune response, angiogenesis, and myogenesis suggesting that the fascia layer may synergize with implanted muscle ECM [167]. Not all of these studies, however, rigorously evaluated how decellularization and residual cellular material may affect the response.

Gillies et al. developed a novel approach to decellularization that did not use detergents, enzymes, or organic solvents, which have denaturing effects on ECM components [168-171]. DNA and intracellular protein removal was achieved using latrunculin B to induce actin polymerization and disrupt intracellular organization to allow solubilization and removal [168]. The host immune response to these non-detergent decellularized scaffolds has been extensively characterized and shown to promote anti-inflammatory macrophage and T-cell accumulation, though effects on myogenesis were not determined [172, 173]. Hydrogels composed of enzymatic degradation products of muscle ECM have also been evaluated [174, 175]. These pepsin digested muscle ECM scaffolds increased myoblast proliferation *in vitro* and markedly improved angiogenesis *in vivo* following ischemic injury, concomitant with recruitment of early myogenic cells.

A number of studies have focused on evaluating the functional improvement of VML defect repair with skeletal muscle ECM scaffolds *in vivo*. Acellular muscle ECM implantation with subsequent remodeling in a VML injury model yielded some myogenesis within the defect [102, 176, 177]. However, force production was increased by approximately 50% compared to untreated defect controls. The authors concluded that the muscle ECM acted as a non-fibrotic bridge between the muscle stumps to allow continuous force transduction as the mechanism of improvement rather than *de novo* myogenesis [176]. A similar study using acellular muscle ECM found evidence that this force transduction through the ECM has a protective function on

adjacent muscle tissue preventing its degeneration and fibrosis in the absence of significant myogenesis [178]. Cell seeding the ECM prior to implantation improves functional recovery in a VML model, as seen with the increase in myogenesis, though cell delivery alone was not compared [101]. The role of ECM tissue specificity in these studies is difficult to ascertain since a non-muscle ECM was not compared, and the proposed mechanism of functional improvement are not dependent on site appropriate muscle formation.

### **1.3.3.3 Cardiac ECM**

Cardiac muscle tissue has been decellularized from both whole intact hearts and heart fragments. Much like other whole organ decellularization methods, intact heart decellularization involves using the native vasculature to perfuse decellularization chemicals through the tissue. Typically, retrograde perfusion through the aorta is used due to the robustness of the aorta and left ventricle to withstand high pressures and flow [151, 179]. There have been several *in vitro* studies that have compared whole heart decellularization methods for cell removal efficacy, maintenance of structure, and retention of specific cardiac factors such as basement membrane proteins and glycosaminoglycans [180, 181] and biaxial mechanics [182]. Perfusion decell can also be effective through direct coronary perfusion in isolated regions of the myocardium [180, 183]. Cardiac ECM prepared by left ventricle immersion decellularization maintained structure & mechanics, and supported MSC growth and myogenic differentiation *in vitro*, however these studies lacked comparisons to other ECM source tissues [184, 185]. These methods have also been optimized for decellularizing human cardiac tissue, which produced similar results to the porcine tissue [186]. Alternative forms of ECM have also been tested in MI repair. Powdered cardiac ECM injected into an MI model increased ejection fraction and decreased dilation. [187] Thin sheets of decellularized left ventricle were shown to be affected by the cell type with which

they are seeded. Cardiac ECM seeded with fibroblasts contracted, though spontaneous beating was observed when the ECM was seeded with cardiomyocytes [188]. A composite cardiac left ventricle ECM/purified Type I collagen gel was able to direct ESC cardiomyogenesis in the absence of cardiac specific factors [189]. Human induced pluripotent stem cells (iPS cells) seeded within intact mouse heart ECM differentiated more efficiently into cardiomyocytes which were able to spontaneously contract and generate measurable force [190]. Similar contractile results were obtained for intact rat heart ECM seeded with endothelial cells and cardiomyocytes [151]. Extensive investigation of cardiac ECM degradation products has shown significant effects on stem cell cardiomyogenic differentiation *in vitro* and functional improvements *in vivo* following MI. These hydrogel forming ECM degradation products not only impart bioactivity to reduce negative fibrotic remodeling outcomes, but can be delivered via minimally invasive means. ECM gel can be injected directly into multiple locations within infarcted tissue through femoral artery cannulation [120, 121, 191, 192].

#### **1.3.4 Studies that do not support a tissue specific hypothesis**

Most of the clinically utilized ECM scaffolds are used in non-homologous locations with varying degrees of success. Urinary bladder and/or small intestine derived ECM scaffolds have been utilized in lung [193], myocardial [110-119, 122] and skeletal muscle [91, 96, 97, 103-107] repair. Taken together, these studies provide useful comparisons of the host response to the same non-tissue specific ECM scaffolds (e.g. urinary bladder ECM) implanted in several different anatomic locations, and may elucidate general remodeling trends.

There are few reports of the use of non-tissue specific lung ECM for lung applications. One example is application of urinary bladder ECM (UBM) for prevention of pulmonary

fibrosis. Particulate and enzymatically digested forms of UBM were intratracheally infused into the lung and shown to mitigate bleomycin induced pulmonary fibrosis [193]. Lung ECM was not evaluated in this model, but these results show that non-lung ECM can also provide beneficial effects to injured lung tissue *in vivo*.

One of the most well characterized ECM materials is small intestinal submucosa (SIS) [194], which has been used in multiple clinical skeletal muscle applications such as rotator cuff repair and ventral hernia repair, as well as multiple pre-clinical studies to treat a multitude of tissues. SIS implantation in muscle locations have shown greatly increased myogenesis and functional improvements in musculotendinous junction and abdominal wall injury locations [105, 107], though this same material in a composite VML/periosteal injury was predisposed to promote bone and connective tissue formation rather than muscle [195]. This suggests that the effect of SIS may depend on implantation location and type of injury induced. Urinary bladder derived ECM has a similar constructive remodeling response to SIS in muscle injury locations [99, 196, 197]. These scaffolds are degraded and remodeled with islands of skeletal muscle forming within the injury location. Studies have also shown that an anti-inflammatory macrophage phenotype is associated with improved remodeling and myogenesis in these models [196]. Stem cell seeded bladder ECM scaffolds markedly improved myogenesis and functional recovery in VML models, and was dependent on seeding density and preconditioning methodology prior to implantation. Acellular bladder ECM in this model improved function to a lesser extent, and with less myogenesis [198-200].

Non-cardiac specific urinary bladder and SIS ECM has also been investigated for cardiac repair applications *in vivo*, and have been shown to encourage remodeling and improve cardiac function [110-113, 115]. Cell seeding [122] or infusion with bioactive factors (e.g. exogenous

growth factors) prior to implantation further improves this functional recovery [116]. Like cardiac ECM, ECM degradation products prepared from small intestine ECM also encourages functional remodeling and protection from dilation and fibrosis [114, 201]. Most *in vivo* evaluations of cardiac ECM efficacy have been compared to synthetic materials such as Dacron, which are the clinical standard of care, rather than to other ECM devices [123, 179]. Both cardiac and non-tissue specific ECM have been more effective as cardiac patch materials compared to synthetics, though these studies do not establish tissue specific effects. Remlinger et al., however, did compare cardiac patches cut from whole heart ECM [202, 203] to patches composed of urinary bladder ECM for right ventricle outflow tract repair. Though both types of ECM promoted endothelialization and  $\alpha$ -actinin positive cardiomyocyte formation, bladder ECM was more quickly and more effectively remodeled with new cardiomyocytes over the time course of this study than cardiac ECM [203]. However, the cardiac and urinary bladder ECM used in this study was very different in thickness and geometry prior to implantation, which may have affected remodeling.

There is also a growing body of evidence supporting the use of these non-tissue specific ECM scaffolds for clinical repair of VML and cardiac defects. Urinary bladder ECM has been implanted in the repair of VML defects in quadriceps, tibialis anterior, and biceps muscles, which have resulted in greatly increased function [204]. This functional improvement was measured not only by force production, but also task completion, such as the ability to perform a range of different motions and activities necessary for normal ambulation [204]. Multiple case studies have reported the use of SIS ECM scaffolds for repairing congenital atrial septal defects (and other cardiac repair applications) in humans [117, 119, 205, 206]. There has been a low

incidence of adverse events, and follow up studies suggest good incorporation and remodeling. Tissue specific ECM scaffolds have not yet been clinically translated for these tissues, however.

In both skeletal and cardiac muscle repair applications, non-homologous scaffolds are degraded and remodeled with reported increases in contractile function. Different studies have either shown advantages, disadvantages, or no difference in comparing tissue specific and non-specific ECM. Each of these conclusions would lead to discordant interpretations. A tissue specific advantage would support the logic that the ECM of every tissue has been optimized during evolution to be the ideal scaffold for that tissue. However, the success of non-homologous ECM sources would imply that the compositional differences between different ECMs does not significantly affect tissue remodeling outcome in these applications, or that certain ECM sources universally provide necessary support to a wide array of tissues.

### **1.3.5 Limitations in determining ECM tissue specificity**

Few studies provide well controlled comparisons between ECM scaffolds prepared from different tissues either *in vitro*, or more importantly, *in vivo*. Many of the aforementioned studies investigated a tissue specific ECM scaffold in isolation (or compared to synthetic materials), and thus characterized *in vitro* and *in vivo* responses without comparison to non-specific ECM. Though determinations of clinical feasibility and efficacy may be ascertained, this approach does not answer the question as to whether homologous utilization of a tissue specific scaffold confers an advantage in tissue remodeling to justify their use. Potential practical advantages of non-homologous ECM scaffolds over homologous sources include a greater relative abundance or ease of preparation. Furthermore, those studies that did provide ECM comparisons are potentially confounded by differences in the decellularization method. These differences are to

be expected since each tissue possesses differing requirements to achieve adequate decellularization while still retaining ECM specific factors. However, these differences also affect the ability to make valid comparisons and so rigorous maintenance of similar processing methods are required.

Additional research is required to determine if there is an advantage to utilizing a homologous scaffold in muscle injury, or whether only certain tissues are influenced by tissue specific effects. The goal of the proposed study is to determine the tissue specific effects of muscle derived ECM scaffold materials. To address the question of tissue specificity, ECM must be prepared using similar and controlled methods for all tissues. This study will compare ECMs prepared from cardiac muscle, skeletal muscle, and small intestine using a single decellularization protocol. In addition, small intestinal submucosa ECM will be prepared by a standard method of tissue decellularization to allow comparisons to previous studies that have used small intestinal ECM.

## **1.4 HYPOTHESIS AND SPECIFIC AIMS**

### **1.4.1 Motivation and central hypothesis**

Tissue specific ECM scaffold utilization has been evaluated for multiple tissues and organs. Though certain tissues, such as lung and liver, appear to confer a clear advantage for homologous ECM implantation, skeletal and cardiac muscle tissues are less clear (see previous section). The overall objective of the present work is to determine if a scaffold composed of

striated muscle ECM (cardiac or skeletal muscle) is superior for the treatment of muscle injury than scaffolds from non-muscle sources. The central **hypothesis** for this study is as follows: the skeletal muscle specific microenvironment in skeletal muscle ECM scaffolds facilitates a greater degree of functional restoration after muscle injury than non-muscle ECM scaffolds. The corollary to this hypothesis is that cardiac muscle ECM would also promote functional skeletal muscle remodeling relative to non-muscle ECM, but not to the extent of skeletal muscle ECM due to tissue specific differences between skeletal and cardiac muscle ECM. The following specific aims are designed to test this hypothesis in a systematic and controlled manner.

#### **1.4.2 Specific aim 1**

Isolate ECM from skeletal muscle tissue and characterize the structure and biochemical composition, and then to compare the structure and composition of skeletal muscle ECM scaffolds to ECM scaffolds derived from cardiac muscle and a non-muscle tissue source: small intestinal submucosa prepared using either conventional methods or muscle ECM processing methods.

#### **1.4.3 Specific aim 2**

Determine the effect of ECM scaffold tissue source on muscle progenitor cell proliferation and differentiation in vitro using muscle and non-muscle ECM scaffold degradation products.

#### **1.4.4 Specific aim 3**

Determine the in vivo remodeling characteristics of muscle and non-muscle ECM scaffolds in a model of murine volumetric skeletal muscle loss.

## **2.0 DEVELOPMENT AND CHARACTERIZATION OF A BIOLOGIC SCAFFOLD COMPOSED OF SKELETAL AND CARDIAC MUSCLE EXTRACELLULAR MATRIX<sup>1</sup>**

### **2.1 INTRODUCTION**

Biologic scaffold materials composed of extracellular matrix (ECM) are typically produced by decellularization of mammalian tissues such as urinary bladder, dermis, or small intestine [74] and have been shown to facilitate the functional reconstruction of several tissue types [207, 208] including the lower urinary tract [77, 209], heart and vascular structures [111, 117], esophagus [79, 96], and musculoskeletal tissues [97, 103, 105, 107], among others. The mechanisms by which constructive remodeling occurs include the recruitment of multipotential stem and progenitor cells to the site of scaffold placement [210, 211], promotion of a favorable M2 macrophage phenotype at the host tissue/bioscaffold interface [197], regional angiogenesis [106], and mitogenesis [211, 212]. These tissue derived biologic scaffolds are frequently used in non-homologous anatomic sites, but recent studies have suggested that biologic scaffolds derived from site specific homologous tissues such as liver and lung may be better suited for constructive tissue remodeling than non-site specific tissue sources [85, 88, 147, 149, 150, 152, 213].

---

<sup>1</sup>This work has been adapted from the following published manuscript:

Wolf MT, Daly KA, Reing JE, Badylak SF. Biologic scaffold composed of skeletal muscle extracellular matrix. *Biomaterials*. 2012;33(10): 2916-25. <http://dx.doi.org/10.1016/j.biomaterials.2011.12.055>

Muscle tissues, including cardiac, skeletal, and smooth muscle, respond favorably when biologic scaffolds are used for their reconstruction following injury [105, 107]. To date, there have been several attempts to isolate and process skeletal muscle ECM (M-ECM) [92, 93, 95, 98, 102, 168, 175, 214]. Most of these attempts have involved the decellularization of intact rodent muscles or the extraction of rodent muscle ECM proteins, with varying degrees of success. DeQuach et al. [175] did show that proteins extracted from a decellularized porcine muscle matrix retain bioactivity. None of these studies have provided a detailed characterization of the intact M-ECM scaffold derived from a large animal tissue source, nor have any of these studies applied stringent decellularization criteria in the development of the decellularization process. The objectives of the present study were to 1) determine a method for decellularization of skeletal muscle and characterize the structure and composition of the resulting ECM, and 2) to compare the in-vitro bioactivity and in-vivo remodeling properties of skeletal muscle ECM vs. non-muscle ECM, specifically SIS, in a rodent model of abdominal wall muscle repair. Following this initial assessment of in vitro and in vivo compatibility, M-ECM was prepared from porcine skeletal muscle to compare its composition to porcine cardiac ECM (C-ECM), small intestinal submucosa prepared using the M-ECM protocol (SIS-M) and porcine SIS using the standard protocol. These comparison groups are provided in Table 2.

**Table 2. Summary of each ECM group's tissue source and the decellularization method.**

<b>ECM group</b>	<b>Tissue source</b>	<b>Decellularization method</b>
M-ECM	Skeletal muscle	Muscle protocol
C-ECM	Cardiac left ventricle	Muscle protocol
SIS-M	Small intestinal submucosa	Muscle protocol
SIS	Small intestinal submucosa	Conventional protocol

## **2.2 METHODS**

### **2.2.1 Overview of experimental design**

The present aim was encompassed two primary objectives. The first was to develop a consistent methodology of decellularizing skeletal muscle. This was achieved by decellularizing canine skeletal muscle by enzymatic and chemical methods. The resulting M-ECM was then assessed for structure and cytocompatibility: the effect on cell attachment and metabolism *in vitro*, and the *in vivo* remodeling characteristics in a rat abdominal wall defect model. ECM composed of porcine small intestinal submucosa (SIS) was used for comparison purposes. The second objective was to apply this decellularization procedure to porcine skeletal muscle, cardiac muscle, and small intestine, and then to characterize the composition of the resultant scaffolds. All animal experiments were conducted in accordance to University of Pittsburgh Institutional Animal Care and Use Committee (IACUC) regulations and guidelines.

### 2.2.2 Skeletal muscle decellularization protocol

Whole quadriceps and hamstring muscle groups were isolated from mongrel dogs and frozen at -80°C immediately following sacrifice. While frozen, entire muscle groups were then sliced into 2.25 mm thick sheets transverse to the alignment of muscle fibers. The muscle slices were then thawed and trimmed of all macroscopic vasculature, fat, and connective tissues, rinsed in deionized water for 1 hour and lyophilized. Muscle tissue slices were then decellularized in batches weighing approximately 18-20 g (dry wt.)

The lyophilized muscle was decellularized following the protocol summarized in Table 3. Briefly, the muscle was subjected to lipid extraction by placement in a 2:1 (v/v) solution of chloroform/methanol (Fisher, Waltham, MA) for 2 hours under a constant stir rate [215]. The muscle was rehydrated using a graded series of ethanol and then exposed to a series of enzymatic and chemical treatments to remove cellular materials in a spinner flask at a stir rate of 70RPM. These treatments consisted of: 0.2% Trypsin/0.2% EDTA for 2 hours (at 37 °C and pH = 7.6), 2% sodium deoxycholate for 5 hours, 2% sodium deoxycholate for 14-16 hours, 1% Triton-X 100 for 1 hour, and finally 0.1% (w/v) peracetic acid/4% (v/v) ethanol for 2 hours followed by extensive rinsing. The muscle tissue was washed with deionized water and 2X phosphate buffered saline (PBS) between each step. The M-ECM scaffolds were lyophilized for storage. Scaffolds used for tissue culture or *in vivo* implantation were terminally sterilized with ethylene oxide (16 hour cycle at 50°C in a Series 3plus EOGas Sterilizer, Anderson Sterilizers, Inc. Haw River, NC).

**Table 3. Summary of the steps in the decellularization of skeletal muscle tissue including the chemical treatment and time of exposure.**

<b>Chemical</b>	<b>Length of Treatment</b>
Chloroform/methanol (2:1 v/v)	2 hours
Graded series of alcohol (100,90,70,50,0)	30 min ea.
0.2% Trypsin/0.2% EDTA at 37 °C	2 hours
Deionized water, 2X PBS	30 min ea.
2% sodium deoxycholate	5 hours
Deionized water, 2X PBS	30 min ea.
2% sodium deoxycholate	14-16 hours
1% Triton X-100	1 hour
Deionized water	30 min
0.1% (w/v) peracetic acid/4% ethanol (v/v)	2 hours
1X PBS	30 min ea. (twice)
Deionized water	30 min ea. (twice)

### **2.2.3 Conventional small intestine decellularization and muscle decellularization method**

Porcine small intestine (jejunum) was obtained from 6 month old pigs from the local abattoir and prepared as previously described [216]. In brief, the majority of the mucosa and the entire serosa, and muscularis externa layers of the intestine were mechanically delaminated from the intestine. Approximately 80 g (wet wt.) of the remaining submucosa, muscularis mucosa and

stratum compactum layers were washed with water and treated with 1.6 L of 0.1% (w/v) peracetic acid/4% (v/v) ethanol for 1 hour. SIS was then rinsed extensively, lyophilized, and sterilized with ethylene oxide.

SIS-M was prepared by exposing 5 cm x 5 cm sheets of the isolated submucosa, muscularis mucosa and stratum compactum layers to the muscle decellularization protocol. Intestine sheets were lyophilized and exposed to the same treatments as Table 2.

#### **2.2.4 Verification of muscle decellularization**

Decellularization was defined as fulfilling the following criteria for DNA content: having less than 50 ng dsDNA/mg ECM dry weight, having all residual DNA fragments be less than 200 base pair in size, and lacking visible nuclei after histologic staining with 4',6-diamidino-2-phenylindole (DAPI). [74] Immediately after processing, M-ECM samples (n = 7) were fixed in 10% neutral buffered formalin. Samples were then embedded in paraffin, surface sectioned, and then stained with H&E and DAPI for detection of nuclei multispectrally at 200X magnification. (Nuance multispectral imaging, CRi, Cambridge, MA) Additional non-fixed samples were used to quantify the amount of double stranded DNA using the PicoGreen assay (Invitrogen, Carlsbad, CA). DNA was extracted from powdered M-ECM by digesting in 0.1 mg/ml proteinase K (Sigma, St. Louis, MO) at 50°C for 24 hours. Samples were then purified with two phenol/chloroform/isoamyl alcohol (25:24:1 v/v) extractions. After ethanol precipitation and drying, the DNA was resuspended in 1ml TE buffer (pH = 8.0) then quantified using the PicoGreen assay according to the manufacturer's instructions. The size of the extracted DNA fragments was determined after separation by 2% agarose gel electrophoresis.

### **2.2.5 Scanning electron microscopy**

Scanning electron micrographs were taken to examine the surface topology of M-ECM and native muscle tissue. Prior to final lyophilization, samples were fixed in cold 2.5% (v/v) glutaraldehyde (Electron Microscopy Sciences, Hatfield, PA) in PBS for at least 24 hours, followed by three washes in PBS. Lipid fixation was performed in 1% (w/v) osmium tetroxide (Electron Microscopy Sciences) for 1 hour followed by three washes in PBS. Fixed samples were then dehydrated using a graded series of alcohol (30, 50, 70, 90, 100%) for 15 minutes each, followed by 15 minutes in hexamethylenediamine (Fisher) and subsequent air drying. The dried samples were sputter coated with a 3.5nm layer of gold/palladium alloy using a Sputter Coater 108 Auto (Cressington Scientific Instruments, Watford, UK) and imaged with a JEOL JSM6330f scanning electron microscope (JEOL, Peabody, MA) at 25X, 500X, 1000X, and 10,000X magnifications.

### **2.2.6 Cell culture and metabolism on M-ECM scaffolds**

C2C12 mouse myoblast, human perivascular stem cell, NIH 3T3 mouse fibroblast, and human microvascular endothelial cell (HMEC) lines were cultured on the surface of M-ECM scaffolds and the abluminal side of SIS to evaluate in vitro cell compatibility. The perivascular stem cells were isolated from fetal skeletal muscle (as described by Crisan et al. [217]), and passage 8-12 was utilized for all experiments. The HMEC, C2C12, and NIH 3T3 cell lines were obtained from ATCC (Manassas, VA). C2C12 and NIH 3T3 cells were cultured in Dulbecco's Modified Eagle Medium (DMEM) (Invitrogen) supplemented with 10% fetal bovine serum (FBS), (Hyclone) and 100U/ml penicillin/100µg/ml streptomycin (Invitrogen). HMECs were cultured in

MDCB131 Medium (Invitrogen), supplemented with 10% FBS and 100U/ml penicillin/100µg/ml streptomycin. Perivascular stem cells were cultured in DMEM supplemented with 20% FBS and 100U/ml penicillin/100µg/ml streptomycin. C2C12 cells were also cultured in low serum conditions to induce myotube formation, which consisted of DMEM supplemented with 2% horse serum and 100U/ml penicillin/100µg/ml streptomycin.

C2C12 cells, perivascular stem cells, NIH 3T3 cells, and HMEC cells were seeded on the surface of lyophilized sheets of M-ECM at a density of 500,000 cells/cm<sup>2</sup> for 7 days, with media changes after the 1st and 4th days. C2C12 cells were grown in both high serum and low serum differentiation conditions. The cell seeded scaffolds were then fixed in formalin, cut into 5 µm cross sections, and stained with H&E. These were imaged at 200X magnification and evaluated for cell morphology characteristics. Perivascular stem cell seeded scaffolds were also fixed with formalin and labeled with Alexa Fluor-546 conjugated phalloidin (Invitrogen) for actin and DAPI for nuclei. The scaffold surface was then imaged with a confocal microscope. (Leica DMI 4000B, Leica Microsystems, Buffalo Grove, IL)

Lyophilized M-ECM and SIS sheets (n = 6-12) from 2 different scaffold preparations were cut into 8mm disks using a biopsy hole punch, placed into a 96-well plate, and anchored to the bottom of the wells with silicone rings. The disks were sterilized with ethylene oxide (16 hour cycle at 50°C in a Series 3plus EOGas Sterilizer) and seeded in triplicate with C2C12 myoblasts or perivascular stem cells at a density of 4,000 cells/well in 200 µl of media. Cells were also seeded in wells with only the plastic anchor ring as controls (n = 3-6). Cells were cultured for 1, 3, and 5 days in standard media, and at each timepoint, cell metabolism was assessed using the alamar blue assay (Invitrogen). Alamar Blue reagent was added to each well for 6 hours, then transferred to a separate plate and read fluorescently (ex:560, em:590). A non-

seeded scaffold background control was subtracted from each reading. All values were normalized to a standard curve of 1,000-20,000 cells/well adding Alamar Blue 4 hours after seeding and measuring after 6 hours of incubation in the Alamar Blue reagent.

### **2.2.7 Acute evaluation of an M-ECM scaffold in a rat abdominal wall defect model**

The in vivo remodeling characteristics of M-ECM and SIS scaffolds were determined in a partial thickness abdominal wall defect model in the rat. [127] A 1x1 cm partial thickness defect was created in the ventrolateral abdominal wall of female Sprague-Dawley rats by removing the external and internal oblique muscles (both are skeletal muscle) while leaving the transversalis muscle and the peritoneum intact. The defect was repaired with a 1x1 cm sheet of M-ECM or SIS sutured at the 4 corners of the defect with 4-0 Prolene sutures (Ethicon Inc., Somerville, NJ), or left untreated with no implanted ECM as a defect only control. The skin incision was then closed with absorbable 4-0 Vicryl sutures (Ethicon) and the rats were allowed to recover normally. Rats were sacrificed 14 and 35 days post-implantation (n = 4 per group per time point), and the repaired defects were excised and fixed with formalin. Explants were then embedded in paraffin, sectioned, and stained with Masson's Trichrome stain or immunolabeled for fast and slow myosin heavy chain (MHC) to evaluate myogenesis as previously described [105, 218]. Slides were deparaffinized followed by epitope retrieval in 0.1 mM EDTA at 95-100 °C for 25 minutes and then 0.1% Trypsin/0.1% Calcium Chloride (w/v) at 37 °C for 10 minutes. Endogenous peroxidase activity was quenched by incubation in a 0.3% (v/v) hydrogen peroxide solution in TBS for 10 minutes at room temperature. Sections were then blocked with 2% normal horse serum/1% BSA in TBS (Vector) for 30 minutes at room temperature and then labeled with mouse anti-slow myosin heavy chain (1:1000, M8421, Sigma) for 40 minutes at room

temperature. Sections were then rinsed in TBS and incubated in a biotinylated goat anti-mouse IgG secondary antibody (1:200, Vector) diluted in blocking solution for 1 hour at room temperature. Sections were washed as before and incubated in the Vectastain ABC reagent (Vector) for 30 minutes at room temperature and then exposed to a diaminobenzadine substrate (ImmPact DAB, Vector) until appropriate staining developed. Sections were then incubated in blocking solution for 10 minutes followed by incubation in alkaline phosphatase conjugated mouse anti-fast myosin heavy chain (1:200, A4335, Sigma) diluted in blocking solution for 1 hour. After rinsing, color was developed by staining with red alkaline phosphatase (Vector) until appropriate staining developed. Slides were then counterstained with hematoxylin, dehydrated, and cover slipped.

## **2.2.8 Protein extraction and growth factor quantification**

Soluble proteins were extracted from different preparations of M-ECM , C-ECM, SIS-M, and SIS (n = 3 each), and native muscle tissues (n = 2) and analyzed for growth factor content.

Soluble proteins were extracted from 300 mg of powdered ECM or tissue in 7ml of a urea-heparin buffer (2M urea, 50mM Tris, 5 mg/ml heparin, 10mM N-ethylmaleimide, 5mM benzamidine, and 1mM phenylmethylsulfonyl fluoride at pH = 7.4). Samples in urea-heparin buffer were gently agitated for 20-24 hours at 4°C, after which they were centrifuged for 30 minutes at 3,000g and the supernatant collected. The remaining pellet was resuspended in freshly prepared urea-heparin buffer and the extraction process repeated. Each extract was then dialyzed against 80-100x volume of deionized water using 3500MWCO Slide-A-Lyzer dialysis cassettes (Pierce, Rockford, IL) for 24 hours, with water changes after 4 and 8 hours. The recovered

extracts were analyzed for total protein recovered using the BCA protein assay (Pierce) and frozen at -80°C until further use.

The isolated protein extracts were quantified for vascular endothelial growth factor (VEGF) and basic fibroblast growth factor (bFGF) with human ELISAs (R&D systems, Minneapolis, MN) following the manufacturer's instructions. Canine, porcine, and human bFGF and VEGF show a high level of sequence homology and extractions from native porcine tissue were found to be reactive with the human ELISA kits used.

### **2.2.9 ECM staining and immunolabeling**

M-ECM, C-ECM, SIS-M, SIS, and native muscle tissue were fixed in formalin, embedded in paraffin, and then cut into 5 µm sections. Standard histologic stains were performed using Herovici's Polychrome (staining for collagen Types I & III) and Movat's Pentachrome (staining for elastin, collagen, and GAGs). Immunolabeling studies were also conducted for the presence of basement membrane proteins laminin, type IV collagen, and fibronectin.

For immunolabeling, slides were deparaffinized followed by epitope retrieval in 10mM citrate buffer (pH = 6.0) at 95°C for 15 minutes. Endogenous peroxidase activity was quenched by incubation in a 3% (v/v) hydrogen peroxide/methanol solution for 30 minutes at room temperature. Non-specific antibody binding was blocked with 2% normal goat serum in PBS (Vector, Burlingame, CA) for 1 hour at room temperature. Tissues were then labeled with primary antibodies overnight at 4 °C. Antibodies were raised in rabbit against human laminin (1:50, L9393, Sigma), type IV collagen (1:100, T59106R, Meridian Life Science Inc., Saco, ME), and fibronectin (1:300, F3648, Sigma) and were diluted in the blocking solution. Sections were then rinsed in PBS and incubated in a biotinylated goat anti-rabbit IgG secondary antibody

(1:100, Vector) diluted in blocking solution for 2 hours at room temperature. Sections were rinsed as before and incubated in the Vectastain ABC reagent (Vector) for 30 minutes at room temperature and then exposed to a diaminobenzadine substrate (ImmPact DAB, Vector) until appropriate staining developed. Staining was stopped by rinsing sections in deionized water followed by counterstaining with hematoxylin. Antibody isotype controls were used in the place of the primary antibody to determine the presence of non-specific staining.

#### **2.2.10 Sulfated glycosaminoglycan quantification**

Sulfated glycosaminoglycan (GAG) content in different preparations of M-ECM, C-ECM, SIS-M, and SIS (n = 3) was determined using the Blyscan Sulfated Glycosaminoglycan Assay Kit (Biocolor Life Sciences, Carrickfergus, UK). For each sample, 10 mg/ml of powdered ECM was enzymatically digested with pepsin for 48 hours at room temperature. The digested scaffold was then assayed following the manufacturer's instructions.

#### **2.2.11 Statistical analysis**

All statistical analysis was performed using MATLAB software (MathWorks, Natick, MA). Metabolic activity differences were determined for both C2C12 myoblast and perivascular stem cell seeded scaffolds. Each substrate at every time point was analyzed using a two-way analysis of variance (ANOVA) with a Tukey post-hoc test and with a significance level of  $p < 0.05$ . All values are given as the mean  $\pm$  standard deviation.

## 2.3 RESULTS

### 2.3.1 Verification of decellularization

The amount and size of residual DNA content after decellularization for each preparation of M-ECM prepared was quantified and is presented in Figure 2. Histologic analysis of M-ECM (Figure 2A & C) showed no evidence of intact nuclear material on H&E or DAPI as compared to native muscle (Figure 2B & D). After decellularization, there was  $7.42 \pm 1.67$  ng DNA/mg dry weight compared to the  $1549 \pm 489$  ng DNA/mg dry weight found in native muscle tissue (Figure 2E). There were no clearly visible bands of DNA after separation on a 2% agarose gel, while native muscle showed a range of DNA fragments (Figure 2F). These values met previously described criteria of decellularization [74].

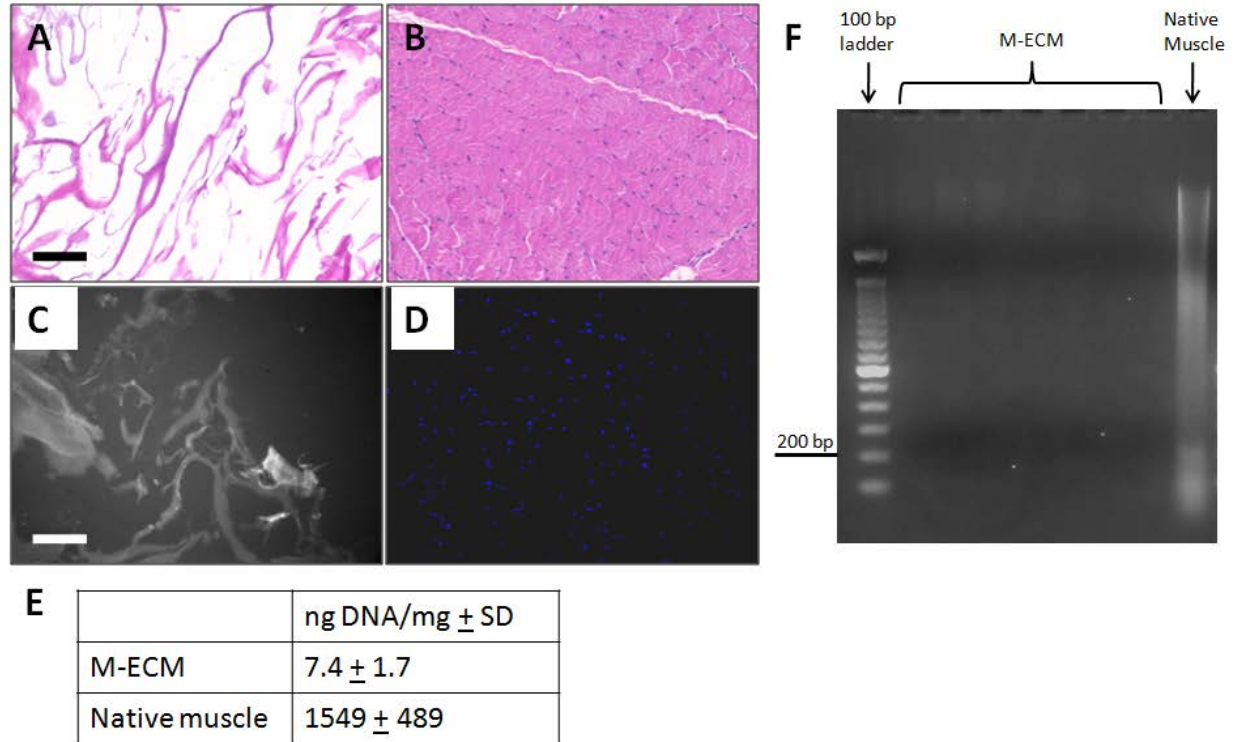


**Figure 2.** Residual DNA content of M-ECM scaffolds after decellularization for each batch tested in the study (n=7) compared to native muscle (n=2). Histologic appearance after H&E staining of (A) M-ECM and (B) native muscle tissue, and after DAPI staining of (C) M-ECM and (D) native muscle, bar represents 100  $\mu$ m. The DAPI stained M-ECM is overexposed and imaged multispectrally displaying scaffold autofluorescence as grey and nuclei as blue. (E) Results of the PicoGreen analysis for double stranded DNA extracted per mg dry weight of scaffolds  $\pm$  SD. (F) Extracted DNA from several batches of M-ECM separated via 2% agarose gel electrophoresis and compared with native muscle and a 100 bp ladder.

### 2.3.2 Scanning electron microscopy

The surface topology of M-ECM scaffolds was compared to native muscle tissue using SEM and is presented in Figure 3. M-ECM had an uneven surface composed of compact structures in a net

like pattern (Figure 3A-D). Higher magnification revealed that these structures consisted of long compact fibrils or bundles of fibrils with a banding pattern suggestive of collagen (Figure 3D, arrows). No myofiber cellular remnants were seen. In contrast, native muscle showed clear tubular myofiber boundaries with densely packed microfibrillar elements within each cell (Figure 3E-F).

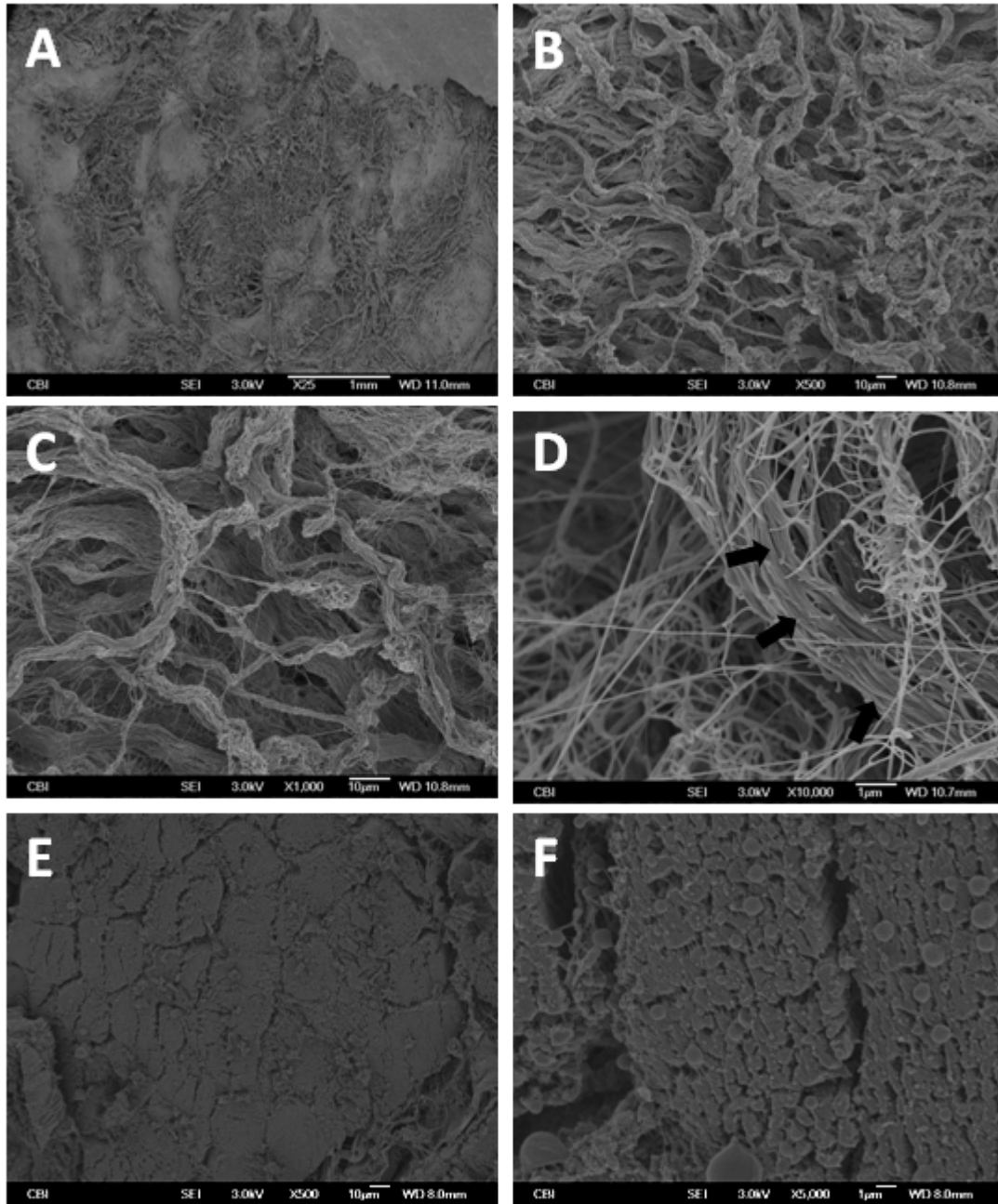


**Figure 3.** SEM images of M-ECM and native muscle tissue. M-ECM was imaged at (A) 25X, (B) 500X, (C) 1,000X, and (D) 10,000X magnifications and compared to native muscle cross sections at (E) 500X and (F) 5,000X. Long fibrils with a collagen-like banding pattern were observed in the M-ECM scaffold.

### **2.3.3 Cell culture and metabolism on M-ECM scaffolds**

Cell attachment, survival, and morphology was assessed using histologic methods for M-ECM and SIS scaffolds seeded with the following cell lines for 7 days in culture: C2C12 myoblasts (Figure 4A & B), human perivascular stem cells (Figure 4C-E), NIH 3T3 fibroblasts, HMEC endothelial cells, and differentiated C2C12 myotubes (Figure 5). Histologic cross sections showed a confluent layer of cells on the surface that possessed a normal, healthy morphology for all cell types on both M-ECM and SIS. Normal cell morphology was further confirmed for perivascular stem cells by staining and imaging the surface with phalloidin for actin (Figure 4E) showing spread cell morphology forming a confluent monolayer. C2C12 differentiation was supported on both M-ECM (Figure 5E & F) with the presence of elongated multinucleate myotubes upon histologic examination.

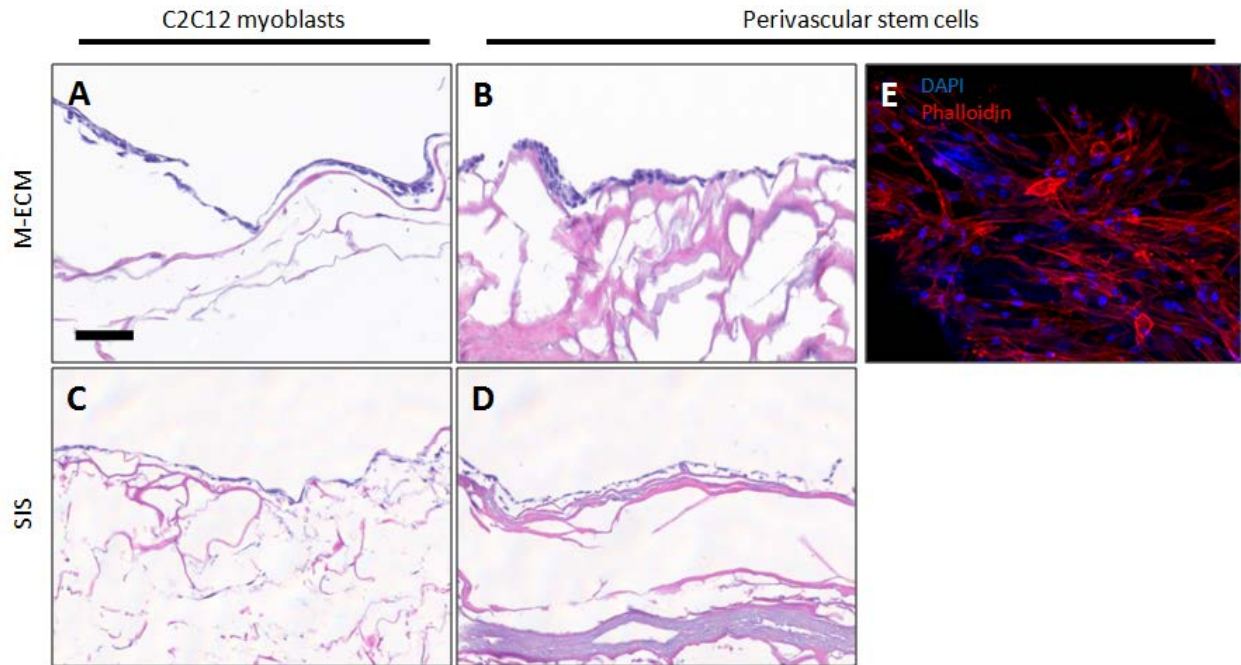


**Figure 4.** *In vitro* cell compatibility histology of (A,C) C2C12 myoblasts and (B,D,E) perivascular stem cells cultured for 7 days on the surface of M-ECM (A,B,E) or SIS (C,D). Representative images of (A-D) H&E cross sections and (E) fluorescent imaging labeling with phalloidin for actin (red) or DAPI for nuclei (blue). Scale bar represents 100  $\mu$ m.

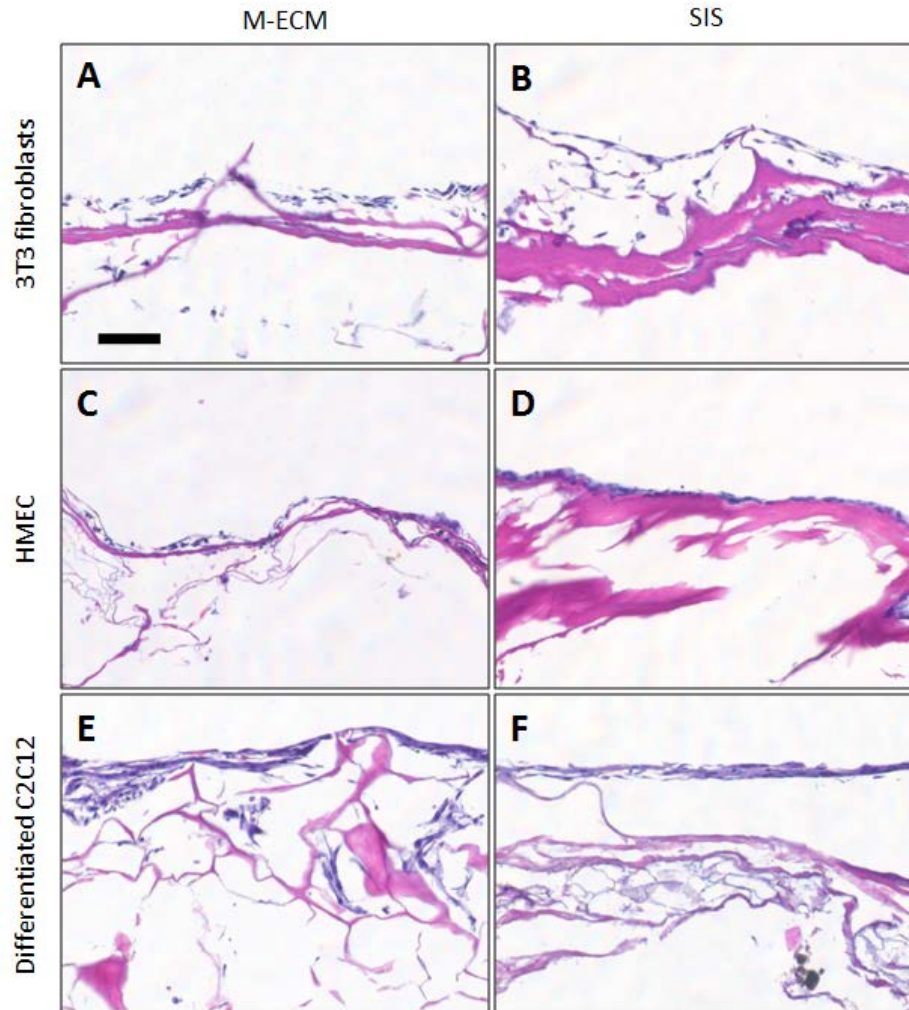


**Figure 5.** *In vitro* cell compatibility histology of (A-B) NIH 3T3 fibroblasts, (C-D) human microvascular endothelial cells, and differentiated C2C12 myoblasts (E-F) after 7 days of culture on (A,C,E) M-ECM or (B,D,F) SIS sheets. H&E stained. Scale bar represents 100  $\mu$ m.

The proliferation of C2C12 myoblasts (Figure 6A) and perivascular stem cells (Figure 6B) seeded on M-ECM and SIS scaffolds or seeded in empty wells (TC) was estimated from the Alamar Blue assay and all differences defined as  $p < 0.05$ . C2C12 metabolic activity was greater on seeded TC than SIS from day 1 onward, and greater than M-ECM from day 3 on. The metabolic activity of cells seeded on M-ECM did not change over the time course of the study,

but SIS and TC seeded cells promoted an increase from day 1 at days 5 and 3, respectively. In contrast, perivascular stem cells seeded on TC did not show alterations in metabolic activity over the time course of the study. Both M-ECM and SIS seeded scaffolds showed an increase in cell metabolism between days 1 and 5.

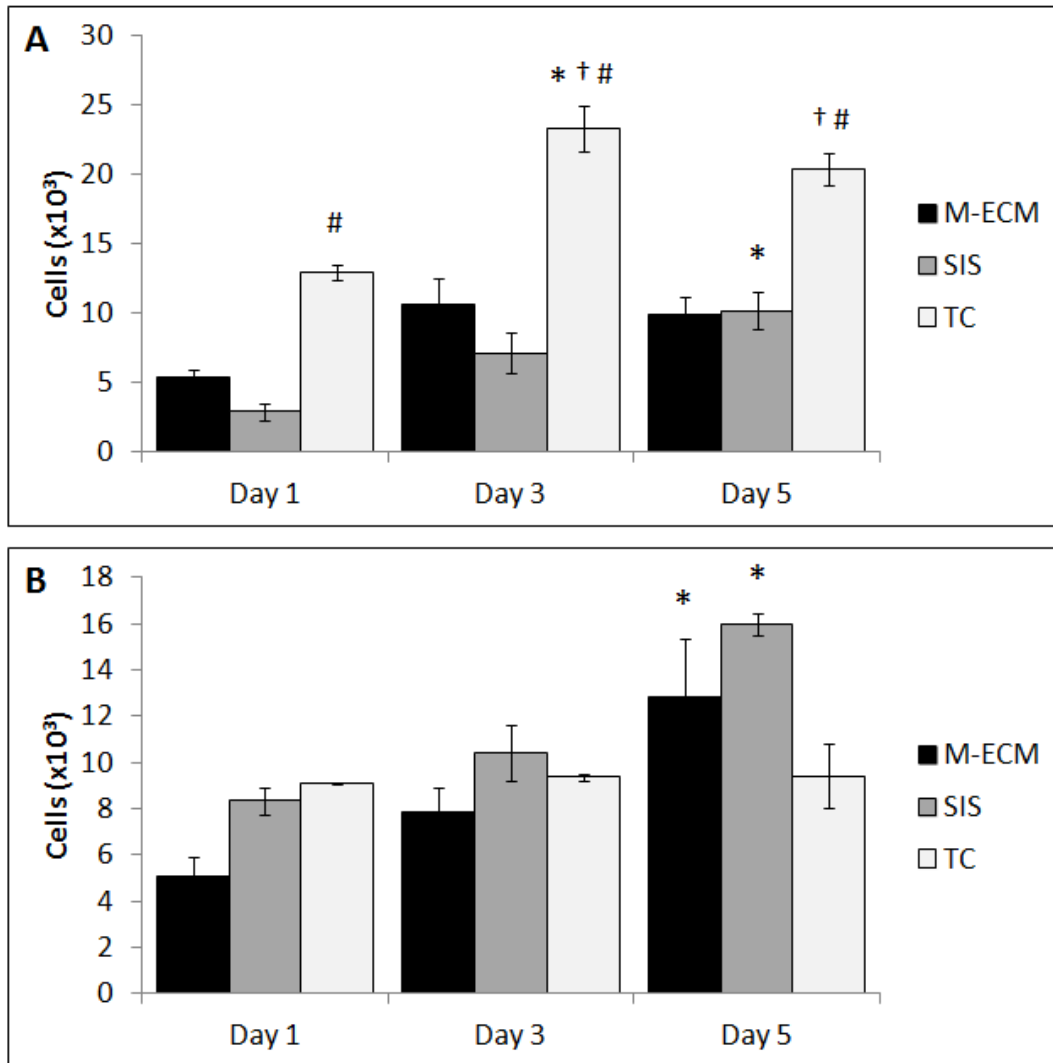


**Figure 6.** Alamar Blue assay for cellular metabolism of (A) C2C12 myoblasts and (B) perivascular stem cells seeded on the surface of M-ECM sheets, SIS sheets, or tissue culture plastic (TC) controls for 1, 3, and 5 days. Results normalized to standard curve of cells assayed on TC 4 hours after seeding. Significance defined as  $p < 0.05$  and \* denotes a difference from TC 4 hours after seeding.

day 1 within a group, # denotes a difference from SIS within a timepoint, and † denotes a difference from M-ECM within a timepoint.

#### **2.3.4 Acute evaluation of an M-ECM scaffold in a rat abdominal wall defect model**

M-ECM and SIS sheets were implanted in a partial thickness abdominal wall defect for 14 and 35 days and evaluated by histologic methods. At 14 days, both M-ECM and SIS scaffolds showed a robust mononuclear cell response with a dense accumulation of cells around the implants (Figure 7A-D). Compared to M-ECM, the SIS scaffold displayed a greater extent of degradation as shown by a highly fragmented scaffold appearance at 14 days (Figure 7B & D, asterisks). There were occasional multinucleate cells in direct contact with the M-ECM scaffold (Figure 8B, arrowheads) that was absent in the SIS group. Both implants showed angiogenesis around the scaffolds (Figure 7B & D). By 35 days, the mononuclear cell response had largely dissipated in both scaffolds and there was evidence of myogenesis within a more organized collagenous connective tissue. (Figure 7E-H)

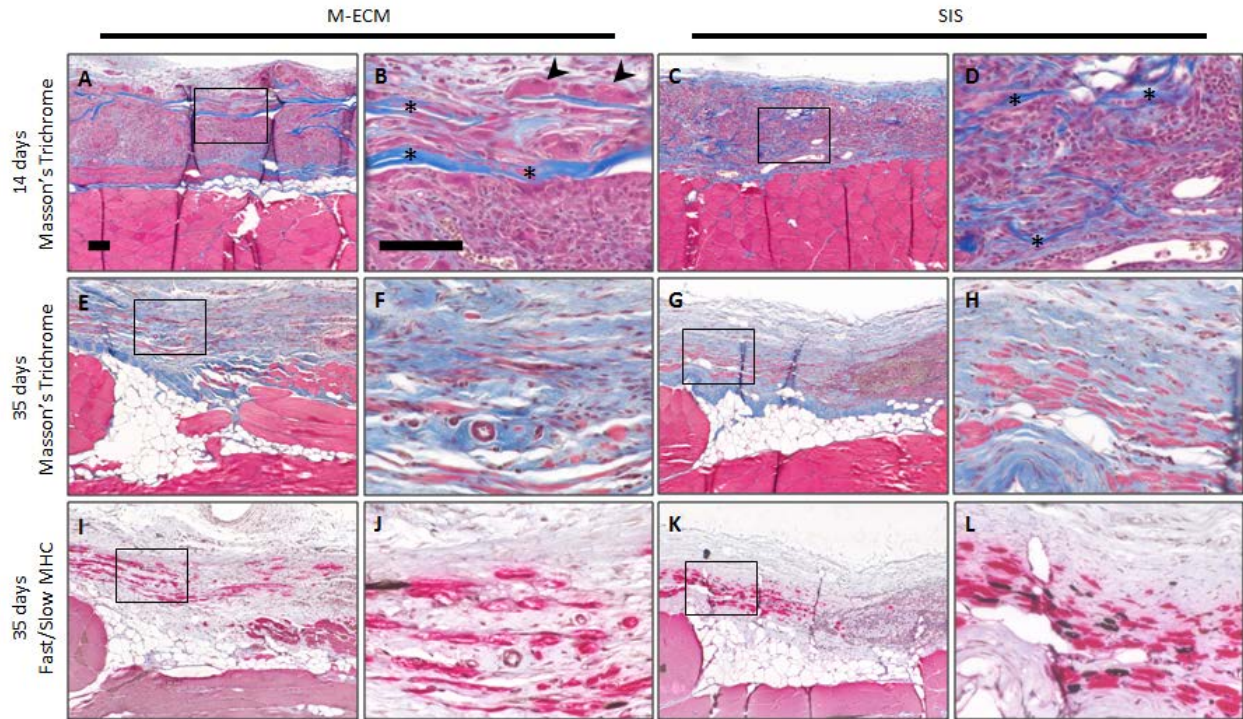


**Figure 7.** *In vivo* response to implanted (A-B,E-F,I-J) M-ECM and (C-D,G-H,K-L) SIS after (A-D) 14 and (E-L) 35 days. Low magnification (100X) images (A,C,E,G,I,K) are presented with black boxes denoting regions of interest for high magnification (400X) images presented directly to the right (B,D,F,H,J,L). Sections were stained with (A-H) Masson's Trichrome or (I-L) immunolabeled for fast (red) and slow (brown) myosin heavy chain (MHC). There are obvious scaffold remnants at 14 days for both scaffolds (asterisks), and multinucleate cells around M-ECM scaffold regions (arrowheads). Scale bars represent 100  $\mu$ m.

For M-ECM, there were still scattered regions in which the scaffold had not completely degraded, with collagenous bands of scaffold visible on histologic examination (Figure 8A, asterisks) with associated multinucleate cells (Figure 8A, arrowheads). The SIS scaffold was more completely degraded, with the infrequent exception of scattered small fragments (Figure 8B, asterisks) surrounded by a dense accumulation of mononuclear cells. Islands of small

diameter muscle fibers staining positive for slow or fast myosin heavy chain were occasionally found in the defect at the interface with the subjacent transversalis fascia. (Figure 7I-L) A greater proportion of the muscle stained positive for fast myosin than slow, consistent with the staining pattern in adjacent native muscle. There was no apparent difference in the amount or phenotype of new muscle observed between M-ECM and SIS scaffolds at the 35 day time point.

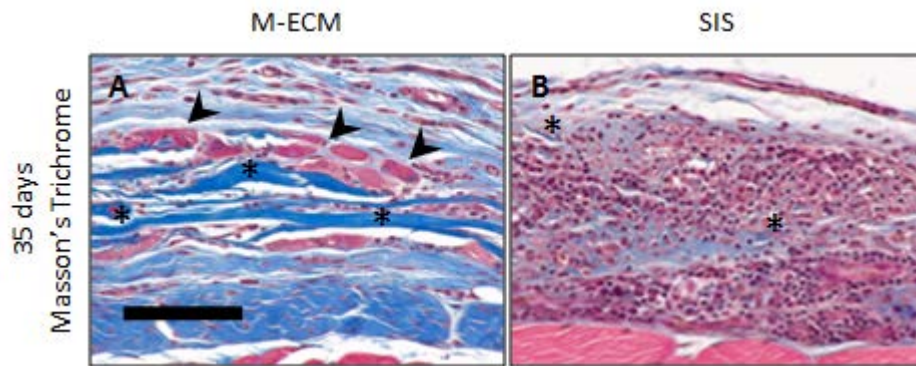


**Figure 8.** Areas of incomplete (A) M-ECM and (B) SIS scaffold degradation after 35 days in vivo after Masson's Trichrome staining. Scattered M-ECM scaffold remnants (asterisks) are apparent in some regions of the defect, but such regions are smaller and more diffuse for SIS. M-ECM scaffold remnants are also associated with multinucleate cells (arrowheads). Scale bar represents 100  $\mu\text{m}$ .

The unrepaired defect only control group at 35 days showed only a thin layer of collagenous connective tissue within the defect area, and little evidence of continued remodeling. (Figure 9A & B) There was a dispersed spindle shaped cell population and no observed myogenic cells.

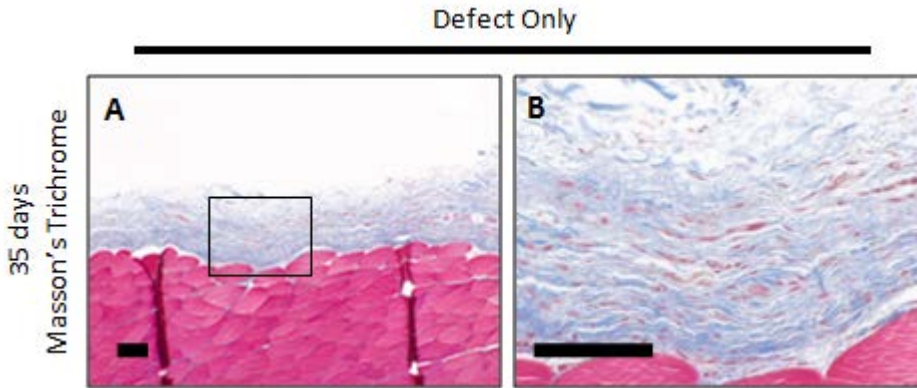


**Figure 9.** *In vivo* remodeling response to an unrepaired partial thickness abdominal wall defect after 35 days. Images were acquired at low magnification (A, 100X) with a black box denoting a region of interest for a high magnification (B, 400X) image. Scale bars represent 100 μm.

### **2.3.5 Application of the skeletal muscle decellularization method to cardiac and small intestine tissues**

Following the initial development and cytocompatibility of the chemical skeletal muscle decellularization protocol (see previous sections), this method was applied to sheets of porcine *psoas major* skeletal muscle, cardiac left ventricle, and small intestinal submucosa as shown in Figure 10A-C. Each tissue was decellularized, resulting in thin white sheets of ECM for use in subsequent analyses (Figure 10D-F).

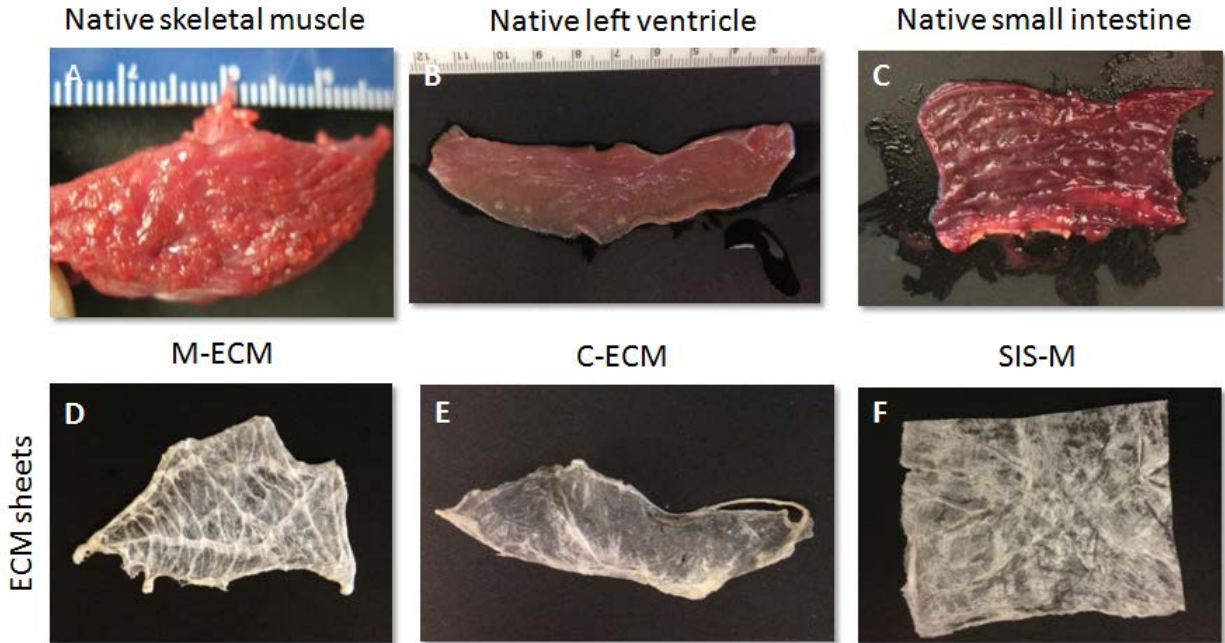


**Figure 10.** Native porcine psoas major skeletal muscle, left ventricle, and small intestine sheets (A-C) were decellularized using the muscle protocol to yield acellular ECM scaffolds (D-F).

### 2.3.6 Protein extraction and growth factor quantification

Soluble proteins remaining in M-ECM, C-ECM, SIS-M, SIS, and native tissues were extracted using urea-heparin extraction buffer and then were quantified using the BCA protein assay. The amount of protein extracted from M-ECM was  $2.30 \pm 0.57$  mg protein/g dry weight for M-ECM, which was two orders of magnitude less than the  $203.03 \pm 30.74$  extracted from native muscle tissue and one order of magnitude less than the  $23.04 \pm 2.52$  extracted from SIS. Similar quantities of protein were obtained from C-ECM and SIS-M extracts.

There was no detectable VEGF extracted (Figure 11A) from any of the decellularized tissues, though native muscle contained  $31.91 \pm 12.93$  ng VEGF/g dry weight. Total amounts of bFGF are presented in Figure 11B. M-ECM, C-ECM, and SIS-M retained bFGF, though in lower

amounts than SIS. Total bFGF content was found to be between 3.10-10.15 ± 2.34 ng bFGF/g dry weight in M-ECM, C-ECM, and SIS-M, which was less than the 75.22 + 19.57 found in SIS and the 39.70 + 8.28 ng bFGF/g dry weight found in native muscle or 125.4 ng/g in native small intestine.

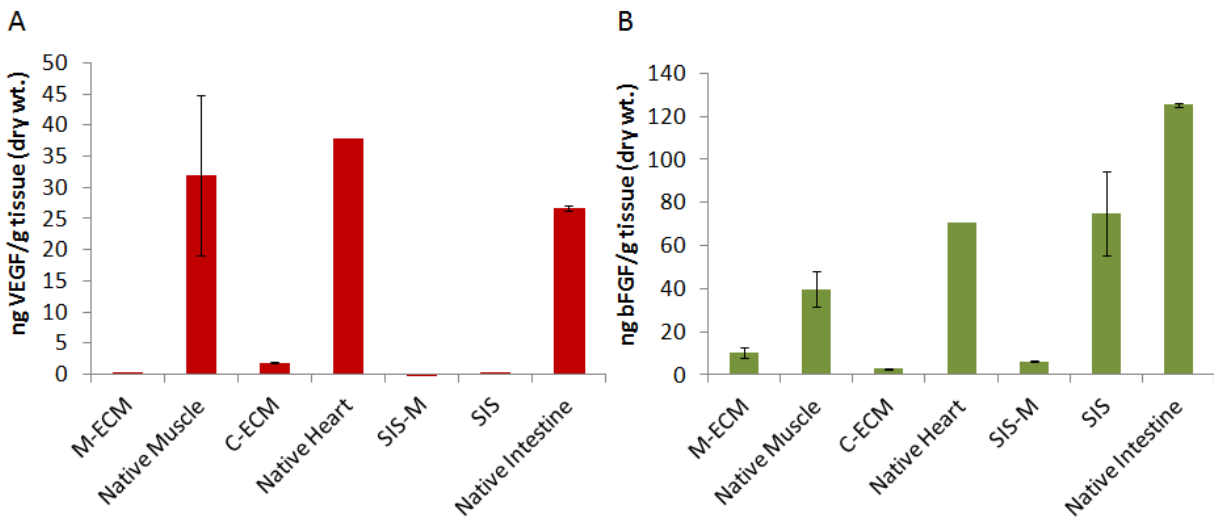


**Figure 11.** Biochemical growth factor analysis of M-ECM, C-ECM, SIS-M, and SIS compared to their native tissues. (A) Vascular endothelial growth factor (VEGF) and (B) basic fibroblast growth factor (bFGF) were quantified by ELISA from urea heparin extracted protein.

### 2.3.7 ECM staining and immunolabeling

ECM scaffolds and native muscle was stained with Herovici's Polychrome and Movat's Pentachrome stains as shown in Figure 12 and Figure 13, respectively. Herovici's staining of native muscle showed a distribution of thick type I collagen in the perimysium (pink/purple) and

type III collagen staining (blue) around individual muscle fibers consistent with previous studies (Figure 12A). [219, 220] Herovici's staining of M-ECM, C-ECM, SIS-M, and SIS showed thick Type I collagen bundles and dispersed strands of Type III collagen. (Figure 12B-E) Thicker bundles of both Type I and III collagen were observed in SIS scaffolds (Figure 12E). Movat's pentachrome showed the presence of elastin (black, arrows Figure 13). Elastin was primarily associated with blood vessels in native tissue, and in was localized to long strands that are possible remnants of blood vessels in each ECM. Staining patterns were similar for M-ECM, C-ECM, and SIS-M, though SIS had more dense protein as well as non-vessel associated elastin staining (Figure 13E).

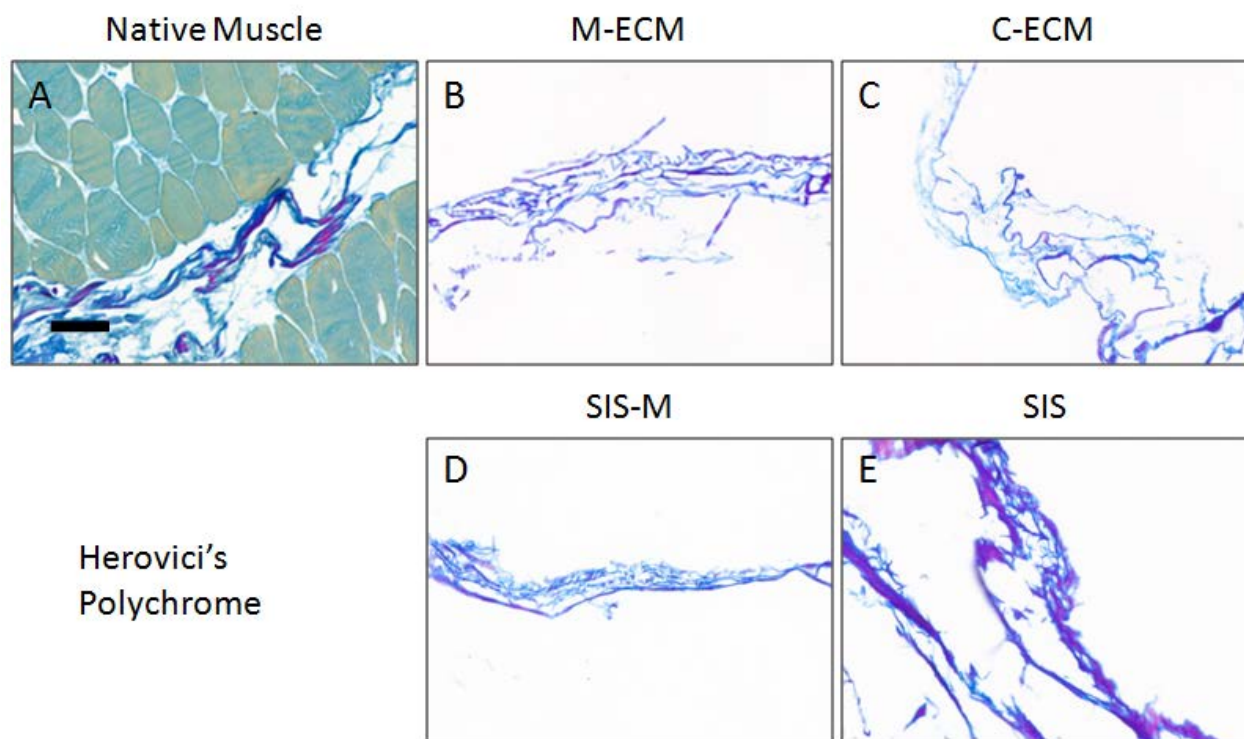


**Figure 12.** Herovici's Polychrome staining of native muscle (A), M-ECM (B), C-ECM (C), SIS-M (D), and SIS (E). Type I collagen fibers stain as pink/purple and Type III collagen stains blue. Scale bar represents 100  $\mu\text{m}$ .

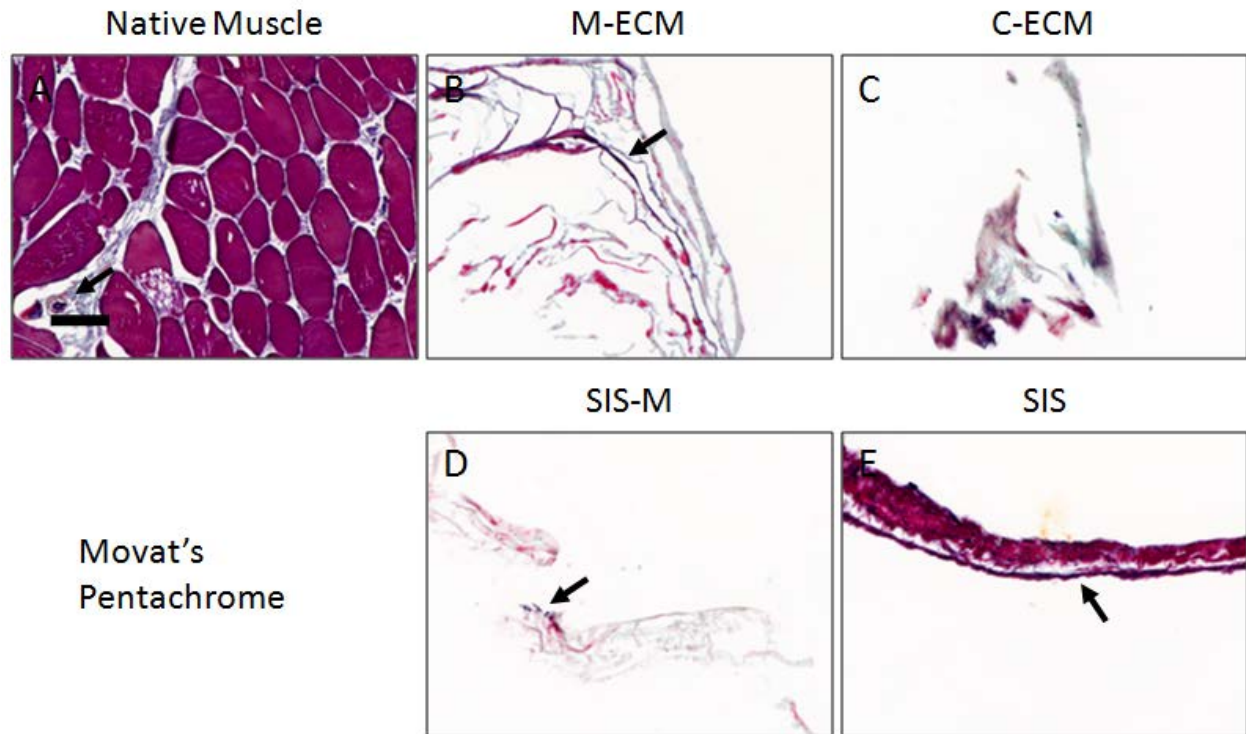


**Figure 13.** Movat's Pentachrome staining of native muscle (A), M-ECM (B), C-ECM (C), SIS-M (D), and SIS (E). Dense protein regions stain red and elastin stains black and is highlighted by arrows. Scale bar represents 100  $\mu\text{m}$ .

ECM scaffolds and native muscle tissue showed evidence of basement membrane proteins fibronectin (Figure 14), Type IV Collagen (Figure 15), and laminin (Figure 16). In native muscle, there was a clear localization of type IV collagen and laminin to the basement membrane surrounding muscle fibers (Figure 15A and Figure 16A). Fibronectin was found on basement membranes of native muscle as well as the interstitial connective tissue (Figure 14A). Each ECM showed abundant fibronectin staining (Figure 14), and isolated regions of Type IV collagen (Figure 15, arrows), with the most widespread staining visible in SIS. There were only occasional regions of laminin staining in all ECM groups (Figure 16, arrows). Antibody isotype controls verified the lack of non-specific staining (data not shown).

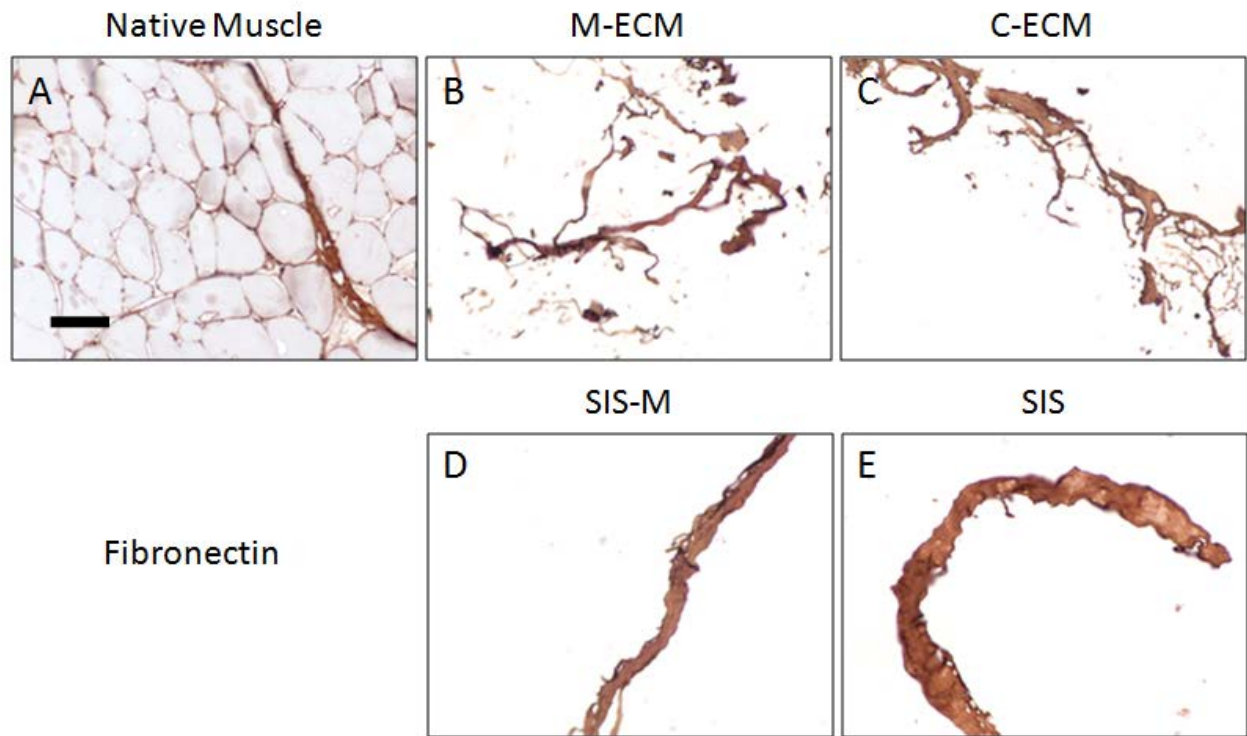


**Figure 14.** Fibronectin immunolabeling of native muscle (A), M-ECM (B), C-ECM (C), SIS-M (D), and SIS (E). Positive staining is indicated by brown ECM staining. Scale bar represents 100  $\mu\text{m}$ .

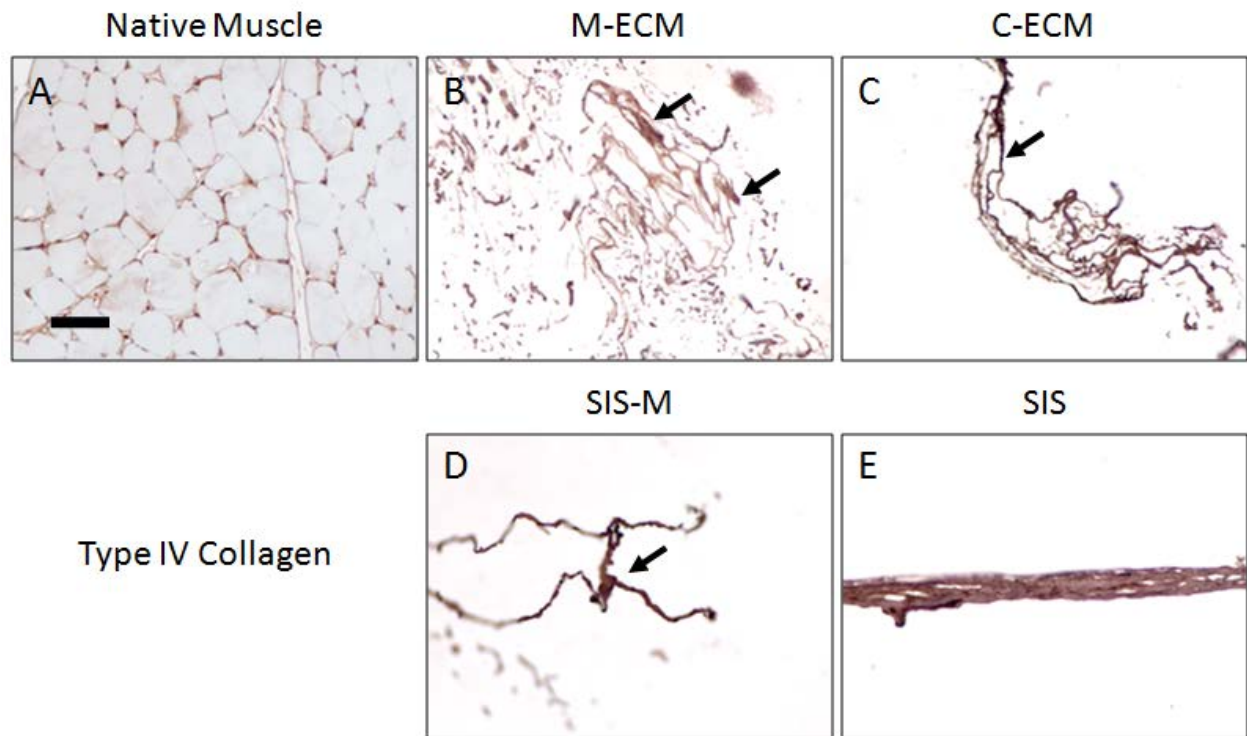


**Figure 15.** Type IV collagen immunolabeling of native muscle (A), M-ECM (B), C-ECM (C), SIS-M (D), and SIS (E). Positive staining is indicated by brown ECM staining and is highlighted with arrows. Scale bar represents 100  $\mu\text{m}$ .

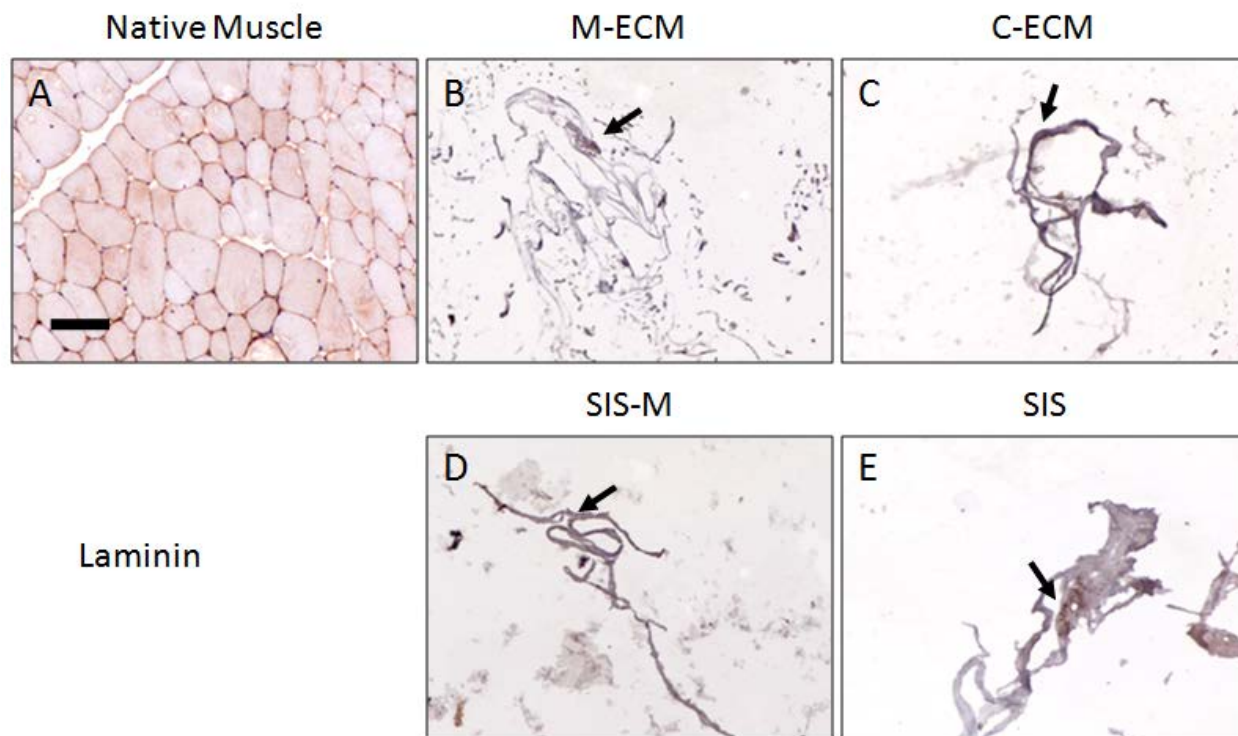


**Figure 16.** Laminin immunolabeling of native muscle (A), M-ECM (B), C-ECM (C), SIS-M (D), and SIS (E). Positive staining is indicated by brown ECM staining and is highlighted with arrows. Scale bar represents 100  $\mu\text{m}$ .

### 2.3.8 Sulfated glycosaminoglycan quantification

The results of the GAG assay are summarized in Figure 17. M-ECM contained  $0.88 \pm 0.8$   $\mu\text{g}/\text{mg}$  dry weight of sulfated GAGs after decellularization, which was similar to C-ECM and SIS-M with  $0.24 \pm 0.03$  and  $0.54 \pm 0.22$   $\mu\text{g}/\text{mg}$ , respectively. SIS had the greatest amount of GAGs with  $4.5 \pm 0.36$   $\mu\text{g}/\text{mg}$  dry weight.

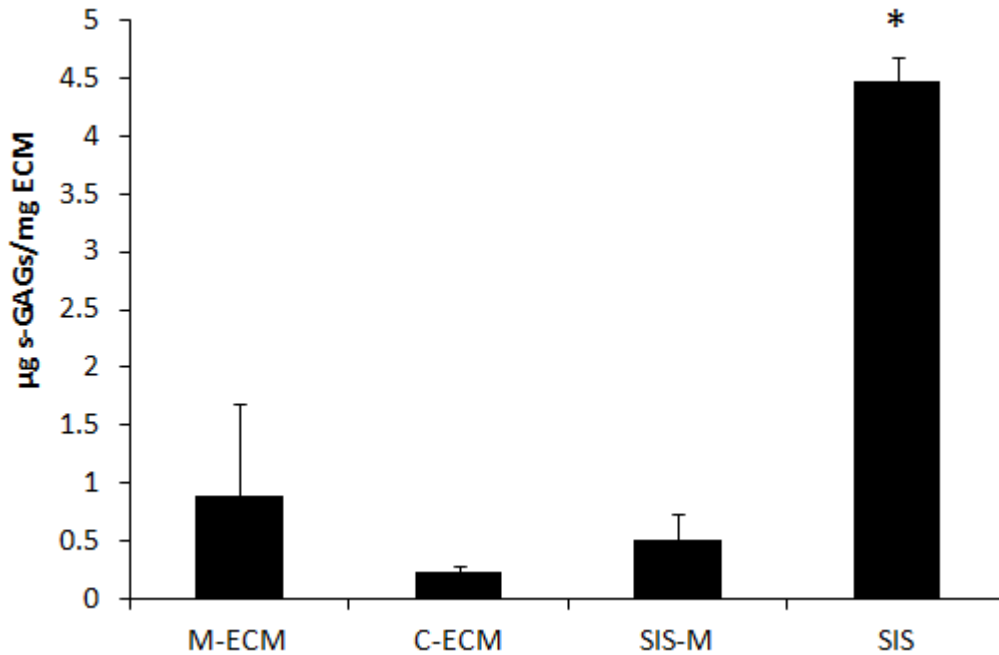


**Figure 17.** Sulfated GAG content of each ECM scaffold following enzymatic digestion. (\*) indicates a difference from all other groups ( $p < 0.05$ ).

## 2.4 DISCUSSION

A method for the preparation of skeletal muscle ECM scaffolds from a large animal tissue source is described in the present study. The M-ECM scaffold was shown to be thoroughly decellularized by established criteria while simultaneously preserving many of the components found in the native ECM. The bioactivity of the scaffold was evaluated and shown to affect the proliferative potential of muscle progenitor cells *in vitro* as well as the induction of a constructive remodeling response *in vivo*. Although differences were identified in the structure and composition of the ECM scaffolds prepared from skeletal muscle and small intestinal submucosa, no differences were present in their respective effects upon the remodeling of

skeletal muscle in a rodent model. This method was then applied to cardiac (left ventricle) and small intestinal submucosa tissue, where there was similar retention of bioactive factors in each tissue.

The method of preparation of an ECM scaffold can have profound effects upon the composition, ultrastructure, and subsequent host response to the scaffold following implantation. Skeletal muscle ECM scaffolds have been prepared and evaluated for the purpose of *in vivo* skeletal muscle reconstruction and several different decellularization approaches have been described. Merritt et al. provided a detailed assessment of the *in vivo* host response to acellular skeletal muscle and observed myogenesis at the scaffold/tissue interface, but found functional recovery only when mesenchymal stem cells were pre-seeded on the scaffold [101, 102]. This study utilized a relatively harsh decellularization protocol compared to methods described in the present study. Such harsh methods are effective at removing cellular material but also effectively denature matrix components [170, 171]. Other studies have reported the use of decellularized muscle tissue with less harsh decellularization protocols; however, quantification of decellularization was not attempted. While most visible nuclear material can be removed following decellularization attempts, cell remnants remain within the matrix, which can adversely affect *in vivo* remodeling. Consequently, less than ideal remodeling responses occur *in vivo* with the exception of those scaffolds preseeded with myogenic cells.[92, 93, 95, 98].

Although most clinical applications of ECM scaffolds have involved a non-homologous implantation site, there have been recent studies which suggest an advantage for the use of site specific ECM [84, 85, 88, 147, 149, 150, 152, 153]. The concept of tissue specificity in ECM scaffolds is predicated upon the concept that there is a unique structure and composition within each tissue, and even within different regions of individual tissues. The ECM of tissues and

organs provides a microenvironmental niche for resident cells that promotes and maintains site appropriate phenotype and function [221]. This niche environment is the sum of both structural and biochemical milieu that includes collagens, glycosaminoglycans, proteoglycans, and bound growth factors, among others that may influence myogenesis and the remodeling response. [46]

The M-ECM characterized in the present study maintains several of the factors found in native muscle tissue including basement membrane proteins and GAGs. Growth factors can be sequestered within the ECM, and FGF was shown in the present study to survive the decellularization process. Although assays used in the present study do not determine biologic activity, previous studies have shown that growth factors within decellularized tissues can stimulate cells in culture [222] [223, 224]. The differences in composition between M-ECM and SIS in the present study are most likely explained by not only the different tissue sources (muscle vs. small intestine), but also by the different decellularization techniques that were used. SIS is a thin material prepared primarily by mechanical methods from the parent small intestine tissue and a brief exposure to peracetic acid. M-ECM on the other hand uses enzymatic and detergent chemical methods that have different effects upon the matrix. This is supported by the similar values obtained for SIS-M following the same muscle decellularization protocol.

In addition to the retention of components found in the native ECM, M-ECM was shown to be cell compatible for a number of cell types *in vitro* as evaluated using histologic methods and with the Alamar Blue assay. C2C12 cells seeded on M-ECM and SIS were similar in their metabolic profile over the time course of the study, which was less than in non-ECM covered wells. Perivascular stem cells seeded on M-ECM and SIS, however, showed greater growth over time compared to non-ECM covered cells. These effects may have been due to the presence of ECM specific attachment proteins, or soluble growth factors that may have eluted from the

scaffold during culture. It should be noted that the Alamar Blue assay is a metabolic assay, which is not directly correlated to cell number in all circumstances.

The determinants of success for biologic scaffold remodeling *in vivo* are not fully understood, but empirical observations have proven informative. SIS that is prepared without chemical crosslinking has been shown to promote a constructive remodeling response, myogenesis, and partial restoration of function [105, 107]. Thoroughness of decellularization, as attained in the present study, avoids a pro-inflammatory response whereas ineffective decellularization is associated with a robust inflammatory response [129]. ECM scaffold degradation is another determinant of remodeling outcome. Degradation products of ECM scaffolds have been shown to have chemotactic and mitogenic effects on stem cells *in vitro* and *in vivo*, [211, 212] and inhibition of scaffold degradation is associated with less desirable outcomes [106, 107]. M-ECM, like SIS and other previously evaluated scaffolds, invokes a strong cellular response at early timepoints, which dissipates over time in a partial thickness abdominal wall defect model. M-ECM showed a morphologically different cell population, specifically, multinucleate cells, in direct contact with the scaffold at 14 days. Multinucleate cells were not seen in the tissue response to the SIS-ECM scaffold. M-ECM did appear to degrade more slowly than SIS, with some intact M-ECM scaffold fragments still visible at 35 days. There was extensive remodeling in areas where the M-ECM had degraded, with small islands of myosin heavy chain expressing muscle cells in the defect area in a very similar pattern to SIS at this time point. In contrast, the unrepaired defect only control, exhibited very little remodeling and no myogenesis confirming the positive influence of M-ECM and SIS scaffolds on the host response. Despite the numerous differences in the structure, composition, and early host responses between M-ECM and SIS, the remodeling characteristics and myogenesis at 35 days

were indistinguishable. It is possible that there will be additional divergence in the remodeling outcome at later time points when remodeling is complete.

The results of this aim show that a M-ECM scaffold can be prepared from a large animal source using an enzymatic and chemical processing method. The M-ECM conforms with established decellularization criteria while preserving factors found in native muscle ECM that may be beneficial to the host remodeling response. The M-ECM exerts biologic effects on myogenic cells *in vitro* and promotes positive remodeling characteristics in a rodent muscle defect model. However, when compared to the nonhomologous SIS there was no detectable advantage in using a tissue specific M-ECM scaffold, despite differences in the structure and composition of the two bioscaffold materials. ECM composition was maintained to a similar extent in resultant C-ECM and SIS-M ECM scaffolds, showing that this method is applicable to other tissues and that they alter the ECM to similar extents. Conventional SIS retained greater quantities of growth factors and GAGs, which is likely due to the stronger detergents and greater exposure time in the muscle decellularization protocol compared to SIS. Though compositional similarities were observed between tissues, relatively broad detection methods were utilized. Laminin and Type IV collagen, for example, encompass multiple isoforms that have divergent, tissue specific functions [69, 70, 225-228]. Likewise, there are multiple types of sulfated glycosaminoglycans (e.g. heparan sulfate and chondroitin sulfate) [229, 230] as well many possible post-translational glycosylation protein modifications. The total Type IV collagen, laminin, and glycosaminoglycan content evaluated in the present study was non-specific, and likely spanned different isoforms in different ratios for each tissue. Future studies investigating the roles of these specific isoforms are required to determine whether different isoforms directly

exert differences in the cell response to these scaffolds, and may act as a mechanism of ECM tissue specificity.

### **3.0 THE EFFECT OF SKELETAL AND CARDIAC MUSCLE EXTRACELLULAR MATRIX DEGRADATION PRODUCTS ON SKELETAL AND CARDIAC MUSCLE PERIVASCULAR STEM CELLS**

#### **3.1 INTRODUCTION**

Extracellular matrix (ECM) from decellularized tissues has been used as an inductive biologic scaffold for tissue reconstruction in several clinical applications such as rotator cuff repair [231, 232], ventral hernia repair [91, 97, 233-235], breast reconstruction [236], and heart valve replacement [237]. The decellularization process removes the majority of the tissues cell components, resulting in an implantable acellular scaffold composed of the native ECM [74, 130]. The utility of ECM scaffolds derives from their ability to remodel into site appropriate host tissue after implantation in a site of injury, a process termed constructive remodeling [73]. During this process, ECM scaffolds are rapidly infiltrated by mononuclear cells, fully degraded [71, 238], and replaced with a mixture of loose connective tissue and site specific functional cells (e.g. myogenic progenitors/myofibers in skeletal muscle) [105, 107]. This is in contrast with default wound healing, which proceeds through the development of a provisional scaffold and eventual dense fibrous scar tissue deposition [239]. ECM scaffolds have been prepared from numerous tissues including small intestine, urinary bladder [200, 240], dermis [235, 241], pericardium [109, 242], and recently, skeletal [108, 168, 178] and cardiac muscle [179, 186, 202]

tissues. The ECM from each of these source tissues has a composition and microstructure that is optimal for its resident cells, and it is from these differences that the concept of tissue specific ECM scaffolds has arisen. A tissue specific ECM hypothesis postulates that an ECM scaffold provides optimal biologic signals and/or microenvironment to cells derived from the same tissue.

The mechanisms of ECM constructive remodeling are only partially understood, several processes have been implicated in the response, and many of these are dependent on ECM degradation and subsequent release of matricryptic molecules [71, 238, 243]. These molecules are small fragments of the native ECM possessing new biologic activity that is not present in the intact parent ECM molecule [243-245]. Such matricryptic molecules have been described in biological contexts such as angiogenesis, cancer invasion, homeostasis, wound healing, and recently, during ECM scaffold degradation and remodeling [210, 243, 245]. ECM scaffold degradation products have shown chemotactic and mitogenic effects on stem cells *in vitro* [211, 246] and *in vivo* [210, 245, 246], and are a potential mediator of ECM remodeling.

Perivascular stem cells (PVSCs) belong to a multipotential, vessel associated stem cell population capable of osteogenic, adipogenic, chondrogenic, and myogenic differentiation *in vitro* and *in vivo* [217, 247]. PVSCs have been isolated and characterized from several fetal and adult tissues, which includes skeletal muscle [217, 247], placenta, bone marrow, pancreas, cardiac muscle (unpublished data), liver [248], and adipose tissue [217]. Their wide anatomical distribution has suggested a ubiquitous role in wound healing and regeneration of vascularized tissues. Furthermore, PVSCs isolated from different tissues have been proposed to possess different characteristics, such as differentiation capacity and surface marker expression, indicating tissue specific PVSC differences (unpublished data). This provides an opportunity to

examine a similar stem cell population derived from both skeletal and cardiac muscle anatomic locations, rather than skeletal muscle satellite cells for which there is no cardiac analogue.

The objective of the present study was to determine whether ECM scaffolds possess tissue specific inductive effects on PVSCs from the same donor and/or different tissue origin. Specifically, the effects of ECM degradation products derived from skeletal muscle, cardiac muscle, and non-muscle tissue were characterized on human skeletal and cardiac muscle derived PVSCs *in vitro*.

## **3.2 METHODS**

### **3.2.1 Overview of experimental design**

ECM scaffold degradation products were prepared *in vitro* from decellularized skeletal muscle (M-ECM), cardiac muscle (C-ECM), and small intestinal submucosa (SIS-M) using identical decellularization protocols. Small intestinal submucosa prepared via conventional methods (SIS) was also included to determine effects of different decellularization methods upon the response to the same ECM. PVSCs were exposed to ECM degradation products *in vitro* and ECM effects upon proliferation and differentiation were characterized.

### **3.2.2 Preparation of ECM degradation products**

Psoas major skeletal muscle, cardiac left ventricle free wall, and small intestine tissues were obtained from market weight pigs (approx. 100 kg) and decellularized using a modified version

of a previously established protocol for skeletal muscle ECM. Skeletal and cardiac muscle were sliced into 2.2 mm cross sectional sheets (transverse to the longitudinal axis) using a rotating blade. Small intestinal submucosa sheets were prepared by isolating the stratum compactum, muscularis mucosa, and submucosal from the other layers via mechanical delamination. All tissues were then frozen and lyophilized. The dried tissue sheets were delipidized by stirring in a chloroform/methanol solution (2:1 v/v, Sigma) for 30 minutes, followed by a graded series of ethanol (100, 100, 95, 70, and 50%) for 30 minutes each and then several water washes. Tissues were then frozen until further processing in a spinner flask at 70 RPM. Tissues were enzymatically processed with 0.2% Trypsin/0.2% EDTA (Sigma) at 37 °C for 2 hours, and then placed in alternating 20 minute hypotonic/hypertonic washes of deionized water and 2X PBS, respectively. Detergent treatment with 2% sodium deoxycholate (Sigma) for 5 hours was performed to solubilize cell components, followed by another pair of hypotonic/hypertonic washes and a fresh change of 2% sodium deoxycholate for 16 hours. A 1% Triton X-100 (pH=8, Sigma) solution was used to remove residual deoxycholate for 1 hour, which was followed by 2 washes in deionized water. Final decellularization was achieved after exposure to 0.1% peracetic acid/4% ethanol for 2 hours and residual chemicals removed via extensive washing: 2 washes with PBS and 2 washes in deionized water for 30 minutes each, 1X PBS for 16 hours, and 4 washes in deionized water. The resultant M-ECM, C-ECM, and SIS-M ECM sheets were frozen and lyophilized.

Lyophilized ECM was comminuted into a particulate form and partially enzymatically digested with 1 mg/ml pepsin (Sigma) in 0.01 M HCl for 48 hours at room temperature with agitation to final ECM concentration of 10 mg/ml (dry wt/volume). The resulting degradation products were frozen until addition to cell culture media. ECM digests were neutralized with

10X PBS (1/9 digest volume) and NaOH (1/10 digest volume), and diluted to desired concentrations with the appropriate media for each assay. Type I rat tail collagen (BD Biosciences) was neutralized according to manufacturer's instructions. Control buffers consisted of pepsin buffer (1 mg/ml pepsin in 0.01 M HCl without ECM) and pepsin-free buffer (0.01 M HCl only), which were neutralized and diluted in the same way as the ECM digests.

### **3.2.3 Skeletal and cardiac perivascular stem cell (PVSC) isolation and culture conditions**

Skeletal and cardiac muscle derived perivascular stem cells were isolated from human fetal skeletal and cardiac muscle tissue, respectively, from the same donor as previously described by Crisan et al. [217]. Human fetal tissues (17-23 weeks of development) were obtained following voluntary or therapeutic pregnancy interruptions performed at Magee-Womens Hospital, in compliance with the University of Pittsburgh Institutional Review Board protocol 0506176, and after obtaining informed consent from the patient for use of the tissues. Developmental age was estimated by medical history and measurement of foot length.

For skeletal muscle, cells were dissociated by cutting the fresh tissue into small pieces and incubating with collagenases I, II, and IV at a concentration of 1 mg/ml for 1 hour at 37 °C with gentle agitation. Remaining tissue fragments were then fully dissociated by mechanical separation with forceps, and incubated for an additional 10 minutes in collagenases with gentle agitation. For cardiac tissue, cells were dissociated by cutting the fresh tissue into very small pieces, mincing mechanically, and incubating in the dissociation solution containing collagenases I, II, and IV at a concentration of 1 mg/ml for 15-20 min at 37 °C with gentle agitation. Dissociated tissues were neutralized with an equal amount of DMEM (Dulbecco's modified Eagle's medium, Gibco) containing 10% fetal bovine serum (FBS, Invitrogen) and 1%

penicillin-streptomycin (P/S, Invitrogen). After centrifugation, pellets were washed, resuspended in PBS, and sequentially passed through 100- and 70- $\mu$ m cell strainers to obtain single cell suspension. Cells were then incubated in erythrocyte lysis buffer (155 mM NH<sub>4</sub>Cl, 10mM KHCO<sub>3</sub>, 0,1mM EDTA) for 10 min at room temperature. After centrifugation, cells were resuspended in PBS and passed through a 70- $\mu$ m cell strainer if debris is observed.

Fluorescent activated cell sorting (FACS) was performed to purify PVSCs from the skeletal and cardiac muscle tissues using a FACSAria flow cytometer (BD). CD56+ myogenic/natural killer cell (anti-CD56-PE-Cy7, Serotec, 1:100), CD45+ hematopoietic cell (anti-CD45-APC-Cy7, Santa Cruz Biotechnologies, 1:100), CD34+ endothelial cell (anti-CD34-APC, Becton-Dickinson, 1:100), and c-kit+ cardiac stem cell (anti-CD117-PE, Serotec, 1:100) populations were gated out of the single cell suspension, and PVSCs were positively selected for expression of pericyte markers CD146 (anti-CD146-FITC, Serotec, 1:100). Sorted PVSCs were plated at a maximum density of 2x10<sup>4</sup> cells/cm and cultured for 1 passage on gelatin-coated plates in endothelial cell growth medium (EGM2 complete, Lonza). PVSCs were subsequently expanded in proliferation medium (20% FBS, 1% penicillin/streptomycin, DMEM), which also maintained an undifferentiated phenotype, and all cells were used between passages 9-12.

### **3.2.4 PVSC myogenic differentiation**

The effect of skeletal and cardiac muscle ECM degradation products on skeletal and cardiac PVSCs was determined by immunolabeling for myogenic and cardiomyogenic phenotypic markers after differentiation culture conditions. Skeletal and cardiac muscle PVSCs each have different culture requirements to induce differentiation as shown in Figure 18.

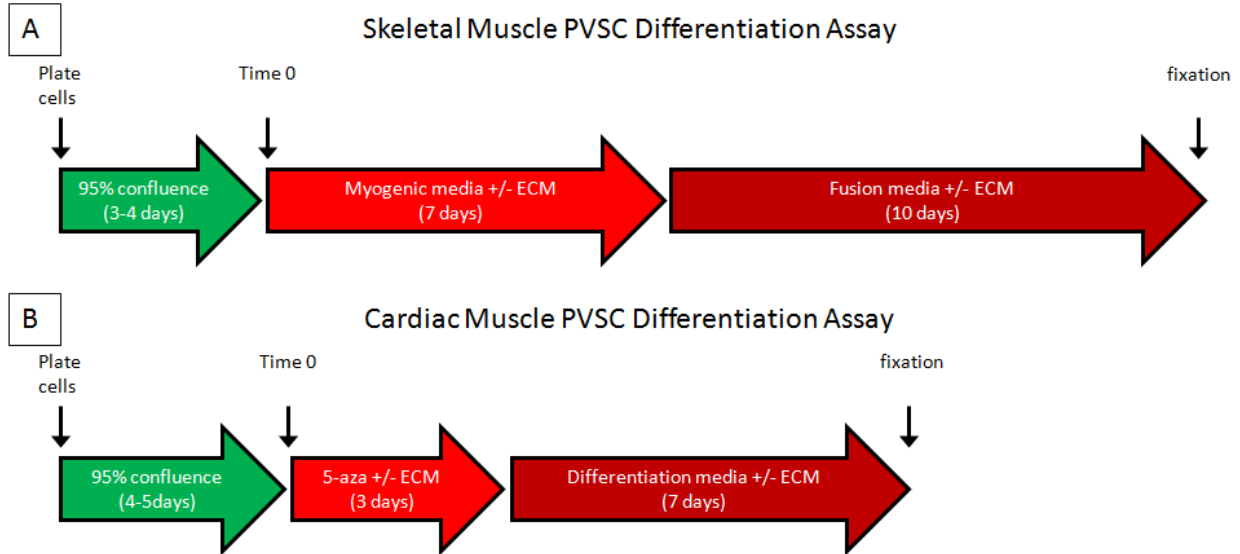


**Figure 18.** *In vitro* culture conditions for skeletal and cardiac muscle PVSC myogenic differentiation. PVSCs were plated, grown to confluency, changed to myogenic pre-conditioning media (with and without ECM degradation products) and finally changed to low serum fusion media (with and without ECM degradation products). Cardiac PVSCs were grown to confluency, pulsed with 5-azacytidine, and cultured in high serum cardiac differentiation media (10% FBS).

Skeletal muscle PVSCs (Figure 18A) were plated in 24 well plates at a density of 5,000 cells/cm<sup>2</sup> and grown to 95% confluence in proliferation media (typically 3-4 days). Proliferation media was then replaced with myogenic pre-conditioning media consisting of 10% FBS, 10% horse serum (Gibco), 1% chick embryo extract (Accurate Chemical), and 1% penicillin/streptomycin in DMEM for 7 days, and supplemented with neutralized ECM degradation products at a concentration of 100 µg ECM/ml, 100 µg type I rat tail collagen/ml (BD), or buffer controls (pepsin buffer or pepsin-free buffer). Full differentiation was induced by replacing the myogenic media with fusion media (1% FBS, 1% horse serum, 0.1% chick embryo

extract, 1% penicillin/streptomycin in DMEM) for 10 days. One half media changes were performed every 2 days for each media condition.

Cardiac muscle PVSCs were differentiated towards a cardiomyogenic lineage using MSC differentiation conditions (BFigure 18). Cardiac PVSCs were plated in 24 well plates at the same initial density as skeletal muscle PVSCs (5,000 cells/cm<sup>2</sup>) and grown to 95% confluency in proliferation media (typically 4-5 days). Proliferation media was then replaced with 10% FBS in DMEM supplemented with 10 nM 5-azacytidine (Sigma) for 3 days followed by differentiation media (10% FBS, 1% penicillin/streptomycin in DMEM) for an additional 7 days, and supplemented with neutralized ECM degradation products at a concentration of 100 µg ECM/ml, or buffer controls. One half media changes were performed every 2 days during differentiation culture.

Following differentiation, PVSCs were fixed within the well plates with 2% paraformaldahyde for 20 minutes at room temperature, and immunolabeled for skeletal and cardiac muscle differentiation markers. A subset of cells was fixed 1 day after initial plating to ensure PVSC phenotype expressing CD146 and NG2 surface markers. After fixation, cells were washed with PBS and simultaneously permeablized and non-specific protein binding blocked (1% bovine serum albumin, 2% horse serum, 0.1% Triton X-100, and 0.1% Tween 20 in PBS) for 1 hour. The blocking solution was decanted and immediately incubated with primary antibody diluted in blocking solution overnight at 4 °C. The following primary mouse monoclonal antibodies were used: anti-GATA4 (1:200, clone G-4, sc-25310, Santa Cruz Biotechnology), anti-MyoD (1:100, clone 5.8A, MA1-41017, Thermo Fisher), anti-fast myosin heavy chain (MHC) (1:250, clone My-32, M1570, Sigma-Aldrich), anti-cardiac MHC (1:200, clone BA-G5, ab50967, Abcam), and anti-sarcomeric MHC (1:250, clone MF-20,

Developmental Studies Hybridoma Bank). Cells were washed with PBS and incubated with secondary antibody diluted in blocking solution (1:250, goat anti-mouse Alexa Fluor 488 conjugate, Invitrogen) for 1 hour, followed by washing and nuclear counter staining with 4',6-diamidino-2-phenylindole (DAPI, Invitrogen). Each labeling condition was performed in triplicate wells for each of the three batches of ECM degradation products.

Individual wells were imaged via epifluorescence using an inverted microscope configuration (Zeiss, AxioVision), and at least 3 representative images were acquired from each well. Skeletal muscle specific differentiation was determined by expression of MyoD and fast MHC, and cardiac muscle differentiation determined by expression of GATA4 and cardiac MHC. PVSC fusion characteristics were quantified from the frequency and morphology of sarcomeric myosin heavy chain expressing cells. Since fusion was a rare event (less than 1% of cells) that typically localized to a few locations within the well, images were acquired to evaluate the maturity of fused cells. These fusion characteristics include: (1) the number of MHC expressing cells, (2) the total number of fused PVSCs defined as MHC expressing cells containing more than one nuclei, (3) the total length of MHC expressing cells, (4) the area of MHC expressing cells, (5) and the fusion index defined as the ratio of nuclei within fused MHC expressing cells to total nuclei per field.

### **3.2.5 BrdU incorporation assay for PVSC proliferation**

The effect of ECM degradation product conditioned media upon PVSC proliferation was determined by 5-Bromo-2'-Deoxyuridine (BrdU) incorporation in serum free conditions as well as serum conditions identical to those used during the differentiation experiments (Figure 19). The serum free assay (Figure 19A) began by plating PVSCs a 96 well plate at cell densities of

1,000 and 2,000 cells per well for skeletal muscle and cardiac muscle derived PVSCs, respectively. These cell seeding densities were determined empirically and differ due to the differing growth characteristics of skeletal and cardiac muscle PVSCs. Media was added to all empty wells to mitigate the effects of media evaporation in wells nearer the edge of the plate. Cells were allowed to attach and acclimate in growth media within the wells for 32 hours, which was then replaced with low serum media (0.5% FBS, 1% penicillin/streptomycin, DMEM) for 18 hours. Cells were then treated with serum free media supplemented with 10  $\mu$ M BrdU (Sigma) ECM (25, 50, or 100  $\mu$ g ECM/ml), Type I collagen (25, 50, or 100  $\mu$ g collagen/ml), pepsin and pepsin-free buffer (with dilution factors equivalent to those used for ECM conditions), or a high serum positive control media (5% FBS, 1% penicillin/streptomycin, DMEM). Each ECM batch was tested in quadruplicate wells. PVSCs were incubated in each treatment condition for 18 hours and fixed with 95% methanol for 15 minutes at room temperature.

The high serum assay (Figure 19B) was conducted in culture conditions that recapitulated those in the differentiation assay. Skeletal and cardiac muscle PVSCs were both seeded within 96 well plates at a density of 5,000 cells per well and allowed to attach and acclimate for 24 hours in growth media. Cells were then treated with high serum media supplemented with 100  $\mu$ g ECM/ml, 100  $\mu$ g collagen/ml, or pepsin and pepsin-free buffer controls. Myogenic preconditioning media was used for skeletal muscle PVSCs and differentiation media was the basal media for cardiac muscle PVSCs for the treatment duration. PVSCs were incubated for a total of 24 hours in each treatment condition, with the addition of concentrated BrdU (final concentration of 10  $\mu$ M in each well) during the final 4 hours of treatment followed by fixation.

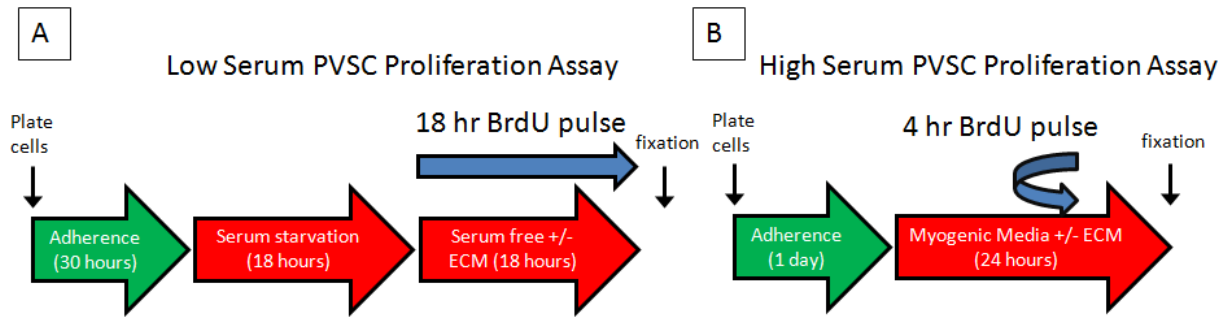


**Figure 19.** Summary of in vitro culture conditions for PVSC BrdU incorporation assays in serum free (A) and high serum (B) media with or without ECM supplementation. PVSCs in the low serum assay were serum starved for 18 hours and pulsed with ECM and BrdU for the following 18 hours. The high serum assay was conducted in high serum corresponding to the differentiation conditions in the respective skeletal and cardiac muscle differentiation assays.

BrdU incorporation was quantified via immunofluorescent labeling and imaging of PVSCs within wells. Non specific protein binding was blocked with 1% bovine serum albumin in PBS for 1 hour at room temperature. Plates were then decanted and immediately incubated with mouse anti-BrdU primary antibody diluted in blocking solution (1:1000, clone G3G4, Developmental Studies Hybridoma Bank) overnight at 4 °C. Plates were washed and incubated with secondary antibody diluted in blocking solution (1:250, goat anti-mouse Alexa Fluor 488 conjugate, Invitrogen) for 1 hour, and nuclei labeled with DAPI (Invitrogen). Mosaic images (composed of 35 individual 100X magnification images) that encompassed entire wells were acquired automatically using AxioVision software (AxioVision v4.7.1, Zeiss). The number of cells incorporating BrdU and the total number of nuclei within each well were quantified from the mosaic images automatically using a custom algorithm (Appendix A) developed with ImageJ software (National Institute of Health, Bethesda, MD). In brief, the original images were split into blue and green color channels and processed to remove background fluorescence, enhance

contrast, and count the number of nuclei and BrdU staining cells based on size exclusion (Figure 20). Only nuclei colocalized with BrdU staining were counted as BrdU positive cells. The percentage of total nuclei with BrdU incorporation was determined for each treatment and expressed as a percent change from the pepsin-free buffer condition.

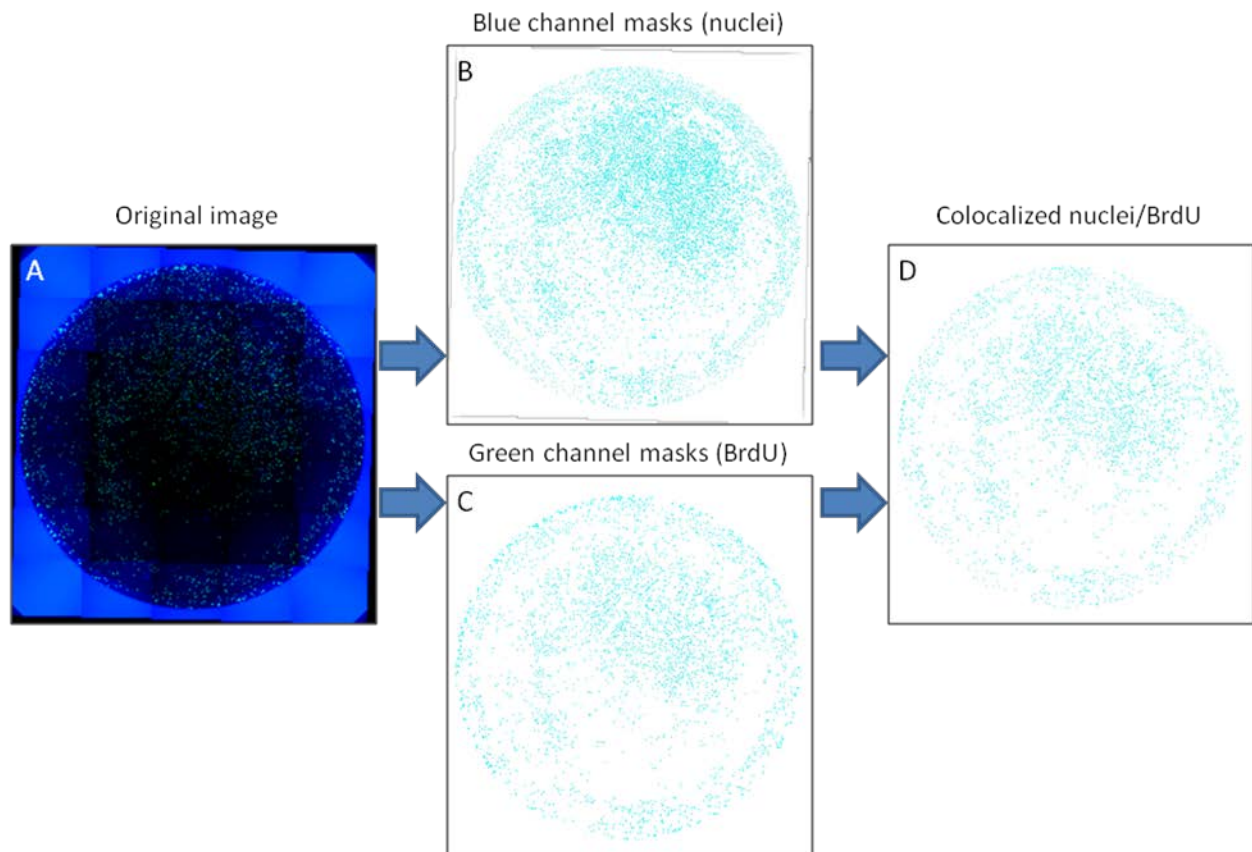


**Figure 20.** Example outputs of a PVSC seeded well stained and analyzed for BrdU incorporation using a custom ImageJ algorithm. The original mosaic image (A) was split into blue and green color channels, processed, and size gated to count the number of nuclei (B) and BrdU staining nuclei (C) from the ImageJ output mask images. Only blue/green colocalized masks were counted as positive BrdU incorporation (D).

### **3.2.6 Statistical analysis**

All values are reported as the mean  $\pm$  standard deviation. Statistical differences between ECM treatments in the serum free proliferation assay were determined with a two-way analysis of variance (ANOVA) for the factors ECM treatment and concentration with a post-hoc Tukey's test. Statistical significance for the high serum proliferation assay was determined using a one-way ANOVA with post-hoc Tukey's test. Significant differences were defined as a p-value  $<$  0.05.

## **3.3 RESULTS**

### **3.3.1 PVSC myogenic differentiation**

Skeletal and cardiac muscle PVSCs were differentiated at high confluence with or without ECM degradation products, and both PVSC cultures were affected by the addition of ECM. The initial PVSC phenotype was confirmed as co-expressing the pericyte surface markers CD146 and NG2 (Figure 21A-B), while also not expressing skeletal or cardiac muscle differentiation markers such as GATA4, MyoD, and sarcomeric MHC (Figure 21C-E). During the course of culture with ECM and Type I collagen only, PVSCs assumed an elongated and contractile phenotype. Highly confluent cell sheets would contract and begin to detach from the edges of the well inward and care was necessary to avoid full detachment during media changes or staining. Cell contraction and elongation was also evident from the shape of the nuclei, which also presented with an elongated aspect ratio. This effect was most pronounced in M-ECM, C-ECM, and SIS treatment

groups, though it was also observed to a lesser extent in SIS-M and Type I collagen treated wells.

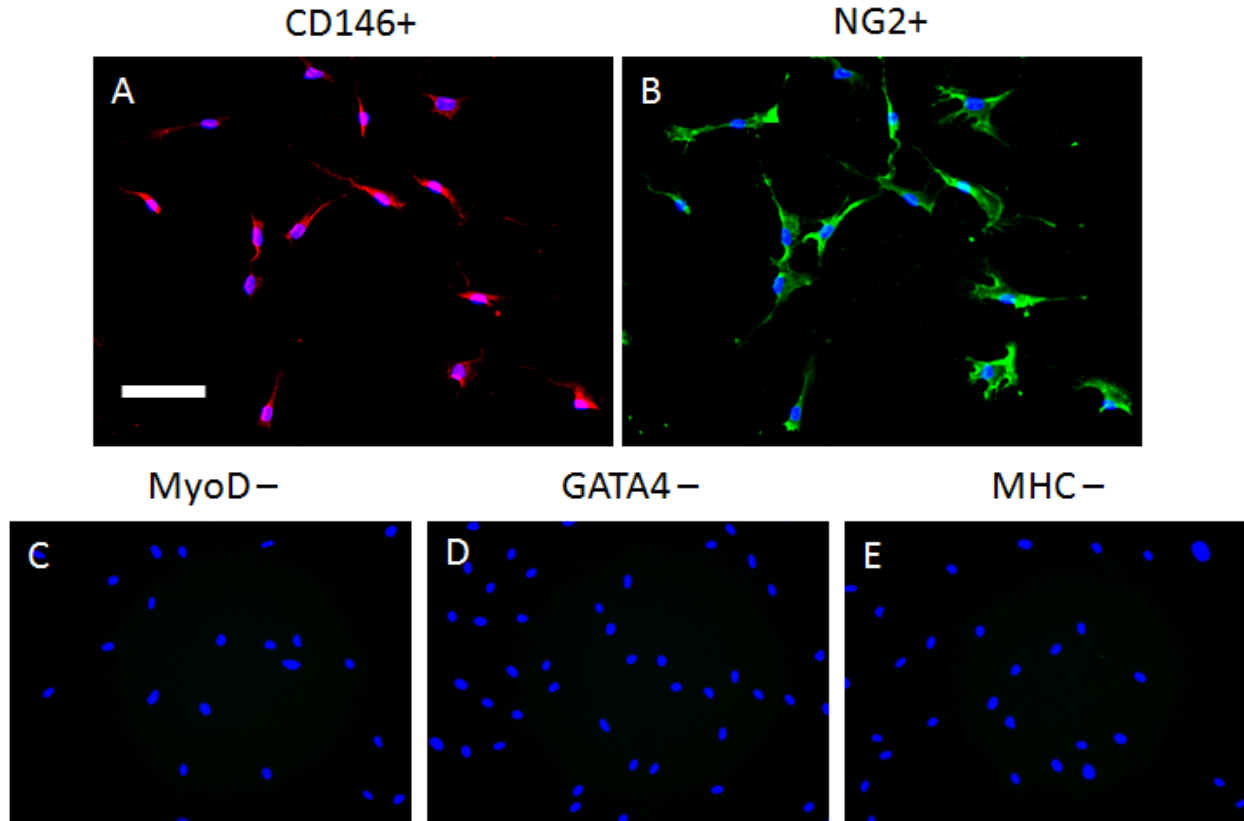
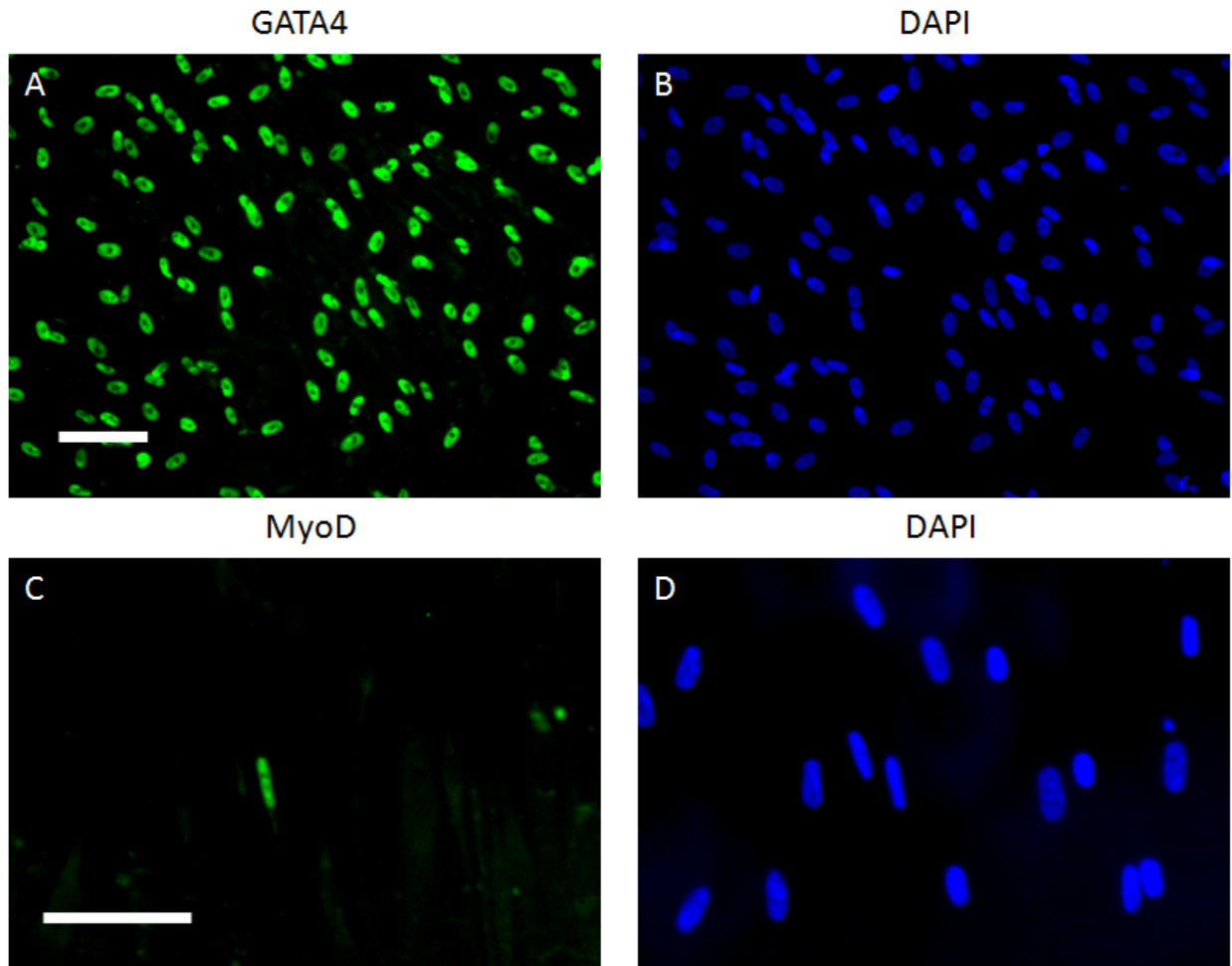


Figure 21. The initial skeletal and cardiac muscle PVSC phenotype prior to myogenic differentiation conditions. PVSCs co-expressed pericyte markers CD146 (A) and NG2 (B), while not expressing MyoD (C), GATA4 (D), or sarcomeric MHC (E). Scale bar represents 100  $\mu$ m.

Under these differentiation conditions, PVSCs expressed a combination of skeletal and cardiac muscle differentiation markers that are not present in non-differentiating culture conditions. Skeletal muscle PVSCs, even in the absence of ECM, highly expressed the cardiac associated marker GATA4 in approximately 90% of cells. In contrast, the early myogenic commitment marker MyoD was only very rarely expressed in less than 0.01% of cells. ECM treatment and Type I collagen did not affect these expression characteristics.



**Figure 22.** Skeletal muscle PVSC expression of GATA4 and MyoD following differentiation without ECM. Nearly all cells expressed GATA4 (A-B, green), while there was only extremely rare expression of MyoD (C-D, green). These results were also typical following each ECM treatment. Nuclei were labeled with DAPI (blue). Scale bars represent 100  $\mu\text{m}$ .

Mature muscle contractile markers were affected by the addition of ECM degradation products. ECM free conditions expressed a mixed phenotype of cardiac and fast skeletal muscle myosin heavy chain, and rarely, cell fusion. ECM treatment induced low levels of cardiac MHC expression in approximately 50% of cells, which was not found in pepsin control treated wells

(Figure 23). This expression pattern was found in mononuclear and fused PVSCs and was similar for each ECM treatment.

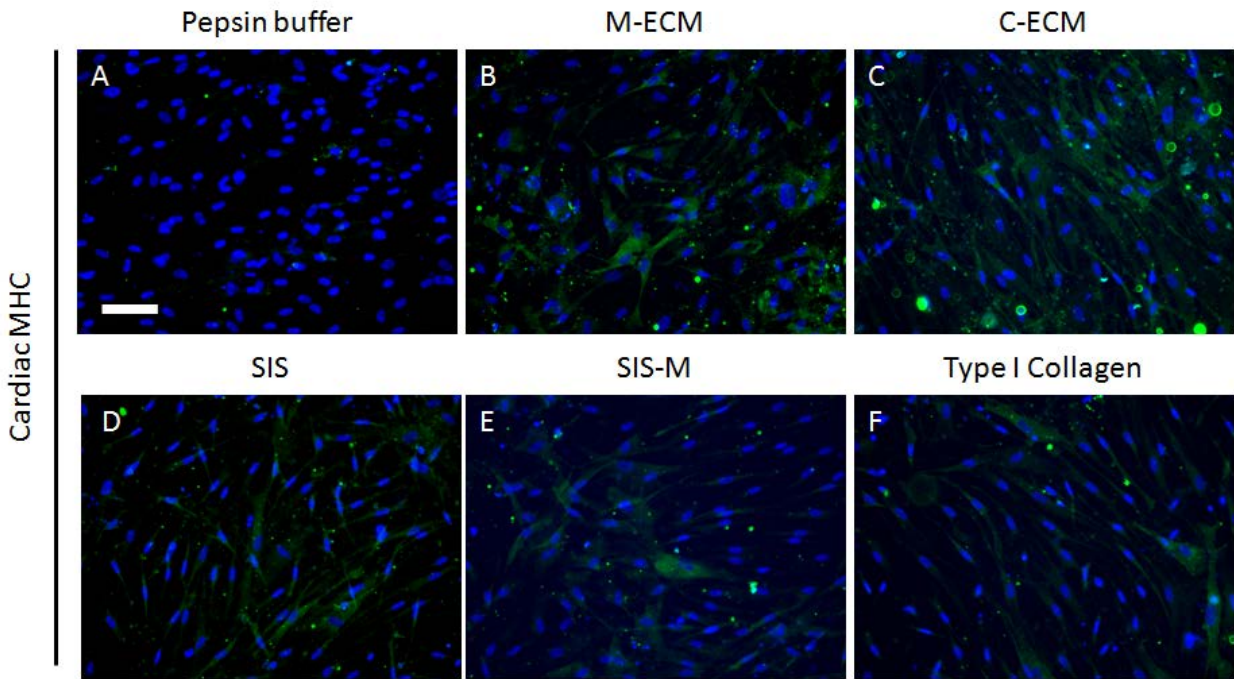


**Figure 23.** Cardiac MHC expression (green) in skeletal muscle PVSCs following differentiation in pepsin control buffer (A), ECM degradation products (M-ECM (B), C-ECM (C), SIS (D), and SIS-M (E)), or purified Type I collagen (F). Nuclei were labeled with DAPI (blue). Scale bar represents 100  $\mu\text{m}$ .

Fast skeletal muscle MHC was not as prevalent as cardiac MHC, though was also increased by ECM treatment (Figure 24). The majority of cells expressing fast MHC were fused rather than mononuclear cells.

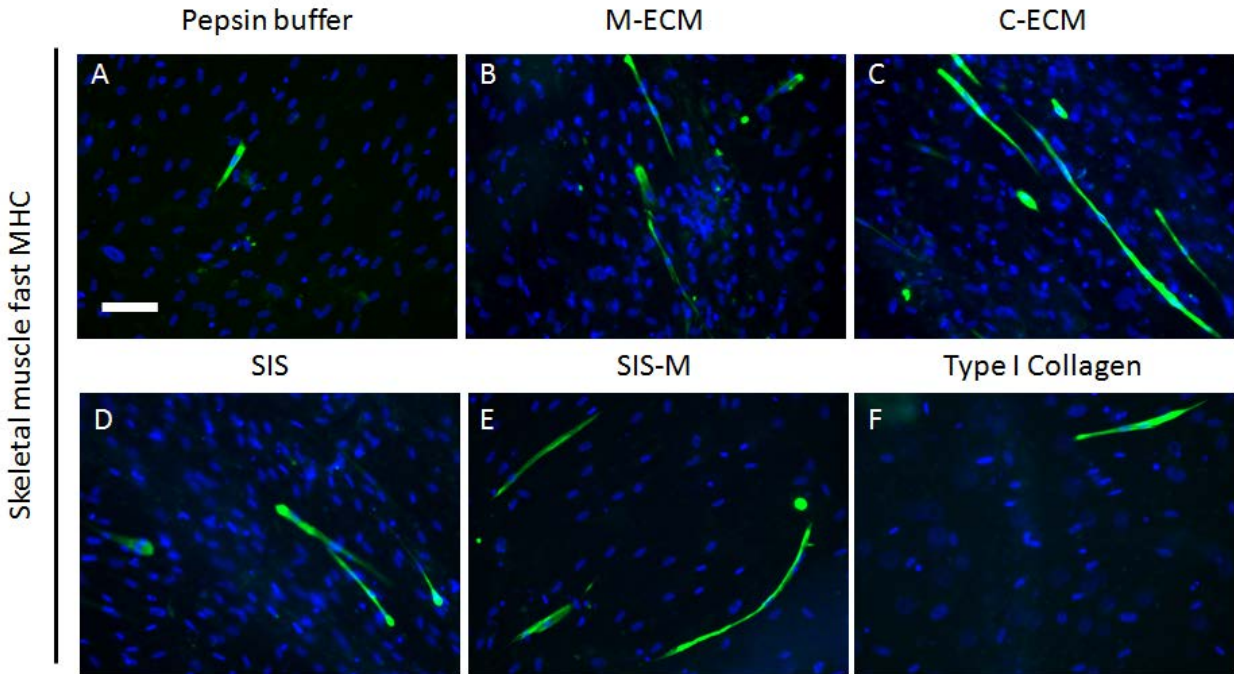


**Figure 24.** Fast skeletal muscle MHC expression (green) in skeletal muscle PVSCs following differentiation in pepsin control buffer (A), ECM degradation products (M-ECM (B), C-ECM (C), SIS (D), and SIS-M (E)), or purified Type I collagen (F). Nuclei stained with DAPI (blue). Scale bar represents 100  $\mu$ m.

Fused cells expressing sarcomeric MHC without ECM treatment (buffer or Type I collagen) had smaller cell areas and fewer nuclei per cell, and were less numerous than with ECM treatment (Figure 25). Though rare, ECM treatment increased fusion, which would occur in localized regions in the well plate. SIS increased the total number of fused cells (MHC positive cells containing more than 1 nuclei) relative to pepsin buffer and SIS-M. However, only M-ECM and C-ECM treatment resulted in an increase in the number of nuclei per fused cell. No treatment affected the total area of MHC expressing cells.

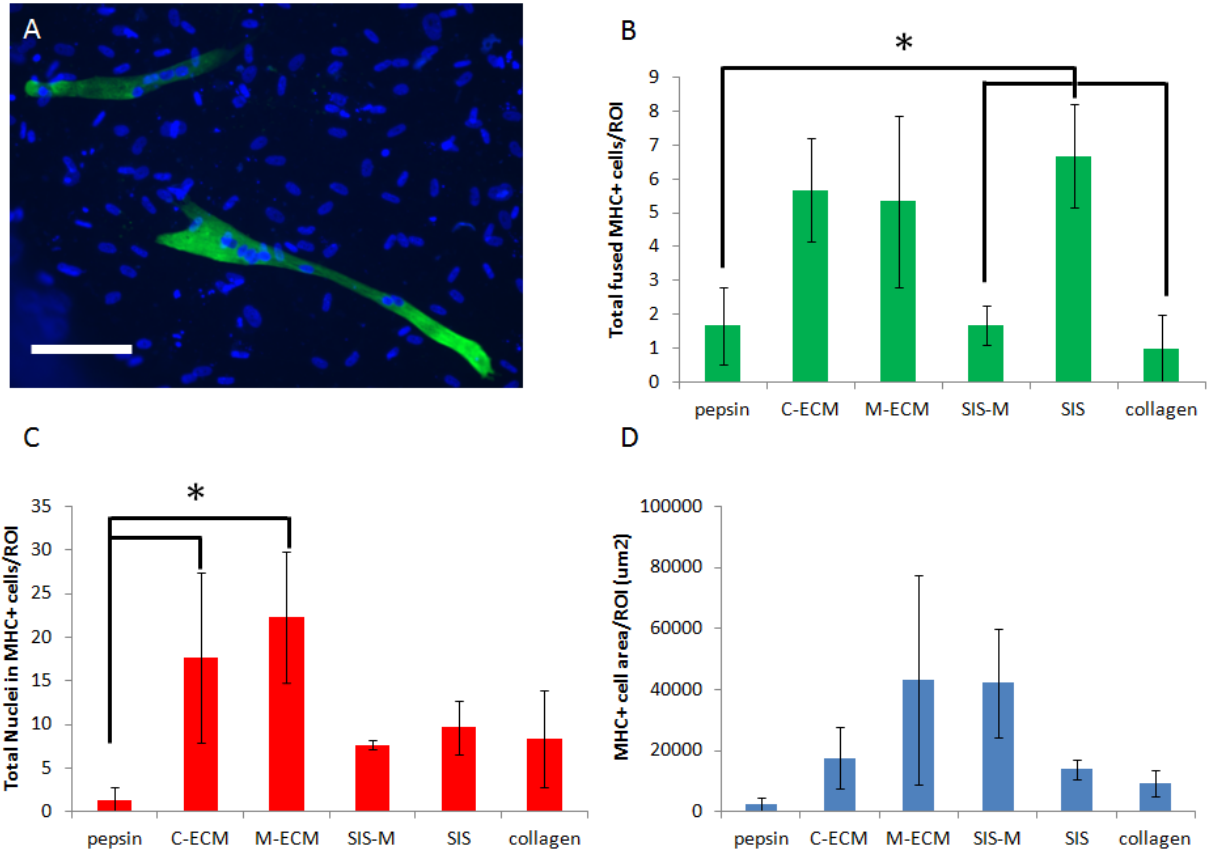


**Figure 25.** Skeletal muscle PVSC fusion analysis using sarcomeric MHC expression after exposure to pepsin buffer, M-ECM, C-ECM, SIS-M, or SIS degradation products, or Type I collagen. Fused cells (A, green) were analyzed for total number of fused MHC+ cells (B), total nuclei within MHC+ cells (C), and total MHC+ cell area (D). Statistically significant differences were determined by two-way ANOVA ( $p < 0.05$ ) and denoted with (\*). Scale bar represents 100  $\mu\text{m}$ .

Unlike skeletal muscle PVSCs, cardiac PVSC differentiation was not affected by the addition of ECM degradation products. Cardiac PVSCs expressed very high levels of GATA4 similar to skeletal muscle PVSCs, though they were not competent for cell fusion or expression

of any other differentiation markers. Cell contractility and elongation was observed after ECM treatment, muscle contractile markers were not apparent (Figure 26).

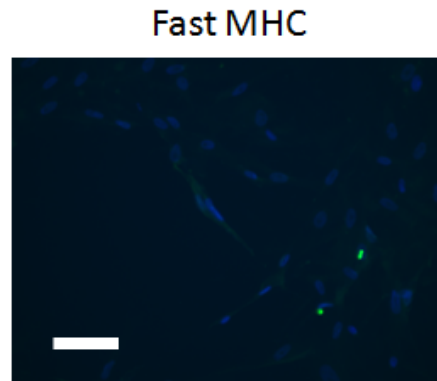


**Figure 26.** Cardiac PVSCs did not express mature myogenic markers. Scale bar represents 100  $\mu$ m.

### **3.3.2 BrdU incorporation assay for PVSC proliferation**

ECM degradation products were added to skeletal and cardiac muscle PVSCs in serum free and high serum conditions and expressed as the % change in BrdU incorporation with respect to the pepsin free buffer condition. ECM degradation products in serum free media (Figure 27) had a minimal effect on skeletal muscle PVSC proliferation, and only C-ECM induced a slight decrease in BrdU incorporation compared to pepsin buffer, with a non-dose dependent decrease of 24-50% compared to pepsin free buffer. SIS degradation products increased proliferation in cardiac PVSCs (6-32% increase) compared to pepsin buffer (17% decrease-15% increase) and Type I collagen (8% decrease-21% increase).

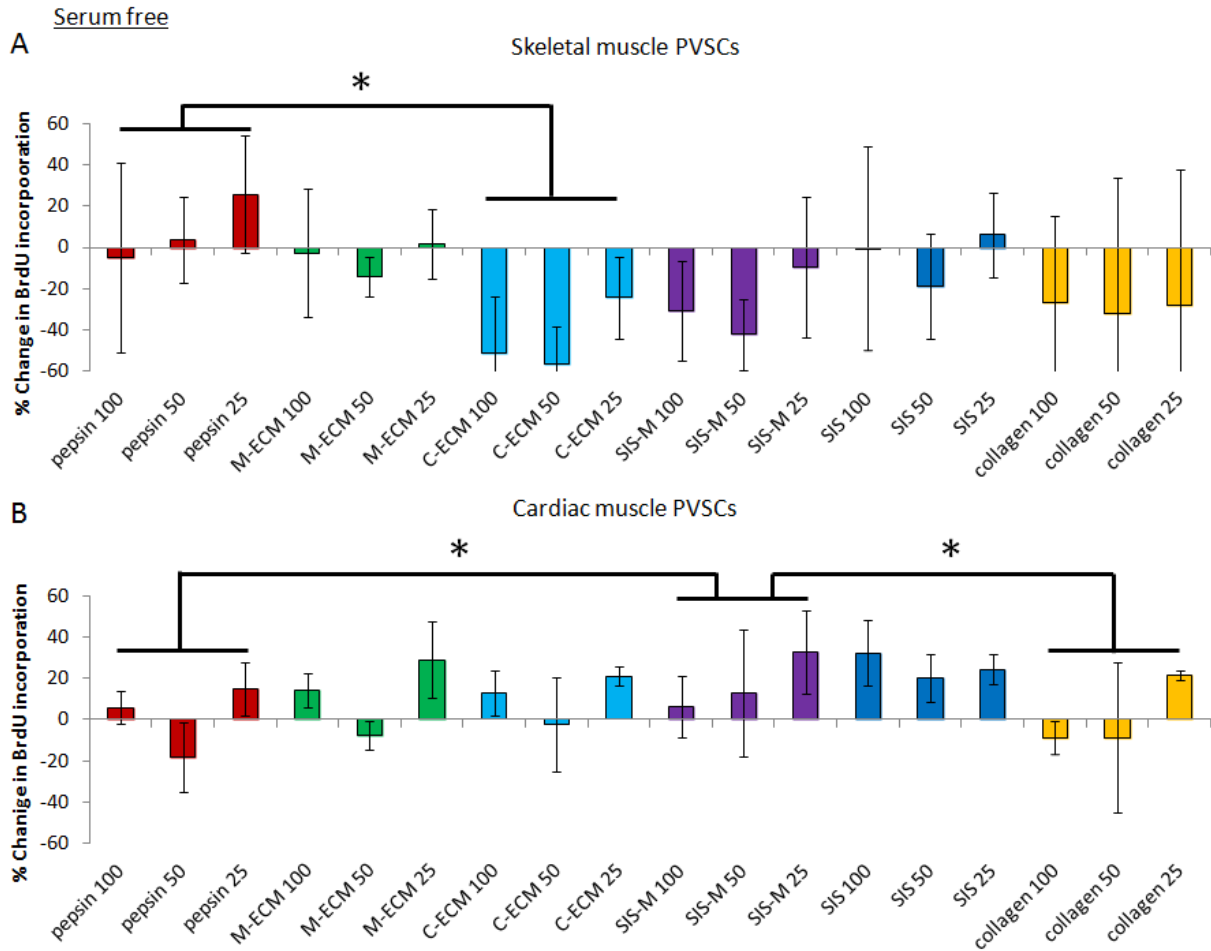


**Figure 27.** BrdU incorporation in skeletal muscle (A) and cardiac muscle (B) PVSCs with ECM exposure in low serum conditions. Each treatment was applied at 100, 50, and 25  $\mu\text{g/ml}$  concentrations. Values were normalized to untreated cells without ECM or pepsin buffer. Statistically significant differences were determined by two-way ANOVA ( $p < 0.05$ ) and denoted with (\*). Bars over groups of concentrations indicate that there was a difference due to treatment group, but not due to a concentration or interaction effect.

In high serum conditions, all ECM treatments and Type I collagen reduced BrdU incorporation in both skeletal (Figure 28A) and cardiac muscle PVSCs (Figure 28B). Skeletal muscle PVSCs exhibited a 5% increase in BrdU incorporation for pepsin buffer controls

compared to a 32-42% decrease for various ECM treatments, which were not statistically different from each other. Cardiac PVSCs were also reduced from a 0% change for pepsin buffer to a 32-52% decrease for ECM treatments, though no ECM treatments were statistically different.

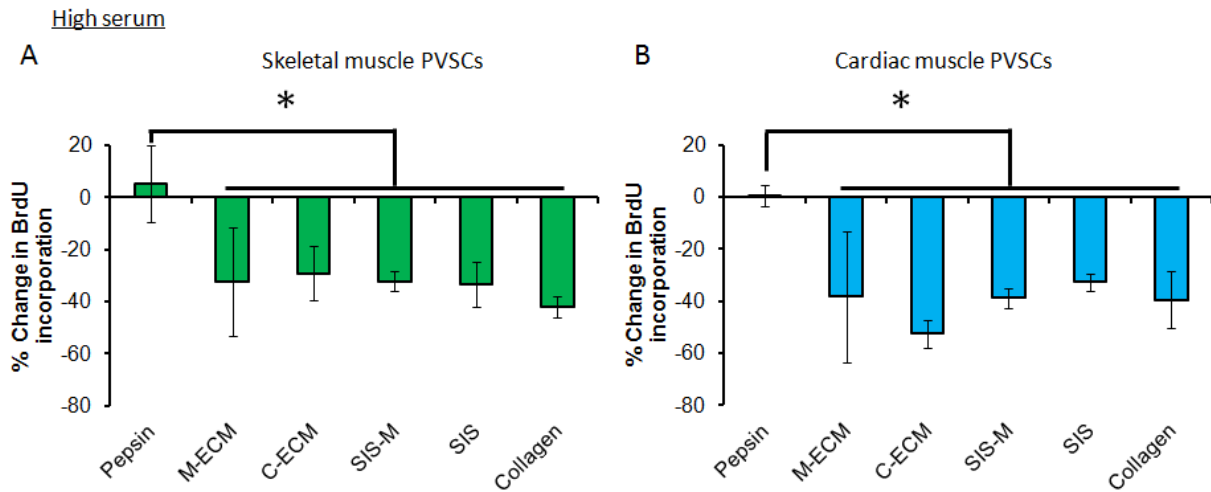


**Figure 28.** BrdU incorporation in skeletal muscle (A) and cardiac muscle (B) PVSCs with ECM exposure in high serum conditions. Statistically significant differences were determined by one-way ANOVA ( $p < 0.05$ ) and denoted with (\*). Each treatment resulted in a significant decrease in BrdU incorporation compared to pepsin buffer control.

### 3.4 DISCUSSION

The present study showed that PVSCs derived from skeletal and cardiac muscle vary in their *in vitro* myogenic differentiation potential and their responsiveness to muscle and non-muscle ECM

scaffold degradation products. Skeletal muscle PVSCs differentiated towards a myogenic phenotype coexpressing both skeletal and cardiac muscle markers, and with increased fusion following ECM treatment with M-ECM, C-ECM, and SIS. Cardiac PVSCs, however, did not effectively express contractile markers or fuse in culture, and ECM exposure did not change this response. Relatively small changes in proliferation were induced by ECM degradation products for PVSC types in low serum conditions in which C-ECM decreased skeletal muscle PVSC proliferation while SIS increased cardiac PVSC proliferation. Both ECM treatment and Type I collagen in high serum conditions decreased proliferation for both skeletal and cardiac muscle PVSCs.

ECM scaffolds are prepared by tissue decellularization, and have been shown to be effective in promoting a constructive remodeling response in musculotendinous tissue [105], cardiac tissue [203], liver [85], esophagus [82], and other anatomic locations. ECM remodeling is likely a complex process that involves multiple wound healing processes and cell types. Immune modulation, cell recruitment, and stem cell activation and proliferation are all processes that have been implicated during ECM remodeling, and it is probable that these are intricately linked [196]. PVSCs are a recently described cell source that reside in multiple vascularized tissues [217, 247, 248], and express mesenchymal stem cell markers. These cells are normally associated in a perivascular location surrounding small blood vessels, but migrate away from this niche following ECM implantation [217] where they may participate in remodeling. Though PVSC activation is correlated with myogenesis (unpublished data, submitted), their precise role has not been defined and may include direct transdifferentiation or release of paracrine factors.

Multiple studies have shown that rapid ECM degradation is a necessary event for constructive remodeling and that the prevention of degradation by chemically crosslinking ECM

scaffolds results in pro-inflammatory immune activation and fibrotic encapsulation of the device [128, 233, 249]. This observation has prompted a number of studies that have evaluated degradation products *in vitro* and *in vivo* as a potential mediator of remodeling. Native ECM degradation products have been shown to influence cell behavior such as proliferation and migration in biologic contexts such as tumor invasion and angiogenesis [243, 244]. These degradation products are a complex mixture of small, biologically active ECM fragments known as matricryptic molecules that possess activity that is not present in the parent ECM molecule. *In vitro* prepared ECM degradation products resulting from pepsin digestion have been shown to be an effective model system of the effect of ECM degradation. Pepsin digested urinary bladder ECM (UBM-ECM) has been shown to increase stem cell proliferation and migration *in vitro* [211], and to recruit multipotential stem cells in after digit amputation *in vivo* [245, 246]. Other studies have shown proliferative and differentiation effects on myogenic and neuronal stem cells *in vitro* and *in vivo* when injected in these injured tissues [174, 175, 250].

ECM degradation products represent a rich milieu of factors whose composition is dependent on the original composition of the ECM scaffold. These include cell adhesion proteins, glycosaminoglycans, and other proteoglycans that release multiple unique small ECM fragments upon degradation. Since the intact ECM scaffold composition varies by tissue, each will then result in a unique profile of degradation products. These degradation products have not yet been fully characterized, however, size distributions have been shown to vary between tissues [251]. Tissue specific ECM effects are currently being investigated based on the premise that tissue specific factors within each tissue's ECM would have preferential effects for restoration of the tissue of origin. M-ECM and C-ECM, possessing muscle specific ECM components, may preferentially influence skeletal and/or cardiac muscle tissues.

Skeletal muscle PVSC differentiation resulted in a complex phenotype with a mixture of skeletal and cardiac muscle markers. This is similar to observations of other stem cell types during development and early tissue wound healing [252]. The course of early fetal development of skeletal muscle has shown both cardiac troponin and fast skeletal muscle myosin heavy chain, which are highly cardiac and skeletal muscle specific, respectively, in adult tissues [252]. These results have extended to muscle derived stem cell (MDSC) differentiation *in vitro*, where a mix of skeletal and cardiac muscle contractile proteins is observed [252]. Both muscle and non-muscle ECM treatments increased sarcomeric MHC expression and cell fusion. SIS increased the total number of fused cells, whereas M-ECM and C-ECM increased the number of nuclei per cell. This may suggest that SIS is most effect for directing early myogenesis, whereas M-ECM and C-ECM promotes greater maturity for fusing cells.

Cardiac PVSCs, however, did not show skeletal muscle differentiation or fusion. This lower relative differentiation capacity compared to skeletal muscle PVSCs may be related to the differing regenerative capacity of skeletal and cardiac muscle. Skeletal muscle is more able to regenerate following injury than cardiac tissue, which leads to scar formation [3]. This lack of differentiation competence may be reflected in the PVSC population as well. The present study showed that ECM treatment did not alter this lack of differentiation potential.

ECM treatment did affect the proliferation of skeletal and cardiac muscle PVSCs, however. Both skeletal muscle myocytes and cardiomyocytes are considered post-mitotic, terminally differentiated cells in adult tissues. As such, differentiation and proliferation are opposing processes in that terminal differentiation requires a decrease in proliferation. Skeletal muscle regeneration is an archetype of this response, where after skeletal muscle progenitors enter a proliferation phase, exit the cell cycle, and fuse to form non proliferating myofibers [39].

It was shown that ECM degradation products, regardless of muscle or non-muscle tissue sources, inhibited proliferation in high serum culture conditions without an increase in cell death, as shown by similar total cell numbers after treatment. Serum free conditions were then investigated to determine whether factors in the ECM directly resulted in this decreased proliferation, or if it was due to inhibiting mitogenic pathways from serum stimulation. Under serum free conditions however, ECM treatment did not show a dose dependent effect upon proliferation, though C-ECM induced a reduction in proliferation in skeletal muscle PVSCs and SIS treatment induced a slight decrease for cardiac muscle PVSCs. This suggests that anti-proliferative mechanisms are present in pepsin derived ECM degradation products that neutralizes mitogens found in serum rather than directly affecting the cell cycle. Purified type I collagen showed a similar reduction in proliferation which indicates that collagen and/or collagen degradation products, rather than small matricryptic molecules cause this effect.

There are some limitations to the approach taken in the present study. Exposure to an ECM digest represents the sum of the numerous individual effects from all of the degradation products in the pepsin digest. Specific peptide sequences have been isolated from urinary bladder ECM digests, which affected stem cell migration [246]. However, this single peptide represents a minute fraction of all of the unique constituent molecules. It is possible that some of these molecules have opposing effects, such as chemotactic and chemorepellant effects. Also, pepsin is not a physiologic enzyme found during normal wound healing or homeostasis *in vivo*. Physiologic degradation involves many proteases that have far greater cleavage specificity than pepsin [243]. Nevertheless, ECM pepsin degradation products have shown activity similar activity as *in vivo* derived products, and are a useful model of ECM degradation. Finally, though specific ECM treatments increased skeletal PVSC fusion, this was still an extremely rare event

relative to primary myoblast isolates or cell lines. It is unclear whether these differences are relevant for PVSC differentiation into skeletal muscle in an *in vivo* setting.

In summary, clearly defined tissue specific effects of muscle and non-muscle ECM on PVSCs were not consistently observed *in vitro*. Rather, ECM degradation products from any source were effective at improving skeletal muscle PVSC myogenic differentiation as well as decreasing skeletal and cardiac PVSC proliferation. The default PVSC differentiation phenotype was also non-tissue specific as PVSCs typically were predisposed towards a cardiomyogenic lineage, though both skeletal and cardiac differentiation markers were found. These results suggest that direct influence of ECM degradation products on PVSC differentiation into skeletal or cardiac muscle is not a mechanism of potential tissue specific effects *in vivo*.

## **4.0 COMPARISON OF ECM SCAFFOLDS PREPARED FROM SKELETAL AND CARDIAC MUSCLE FOR TREATMENT OF VOLUMETRIC MUSCLE LOSS IN A RODENT MODEL**

### **4.1 INTRODUCTION**

Extremity volumetric muscle loss (VML) as a consequence of traumatic injury exceeds the innate regenerative capacity of skeletal muscle tissue and leads to significant functional impairment [10]. Direct or indirect causes of VML include direct trauma (e.g. car accidents and gunshot wounds), peripheral compartment syndrome, muscle ischemia, and surgical excision [13, 16, 18, 33]. VML is typically debilitating, and associated with decreased quality of life and independence [22, 23]. Current treatment strategies for VML are limited. Autologous muscle grafting (e.g. free flap transfer) is the standard of care, though this approach presents challenges such as limitations in the size of the transferred muscle tissue, engraftment efficiency, and donor site morbidity [11, 14, 31, 36]. Implantable synthetic materials have been used for muscle repair to reinforce injured muscle and prevent further damage, but the non-degradable polymers typically used for such repairs may result in adverse outcomes such as fibrous tissue deposition [134, 135, 139]. Therefore, new therapies are needed to not only reinforce damaged muscle, but to also promote new muscle formation and functional recovery.

Naturally derived extracellular matrix (ECM) scaffolds have been successfully used to promote tissue restoration in a number of pre-clinical and clinical applications [73, 74]. These biologic materials are prepared via the decellularization of mammalian tissues to yield acellular scaffolds composed of native ECM. This ECM is composed of a diverse range of collagen types, glycosaminoglycans, proteoglycans, other bioactive molecules that provide potent biological signals to its resident cells. Multiple tissues and organs have been decellularized for use as ECM scaffolds, including the heart [180, 202], pericardium [242, 253], vascular tissue [154], skeletal muscle [102, 168], liver [148, 254], lung [213, 255], small intestine [194, 256], urinary bladder [257, 258], and dermis [235, 241], among many others. The ECM scaffolds derived from these various tissues have primarily been implanted in non-homologous locations (e.g. implanting a dermal ECM scaffold in a skeletal muscle location for ventral hernia repair). Recently however, homologous tissue specific ECM applications have been investigated. Since the ECM of every tissue provides its resident cells with a unique microenvironment, characterized by a composition and architecture specific to that tissue for structural, mechanical, and biological support, it is plausible that a tissue specific ECM scaffold is to use the cues provided in the ECM microenvironment to promote site specific remodeling.

The goal of the present study was to evaluate the efficacy of a skeletal muscle tissue specific ECM scaffold to promote functional skeletal myogenesis in a mouse model of VML compared to non-skeletal muscle ECM. Skeletal muscle tissue was decellularized using a previously described method, and the identical method was applied to cardiac tissue (non-skeletal, striated muscle) and small intestinal submucosa (non-skeletal, smooth muscle).

## **4.2 METHODS**

### **4.2.1 Overview of experimental design**

The same decellularization protocol was utilized to prepare skeletal muscle ECM (M-ECM), cardiac ECM (C-ECM), and small intestinal submucosa sheets that were prepared using conventional techniques (SIS) or using the muscle ECM protocol (SIS-M). ECM sheets were further processed into a particulate form for implantation in a murine quadriceps VML model. Each ECM scaffold was used to repair the VML defect, which was evaluated histologically for evidence of skeletal muscle myogenesis and remodeling at 14, 56, and 180 days post implantation. Functional improvements were characterized at 180 days using electromyography (EMG) to determine if there is a difference in functional recovery among the groups. All experiments were conducted with approval of the University of Pittsburgh Institutional Animal Care and Use Committee (IACUC).

### **4.2.2 Tissue decellularization and device preparation**

Psoas major skeletal muscle, cardiac left ventricle free wall, and small intestine tissues were obtained from market weight pigs (approx. 100 kg) and decellularized using a modified version of a previously established protocol for skeletal muscle ECM. Skeletal and cardiac muscle were sliced into 2.2 mm cross sectional sheets (transverse to the longitudinal axis) using a rotating blade. Small intestinal submucosa sheets were prepared by isolating the stratum compactum, muscularis mucosa, and submucosal from the other layers via mechanical delamination. All tissues were then frozen and lyophilized. The dried tissue sheets were delipidized by stirring in a

chloroform/methanol solution (2:1 v/v, Sigma) for 30 minutes, followed by a graded series of ethanol (100, 100, 95, 70, and 50%) for 30 minutes each and then several water washes. Tissues were then frozen until further processing in a spinner flask at 70 RPM. Tissues were enzymatically processed with 0.2% Trypsin/0.2% EDTA (Sigma) at 37 °C for 2 hours, and then placed in alternating 20 minute hypotonic/hypertonic washes of deionized water and 2X PBS, respectively. Detergent treatment with 2% sodium deoxycholate (Sigma) for 5 hours was performed to solubilize cell components, followed by another pair of hypotonic/hypertonic washes and a fresh change of 2% sodium deoxycholate for 16 hours. A 1% Triton X-100 (pH=8, Sigma) solution was used to remove residual deoxycholate for 1 hour, which was followed by 2 washes in deionized water. Final decellularization was achieved after exposure to 0.1% peracetic acid/4% ethanol for 2 hours and residual chemicals removed via extensive washing: 2 washes with PBS and 2 washes in deionized water for 30 minutes each, 1X PBS for 16 hours, and 4 washes in deionized water. The resultant M-ECM, C-ECM, and SIS-M ECM sheets were frozen and lyophilized.

Three dimensional ECM devices were prepared from ECM sheets as previously described [56]. Lyophilized ECM sheets were comminuted into a particulate form using a Wiley Mill. ECM particulate was passed through either 40 or 60 mesh screens and combined at a 2:1 (40:60 mesh, w/w) ratio. This ECM particulate mix was wetted, fit within a 3 mm thick mold, and lyophilized. Devices were then cut to final dimensions of 4x4x3 mm to fill the VML defect. ECM devices and sheets were sterilized with ethylene oxide (16 h cycle at 50 °C in a Series 3plus EOGas Sterilizer, Anderson Sterilizers, Inc. Haw River, NC) prior to implantation.

### **4.2.3 Surgical creation of the VML defect and ECM device implantation**

A VML defect was created in the quadriceps of female C57BL/6 mice (age 6 - 8 weeks, Jackson Laboratories) as previously described [56] and shown in Figure 29. Mice were anesthetized with 2% isoflurane and a 1.5 cm incision through the skin and fascia was made to expose the quadriceps muscle. The VML defect was created by full thickness excision of the tensor fasciae latae muscle and partial thickness excision of the underlying rectus femoris (Figure 29), which corresponds to the following defect dimensions: full muscle width x 4 mm (longitudinal) x 3 mm deep. Non-resorbable polypropylene sutures (size 7-0, Oasis, Fisher Scientific) were placed along the lower corners of the defect to demarcate defect borders. Defects were either left untreated (NTx) or repaired with M-ECM, C-ECM, SIS-M, or SIS particulate devices. The three dimensional ECM devices were placed within the VML defect and covered with a 1 x 1 cm ECM sheet sutured with polypropylene sutures to adjacent healthy muscle (Figure 30). The incision was closed with polyglycolic acid (PGA) suture (size 7-0, Oasis, Fisher Scientific), and animals were allowed to ambulate normally with analgesic (buprenorphine hydrochloride, 0.25 mg/kg) and antibiotic (enrofloxacin, 20 mg) administration for 3 days post operatively. Animals were sacrificed and the treated quadriceps muscle harvested for histologic analysis after 14, 56, and 180 days post implantation (n = 4 per device and time point), or for functional electromyography (EMG) analysis at 180 days (n = 8 per device).

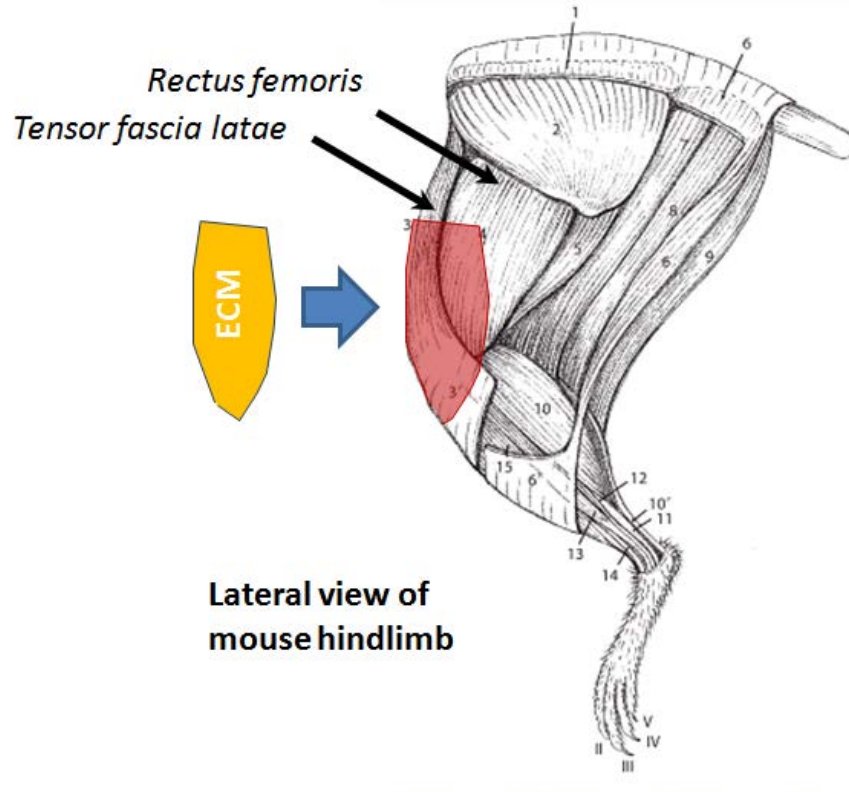


**Figure 29.** Schematic representation of the VML model in the mouse quadriceps muscle<sup>2</sup>. The defect (red region) consists of a full thickness resection in the *tensor fascia latae* muscle and a partial thickness resection of the *rectus femoris* in the mouse hindlimb. A size matched ECM particulate device is then implanted within the defect.

<sup>2</sup>Adapted from *The Laboratory Mouse*, first edition, Vladimír Komárek, Gross Anatomy, page 122, Copyright 2004, with permission from Elsevier. <https://www.elsevier.com/>

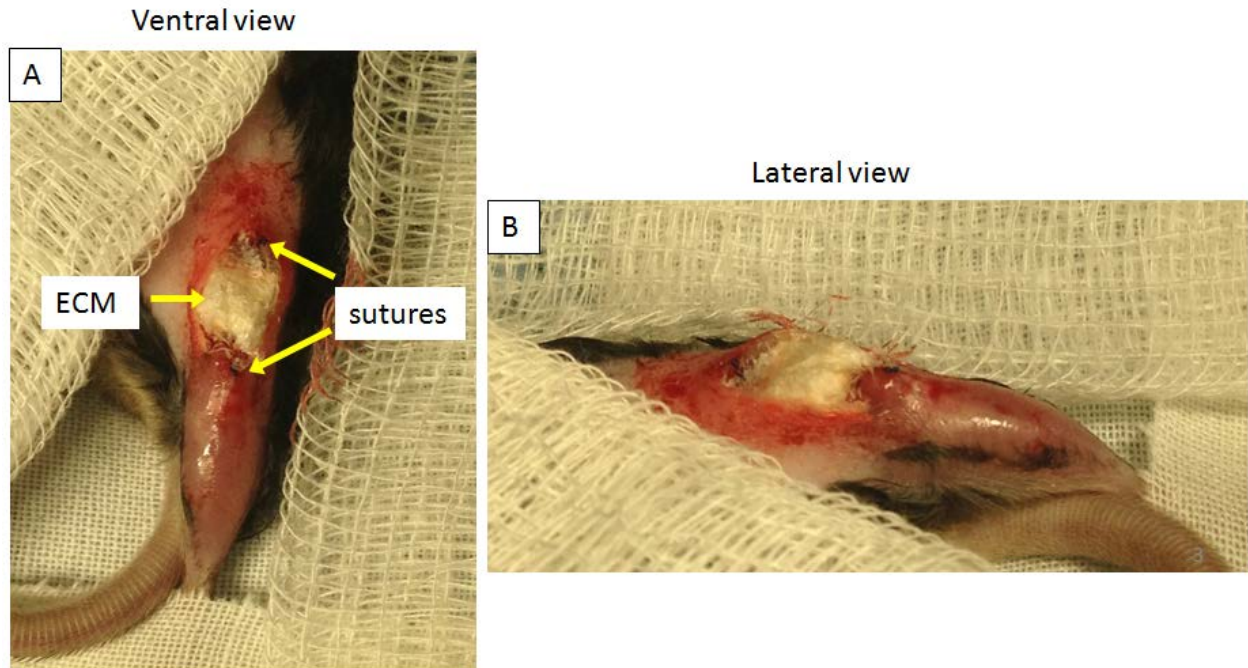


**Figure 30.** Representative images of an SIS particulate device with overlaid sheet within the VML defect at the time of implantation. The ECM fills the defect and is held in place with a sheet of ECM sutured at the distal and proximal defect borders.

#### 4.2.4 Histologic analysis of ECM remodeling in a VML defect

Histologic analysis was conducted on tissues collected at 14, 56, and 180 days post implantation to evaluate ECM remodeling and myogenesis. Mouse legs were fixed with 10% neutral buffered formalin immediately following sacrifice, and the entire quadriceps muscle isolated, bisected along the saggital plane, and sectioned. Fixed tissues were embedded in paraffin and cut into 5  $\mu\text{m}$  thick sections for Masson's Trichrome staining or immunolabeling. Defect borders were demarcated by the non-resorbable sutures at the edges of the defect.

Immunolabeling studies were performed to determine the presence of blood vessels (CD31), innervation ( $\beta$ III tubulin), and myogenesis (fast and slow myosin heavy chain and

desmin) within the defect area. Sections were deparaffinized with xylenes and a graded series of ethanol prior to immunolabeling and extensive buffer washes conducted between each step unless otherwise indicated.

1. CD31 and  $\beta$ III tubulin immunolabeling was performed to evaluate the tissue remodeling characteristics of angiogenesis and innervation, respectively. Antigen retrieval was conducted in sodium citrate (10 mM, Sigma) heated to 95-100 °C for 20 minutes and sections were blocked for 1 hour with 1 % bovine serum albumin (BSA, Sigma)/2% horse serum (Gibco) in PBS-T (0.1% Triton X-100/0.1% Tween 20, Sigma). Sections were decanted and immediately incubated overnight at 4°C in either CD31 (rabbit polyclonal, ab28364, abcam) or  $\beta$ III tubulin (mouse monoclonal, clone TU-20, MA1-19187, Sigma) primary antibodies diluted (1:100) in the blocking solution. AlexaFluor 488 conjugated secondary antibody (anti-rabbit or anti-mouse Alexa Fluor-488, Invitrogen) was applied for 2 hours followed by 4',6-diamidino-2-phenylindole (DAPI) nuclear staining. Slides were coverslipped with aqueous mounting media (DAKO) and imaged via epifluorescence to determine the presence of blood vessels and nerves around and within the ECM device during remodeling.

2. Fast and slow myosin heavy chain (f/s-MHC) co-labeling was performed to determine the presence of mature skeletal muscle as previously described [105]. Antigen retrieval was conducted with 0.1 mM EDTA heated to 95-100°C for 25 minutes followed by 0.1% Trypsin/0.1% Calcium Chloride (w/v) at 37 C for 10 min. Peroxidase activity and non-specific protein binding were blocked by incubation in 0.3% (v/v) hydrogen peroxide for 10 minutes and 1% BSA/2% horse serum in TBS (blocking solution) for 30 minutes, respectively. Blocking solution was decanted and then immediately incubated with slow MHC primary antibody (mouse monoclonal, clone NOQ7.5.4D, M8421, Sigma) diluted in blocking solution (1:4000) for 40

minutes. A biotinylated secondary antibody (anti-mouse biotinylated, Vector) diluted in blocking solution (1:200) was applied for 1 hour followed by incubation with an avidin-biotin-peroxidase complex (Vectastain ABC, Vector) for 30 minutes. A diaminobenzadine substrate (ImmPact DAB, Vector) was applied until appropriate staining developed. Sections were incubated in blocking solution for an additional 10 minutes and labeled with an alkaline phosphatase conjugated primary antibody against fast myosin heavy chain (anti-mouse monoclonal alkaline phosphatase conjugated, clone MY-32, A4335, Sigma) diluted in blocking solution (1:200) for one hour. Red alkaline phosphatase substrate was applied until appropriate staining developed. Slides were counterstained with hematoxylin, dehydrated, and coverslipped.

3. Desmin labeling for developing muscle and mature muscle was achieved using the same protocol for slow MHC as described above in (2), substituting a desmin primary antibody (mouse monoclonal, clone DE-U-10, ab6322, Abcam) diluted (1:500) in blocking solution.

#### **4.2.5 Electromyography (EMG) of innervated muscle in the VML defect**

Electromyography (EMG) measurements were conducted at 180 days to assess functionally innervated skeletal muscle formation within the VML defect following ECM remodeling (n = 8 animals). Muscle electrical activity was recorded with a bipolar silicone epimysial electrode inserted within the VML defect along the fascial plane dividing the tensor fascia latae and underlying rectus femoris muscle. The recording area of the electrode was in contact with the ventral aspect of the defect and was insulated from underlying uninjured muscle by the silicone sheet. A pair of 38G Teflon coated fine wire electrodes with deinsulated tips were placed around the femoral nerve approximately 1 cm proximal to the defect to stimulate compound muscle action potentials in the quadriceps muscle. Stimulation pulses (200  $\mu$ s anodic phase, 3Hz, 20 s

train duration, Model S88X Stimulator, Grass Technologies, Natus Neurology Inc., West Warwick, RI) were applied and the resulting compound muscle action potential (CMAP) within the defect were averaged and recorded (Tektronix TDS 3012C Digital Phosphor Oscilloscope, Tektronix Inc., Aliquippa, PA) after amplification and bandpass filtering (50X gain, 30-3000Hz bandpass filter, BMA 400 bioamplifier, CWE Inc., Ardmore, PA). A schematic of the recording equipment and electrode placement is shown in Figure 31.

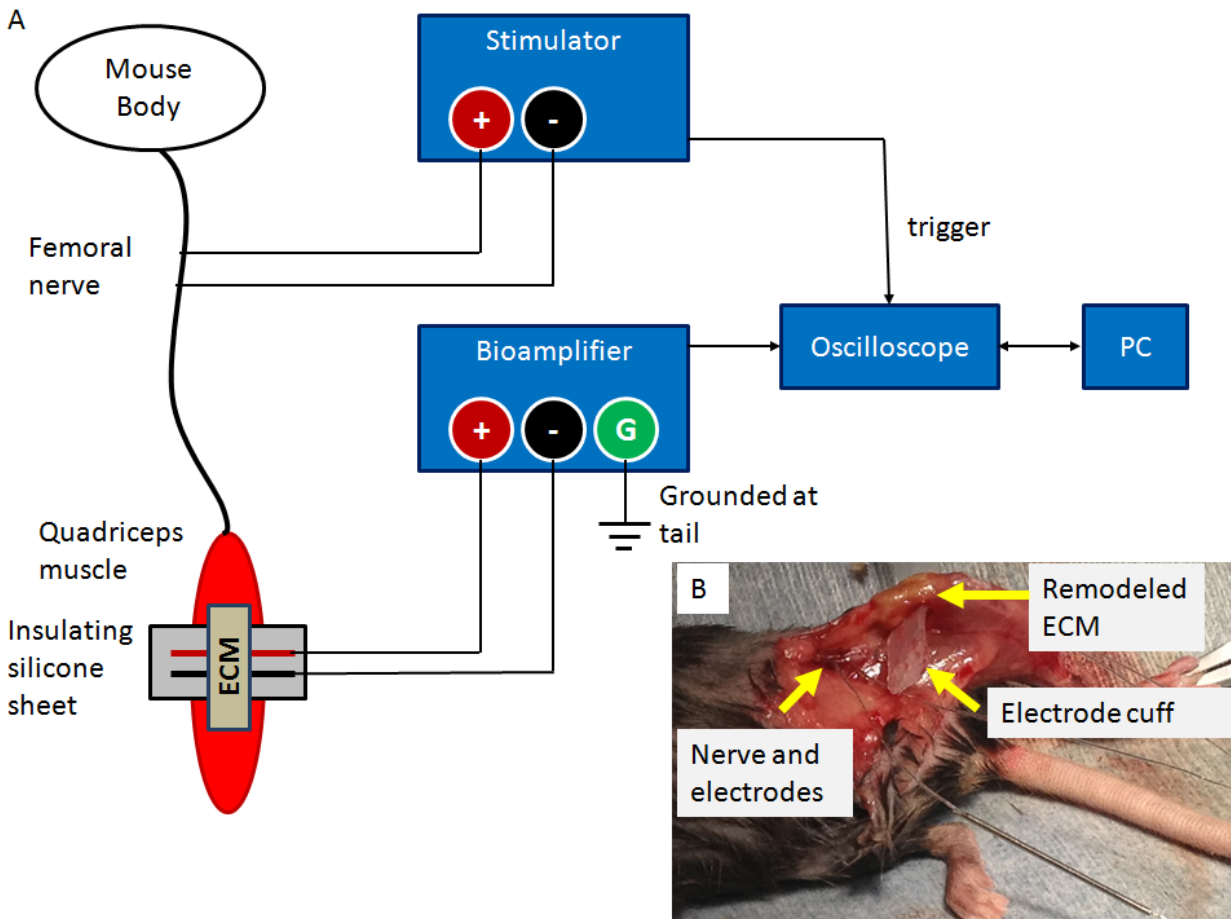


**Figure 31.** EMG recording setup for evaluating muscle function after 180 days. A schematic (A) of the recording equipment and electrode placement within the quadriceps muscle and a representative image of the electrode placement *in situ* during testing.

The CMAP was characterized by the peak-to-peak voltage ( $V_{PP}$ ) and root mean square voltage ( $V_{RMS}$ ) of the response during a time window 1-8 ms following stimulation. Muscle fiber recruitment characteristics were determined from the relationship between nerve stimulation intensity (0.3-8V) and the CMAP response ( $V_{PP}$  and  $V_{RMS}$ ) [259, 260]. These parameters include: (1) the maximum peak-to-peak voltage ( $V_{PP-max}$ ), (2) the maximum RMS voltage ( $V_{RMS-max}$ ), (3) the stimulation threshold for a CMAP reponse ( $S_{thresh}$ ), (4) the stimulation required to evoke half the maximal response ( $S_{1/2}$ ), (5) the minimum stimulation required to evoke a maximal CMAP reponse ( $S_{max}$ ), (6) and the slope of the linear region of the muscle recruitment curve (slope). These parameters correspond to a sigmoidal recruitment curve as shown in Figure 32.

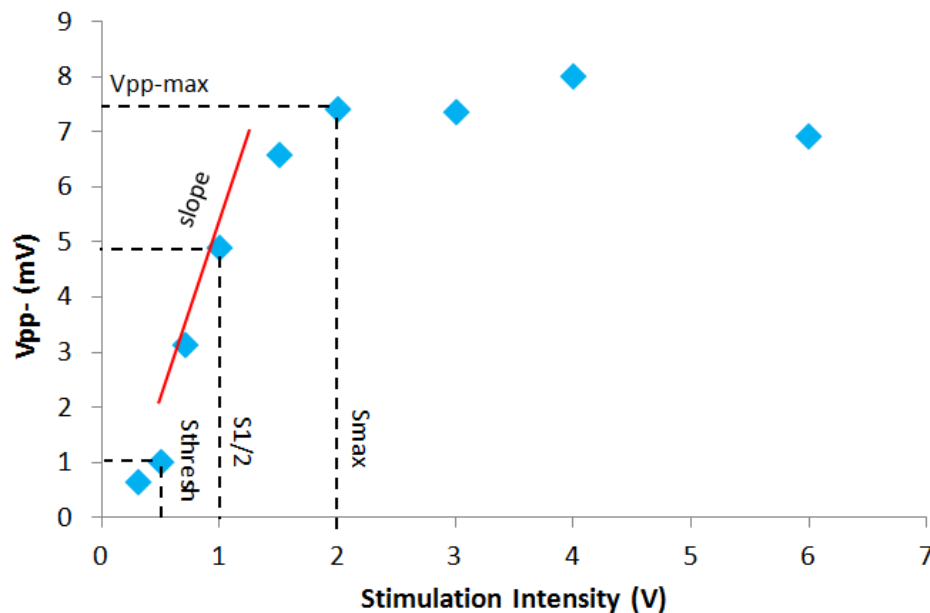


**Figure 32.** Representative muscle recruitment curve for uninjured muscle highlighting the recruitment parameters evaluated in this study. The thresholds of stimulation were calculated at

the minimum, half maximal, and maximal  $V_{pp}$  amplitude of the CMAP response. Muscle recruitment rate was calculated as the slope of linear region of the recruitment curve.

#### **4.2.6 Statistical analysis**

All values are presented as mean  $\pm$  standard error. Statistical analysis of  $V_{PP-max}$ ,  $V_{RMS-max}$ ,  $S_{thresh}$ ,  $S_{1/2}$ ,  $S_{max}$ , and slope was conducted with a Kruskal-Wallis non-parametric analysis of variance (ANOVA) with a post-hoc Mann-Whitney U Test and Sidak correction using SPSS software (IBM SPSS Statistics v21, IBM Inc., Armonk, NY). A non-parametric analysis was chosen after determining that the data did not follow a normal distribution via the Kolmogorov-Smirnov test for normality. Statistical significance was defined as  $p < 0.05$ .

### **4.3 RESULTS**

#### **4.3.1 Histologic analysis of ECM remodeling in a VML defect**

Histologic analysis of the remodeling ECM constructs implanted within the VML defect showed distinct remodeling differences between groups. Masson's Trichrome staining showed a robust mononuclear cell infiltrate in the periphery after 14 days for each ECM group, which was accompanied with disruption of scaffold architecture that is consistent with degradation. The scaffold interior was less populated with cells, with more infiltration observed for the M-ECM group. The untreated defect was also highly cellular at the defect border. A similar trend was observed at the 56 day time point, in which active mononuclear cell remodeling was underway at

the periphery. Untreated defects, however, had a greatly reduced cellular infiltrate, replaced primarily with adipose and loose connective tissue (Figure 33). After 180 days, additional histologic differences were observed. M-ECM had undergone the greatest amount of scaffold degradation, with only fragments visible after 180 days (Figure 34). The C-ECM and SIS-M groups still had bulk ECM scaffold visible within the defect, which were well cellularized at the periphery but not the interior of the scaffold. Untreated defects were similar in appearance to the 56 day time point maintaining connective tissue near the edge of native muscle and adipose tissue filling the remainder of the defect.

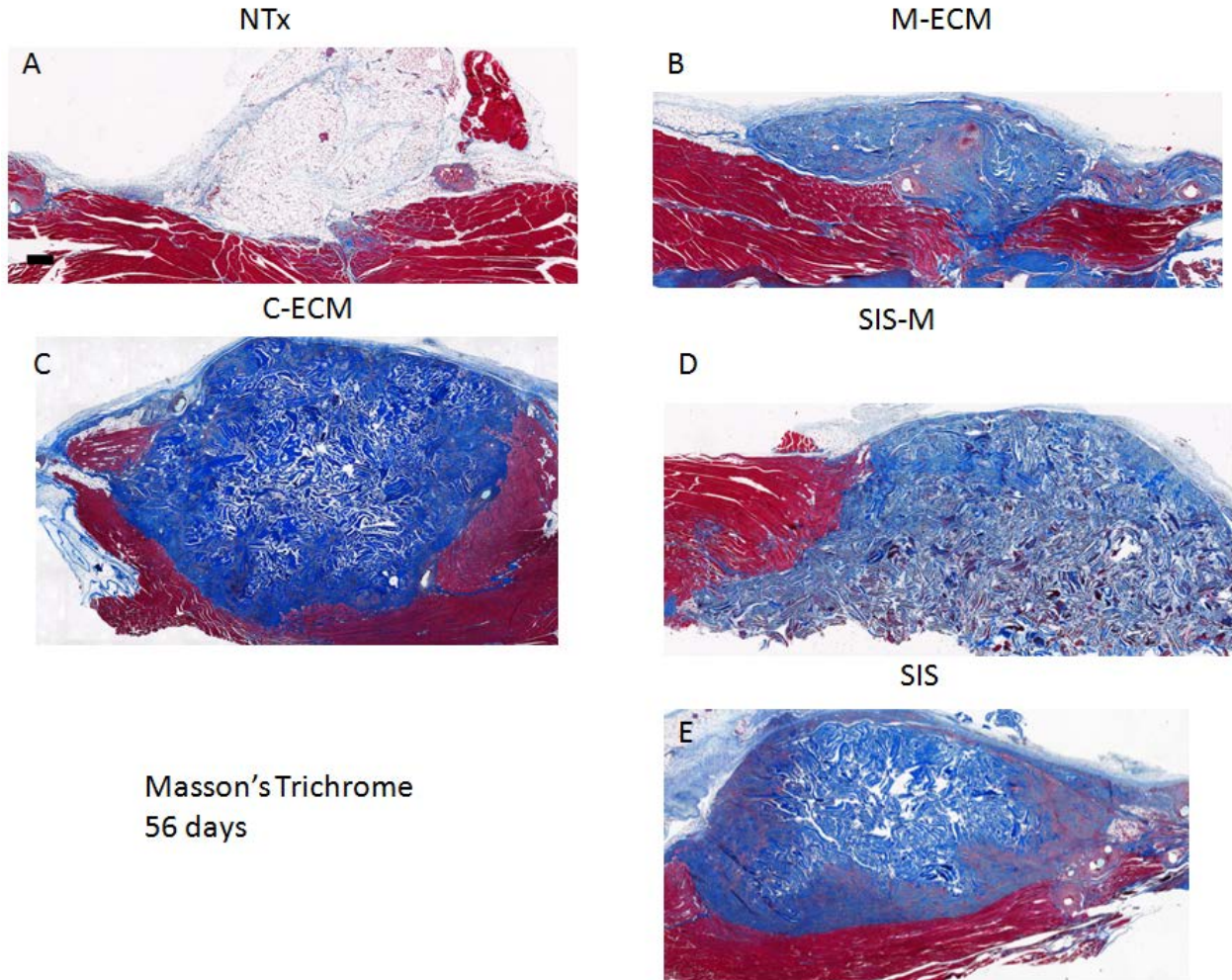


**Figure 33.** Masson's Trichrome stained images of the VML defect after 56 days. Untreated defects (A) were filled with adipose tissue (white tissue) while the ECM devices (B-E, blue) were still visible and undergoing the remodeling process. All images are oriented such that underlying uninjured quadriceps are along the bottom of each image. Scale bar represents 200  $\mu\text{m}$ .

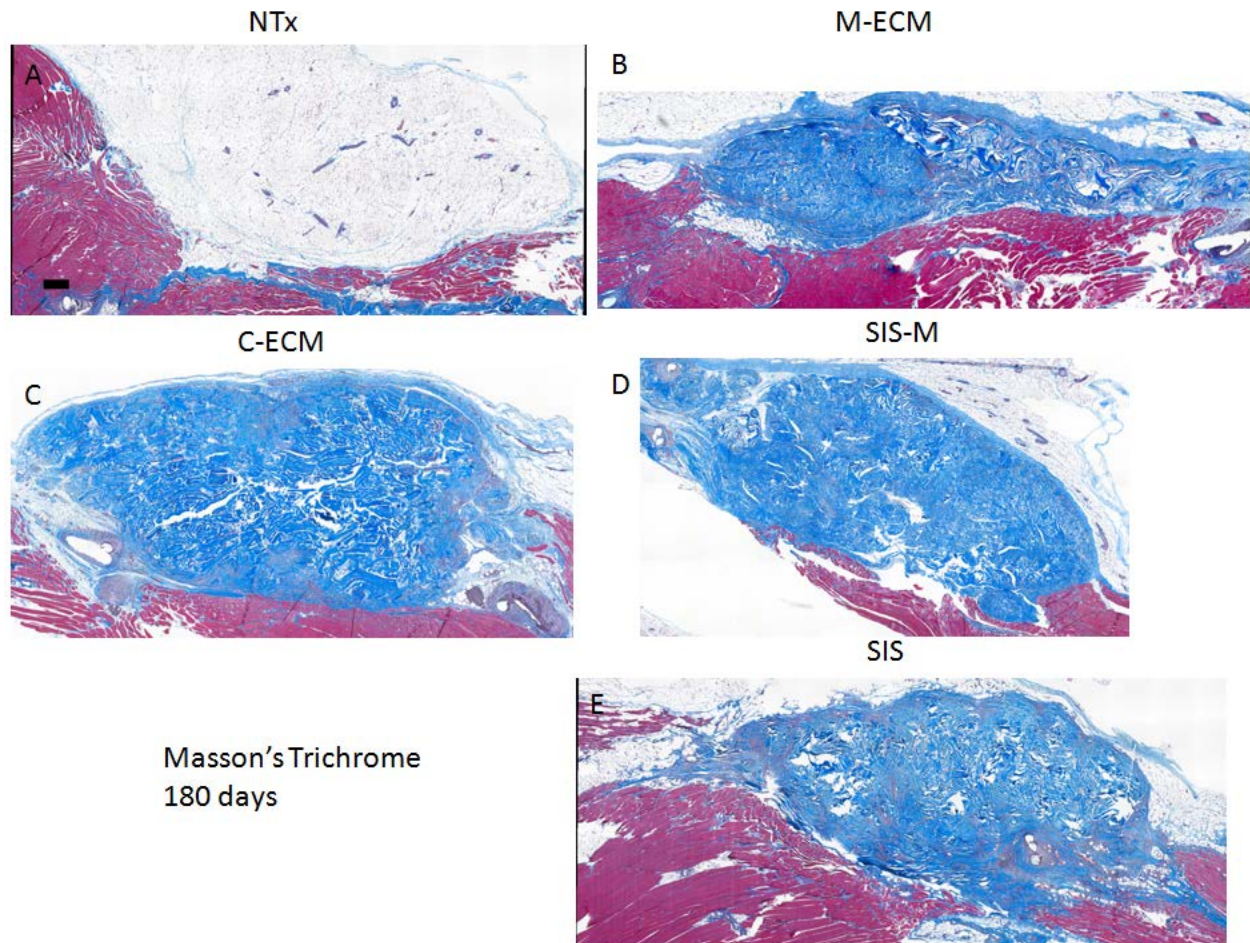


**Figure 34.** Masson's Trichrome stained images of the VML defect after 180 days. Untreated defects (A) were filled with adipose tissue (white tissue) while the ECM devices (B-E, blue) were still visible and undergoing the remodeling process. All images are oriented such that underlying uninjured quadriceps are along the bottom of each image. Scale bar represents 200  $\mu\text{m}$ .

Myogenesis within the defect was observed at a low frequency by the 56 day time point. Untreated defects showed few desmin (Figure 35) and myosin heavy chain positive myofibers (Figure 36), and these occasional cells were present only directly adjacent to well developed muscle at the defect border. Muscle cells were also infrequent in ECM treated defects, though

these cells were located farther from the defect border. A high proportion of more mature muscle at the defect border had centrally located nuclei indicating that these muscle fibers had undergone myogenesis.

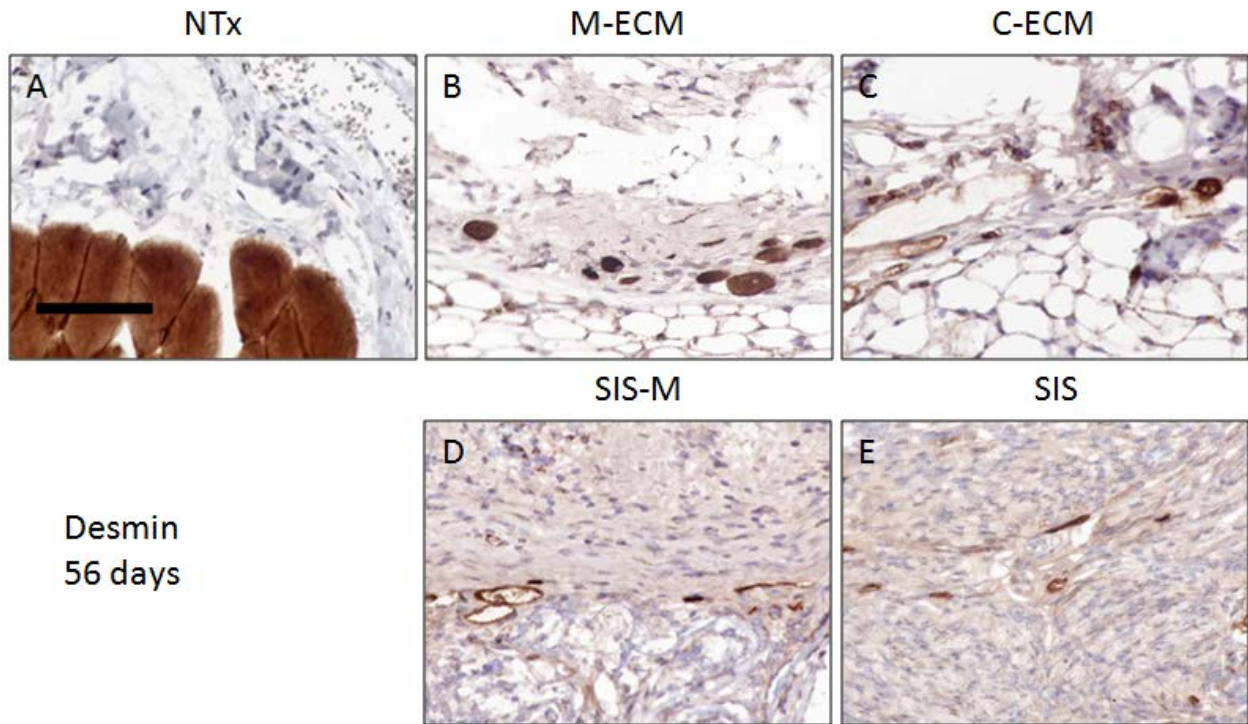


**Figure 35.** Desmin immunolabeling (brown) within the VML defect after 56 days. Desmin expressing cells did not migrate from the defect border in untreated animals (A, positive staining represents native tissue), while ECM treatment encouraged desmin positive cell accumulation in the area of remodeling near the ECM periphery (B-E). Each ECM image is located several fields of view away from the defect border, while the untreated image is located in proximity to the border to show that there are no desmin expressing cells migrating from native muscle. Scale bar represents 100  $\mu\text{m}$ .

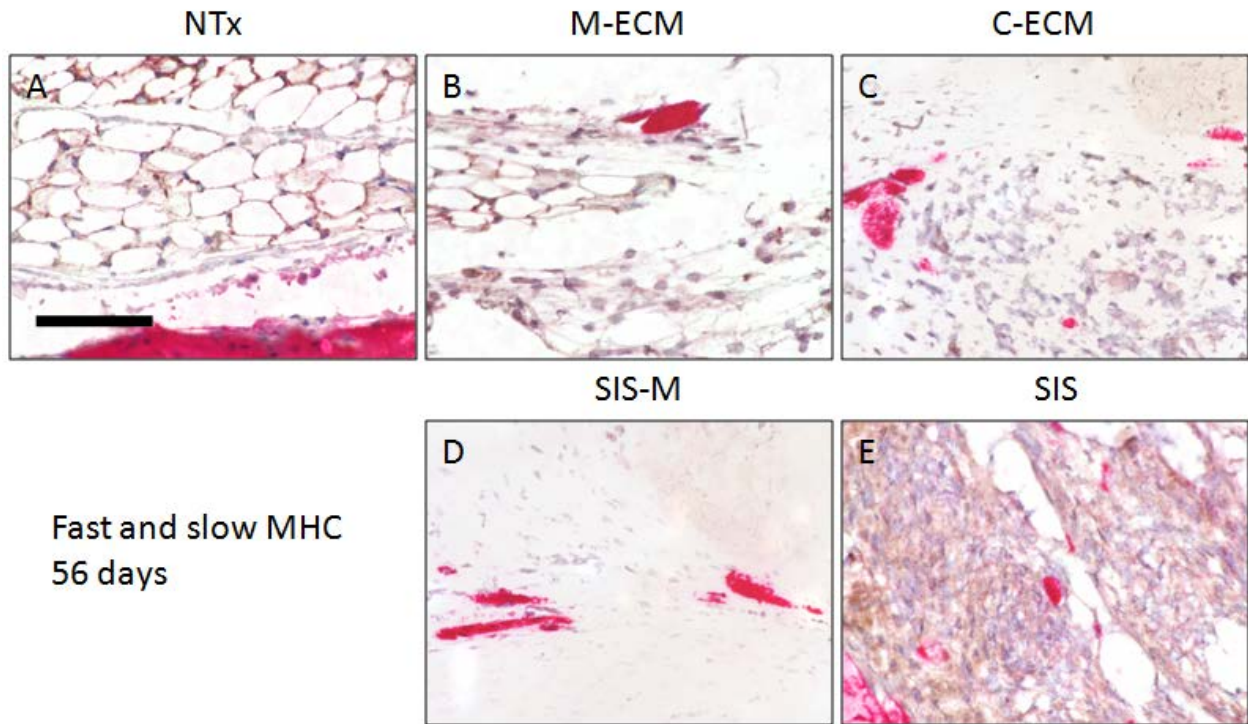


**Figure 36.** Fast (pink) and slow (brown) skeletal muscle MHC immunolabeling within the VML defect after 56 days. MHC expressing cells did not migrate from the defect border in untreated animals (A, positive staining represents native tissue), while ECM treatment encouraged desmin positive cell accumulation in the area of remodeling near the ECM periphery (B-E). Each ECM image is located several fields of view away from the defect border, while the untreated image is located in proximity to the border to show that there are no myosin expressing cells migrating from native muscle. Scale bar represents 100  $\mu\text{m}$ .

Immunolabeling studies showed the presence of CD31 expressing blood vessels within the area of tissue remodeling at both the 14 and 56 day time points (Figure 37). These cells were apparent within the peripheral regions of the scaffold, where the cellular infiltration was greatest. This was also true for the 56 day time point, though there were fewer blood vessels apparent in untreated defects. ECM associated vessels were smaller in size and more numerous at the 14 day

time point, with fewer and larger vessels at 56 days, which was typical of the ECM response.  $\beta$ III tubulin expression was observed in remodeling defects after 180 days post implantation. Small nerve bundles were found along of the periphery of implanted ECM devices (Figure 37) that was similar for each ECM treatment. There were also non-neuronal mononuclear cells expressing  $\beta$ III tubulin occasionally found within the remodeling ECM scaffolds (Figure 38).

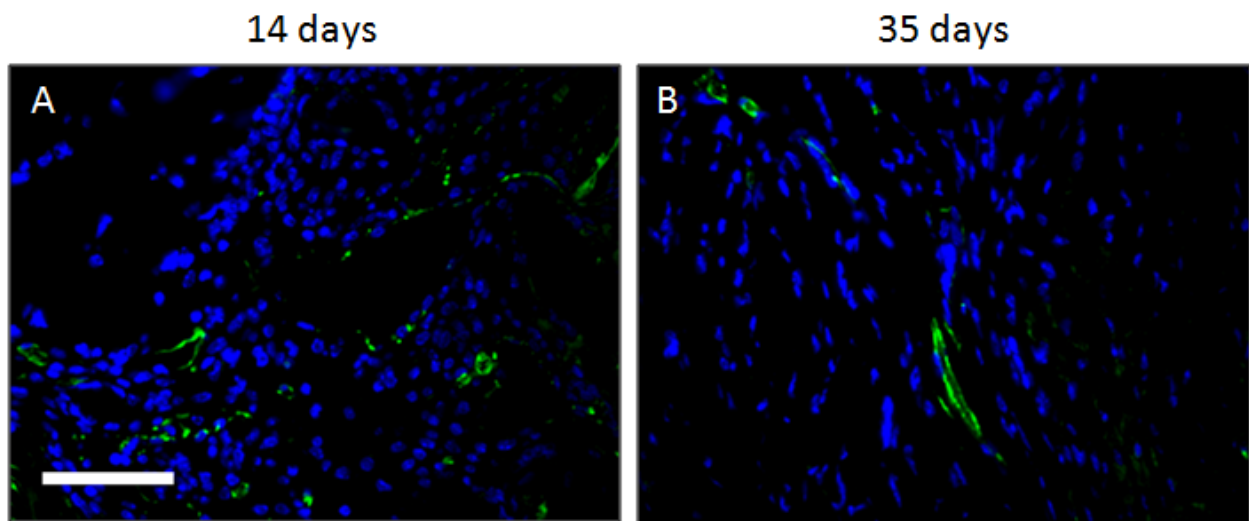


**Figure 37.** CD31 expression of blood vessels within the remodeling defect after 14 (A), and 35 days post ECM implantation. These images are representative of all ECM scaffolds. Scale bar represents 100  $\mu$ m.

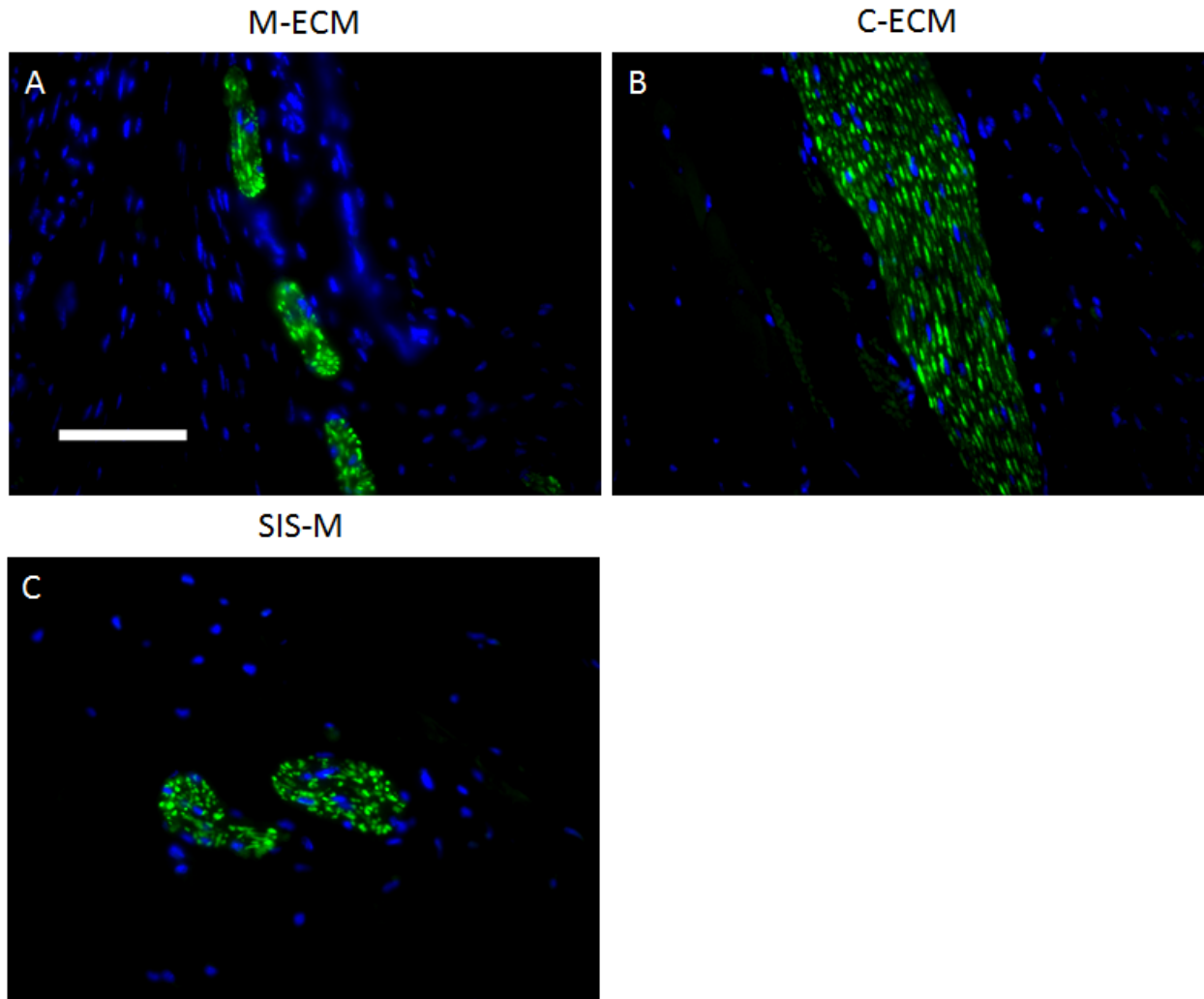


**Figure 38.**  $\beta$ III tubulin staining (green) of nerve fibers within the area of ECM remodeling. Innervation was observed following each ECM treatment including M-ECM (A), C-ECM (B), and SIS-M (C). Both transverse (A,C) and longitudinal nerve sections (B) were observed. Cell nuclei are labeled with DAPI (blue). Scale bar represents 100  $\mu$ m.

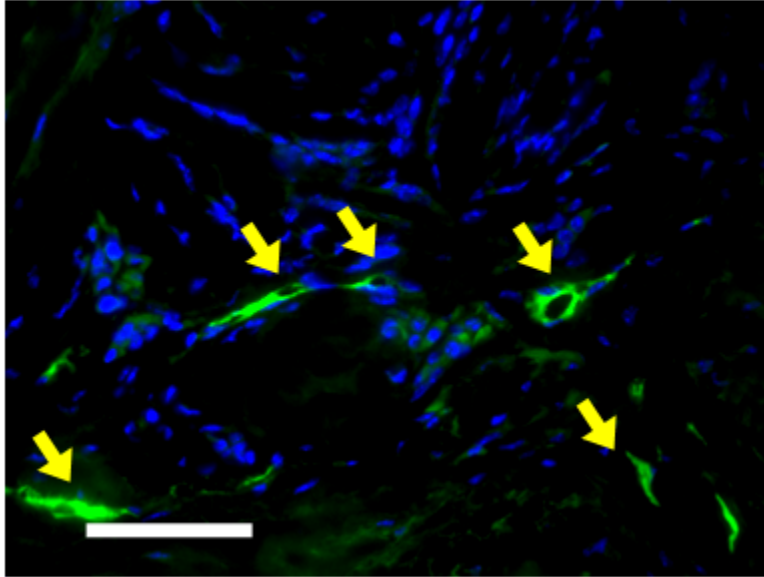


**Figure 39.** Representative image of non-neuronal  $\beta$ III tubulin expression (green, arrows) in mononuclear cells within the ECM scaffold. Cell nuclei are labeled with DAPI (blue). Scale bar represents 100  $\mu$ m.

#### 4.3.2 Electromyography (EMG) of innervated muscle in the VML defect

Electromyography (EMG) of the compound muscle action potential (CMAP) was performed to generate muscle recruitment profiles after 180 days post operatively to quantitatively assess functionally innervated skeletal muscle in the defect area. Supramaximal nerve stimulation produced  $V_{pp-max}$  and  $V_{RMS-max}$  values that were greatest in uninjured tissues ( $9.14 \pm 1.02$  mV and  $1.88 \pm 0.22$  mV) and were significantly reduced in untreated defects ( $2.71 \pm 0.63$  mV and  $0.88 \pm 0.14$  mV), corresponding to approximately 30% and 47% of the uninjured  $V_{pp-max}$  and  $V_{RMS-max}$ , respectively for untreated defects (Figure 39). The greater reduction in peak to peak voltage compared to RMS voltage indicates loss of nerve stimulation synchrony in the defect and a

broader EMG signal. ECM treatment resulted in supramaximal CMAP amplitudes that were increased relative to untreated animals. In order of greatest to least  $V_{pp-max}$  and  $V_{RMS-max}$  values: M-ECM ( $6.38 \pm 1.24$  mV and  $1.65 \pm 0.30$  mV), SIS ( $5.62 \pm 0.97$  and  $1.36 \pm 0.22$  mV), C-ECM ( $4.38 \pm 0.75$  and  $1.11 \pm 0.15$  mV), and SIS-M ( $3.57 \pm 0.46$  and  $1.09 \pm 0.10$  mV). Though each ECM treatment increased  $V_{PP-max}$  and  $V_{RMS-max}$  compared to untreated defects, differences between ECM scaffolds were not statistically significant from each other (Figure 40A).

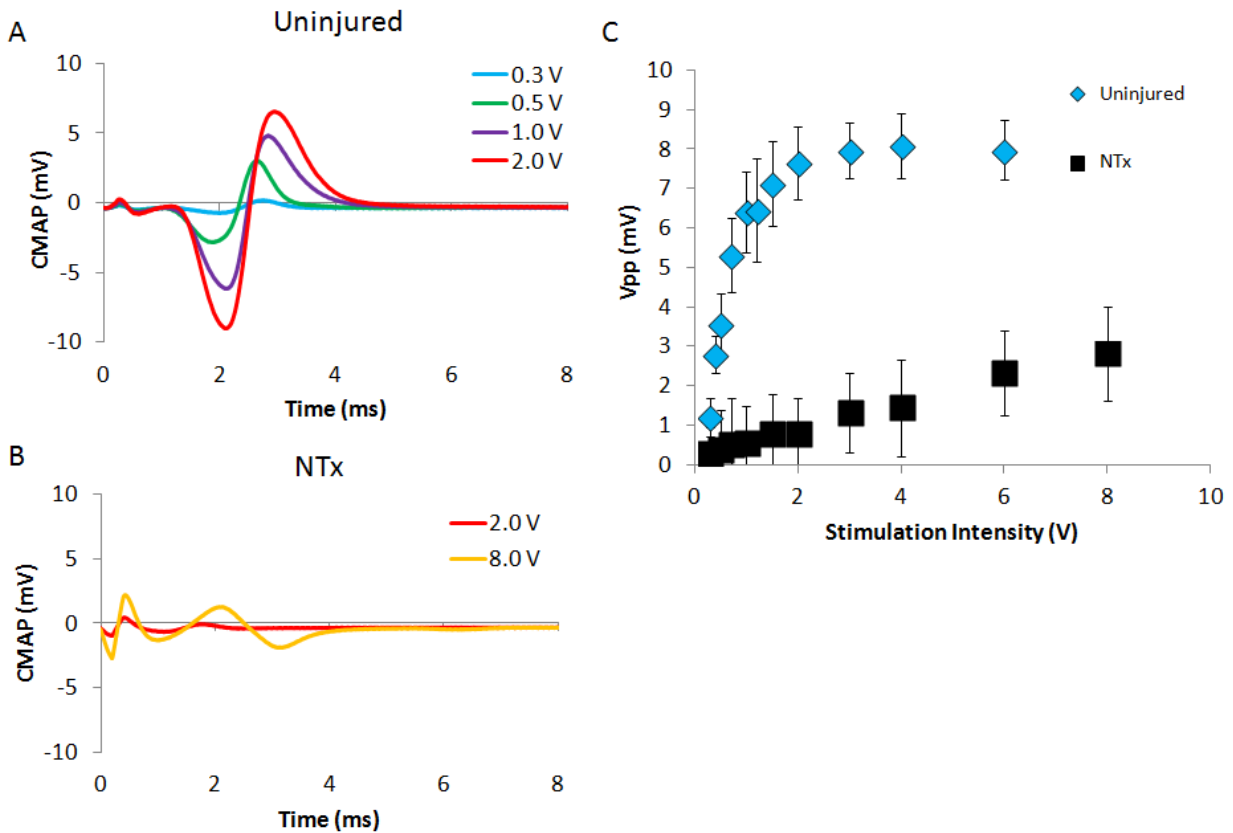


**Figure 40.** Representative waveforms of the CMAP response (A-B) at increasing nerve stimulation intensities (0.3-2.0 V for uninjured and 2.0-8.0V for untreated) and the averaged recruitment curves for uninjured and untreated VML defects after 180 days. The amplitude of the

CMAP waveform at each stimulation intensity was used to generate muscle recruitment curves. The initial biphasic wave before 1 ms represents stimulation artifact.

The untreated VML defect caused a deficiency in muscle recruitment rate as shown in the slope of the recruitment curve. Uninjured animals had a recruitment slope of  $8.84 \pm 2.53$  mv/V compared to the reduced slope of  $0.54 \pm 0.15$  mV/V for untreated animals. ECM treatment resulted in increased recruitment slopes (in order of greatest to least): M-ECM ( $6.53 \pm 2.10$  mV/V), SIS ( $3.96 \pm 1.2$  mV/V), C-ECM ( $2.10 \pm 0.75$  mV/V), and SIS-M ( $1.27 \pm 0.46$  mV/V), though only SIS response was statistically increased compared to the untreated control (Figure 40B). The nerve stimulation thresholds necessary to evoke a minimum, half maximal, and maximal responses were also affected by generation of a defect, which was partially recovered in ECM treated animals. The generation of a VML defect increased the stimulation voltage required to elicit a detectable response with  $S_{\text{thresh}}$  of  $0.41 \pm 0.03$  V in healthy animals increased to  $4.94 \pm 0.77$  V for injured untreated animals. ECM treatment reduced  $S_{\text{thresh}}$  to a similar extent for all ECM treatment groups, which ranged between 1.36 and 1.6 V.  $S_{1/2}$  and  $S_{\text{max}}$  were also increased relative to healthy animals, though generally, was not significantly affect by any ECM treatment (with the exception of  $S_{1/2}$  for C-ECM. Figure 40C).

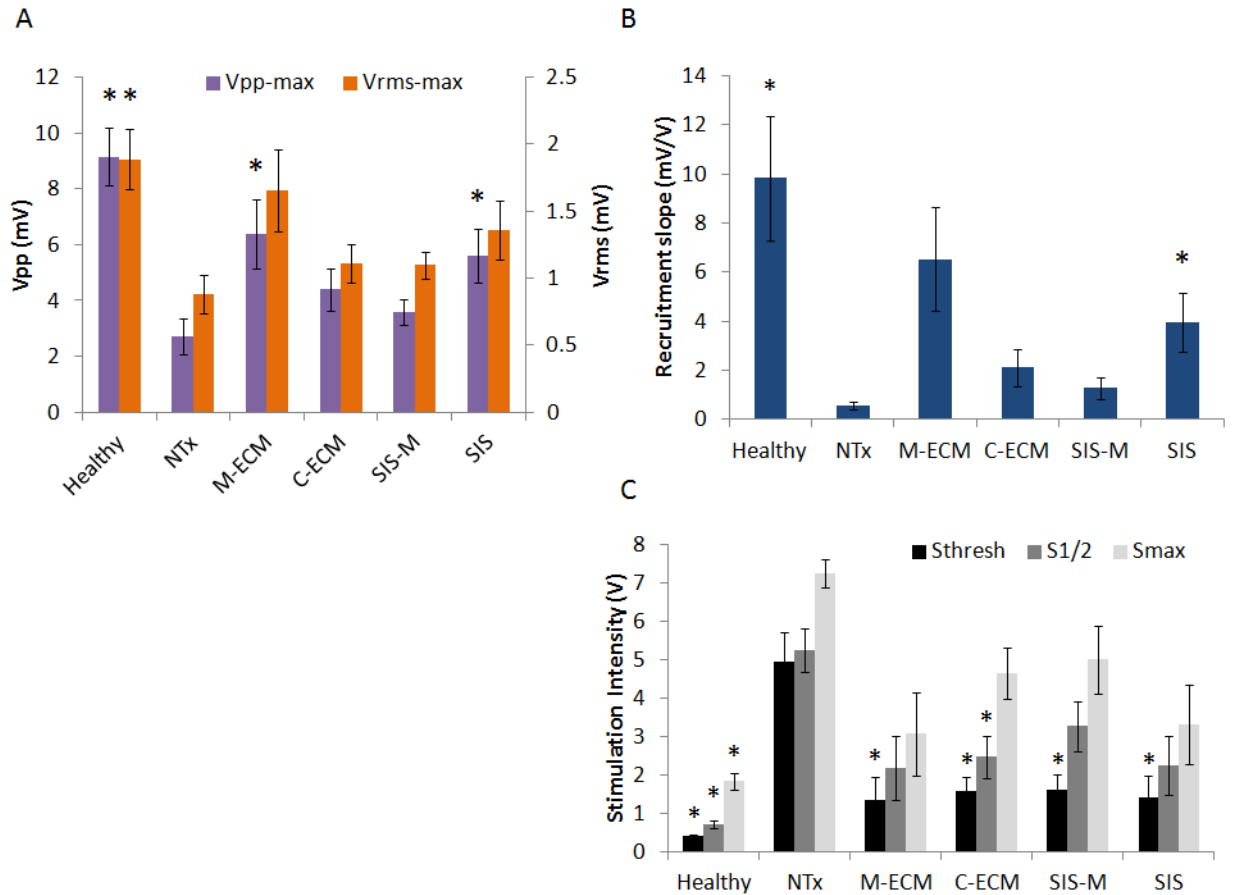


**Figure 41.** Muscle fiber recruitment parameters from EMG recordings of the CMAP within the VML defect after 180 days. The amplitude of the CMAP response (A) was calculated as the peak-to-peak voltage ( $V_{PP}$ ) and root mean square voltage ( $V_{RMS}$ ). Muscle recruitment rate was defined as the slope of muscle recruitment during the linear region of the recruitment curve (B). Stimulation efficacy (C) was evaluated as the minimum nerve stimulation intensity required to evoke a minimum threshold, half maximal, and maximal amplitude response from the recruitment curve. Statistically significant differences from untreated animals as determined by Kruskal-Wallis non-parametric analysis of variance (ANOVA) with a post-hoc Mann-Whitney U Test and Sidak correction ( $p < 0.05$ ) are denoted with (\*). No significant differences were found between ECM treatment groups or healthy animals.

## 4.4 DISCUSSION

The present study compared tissue specific ECM scaffolds prepared from skeletal and cardiac muscle to non-muscle small intestine derived ECM in their capacity promote functional restoration in a murine VML injury model. ECM particulate devices were implanted in surgically created VML defects for evaluation over a time course of 14, 56, and 180 days post implantation. ECM remodeling was characterized histologically at each time point, and muscle function was evaluated using EMG after 180 days.

ECM scaffolds are a clinically utilized biomaterial in numerous tissue reconstruction applications [74]. The widespread use of these scaffolds is due to the favorable remodeling response following implantation in sites of injury, where they are rapidly degraded and replaced with site specific host tissue [73, 207]. Though ECM scaffolds may be isolated from virtually any tissue, it is unknown how the source tissue affects the remodeling response. The tissue specific ECM scaffold hypothesis postulates that an ECM scaffold isolated from the same tissue it is intended to treat will lead to the optimal remodeling response because it contains the ideal microenvironmental factors for that tissue. Tissue specific ECM properties have been characterized and compared across many decellularized tissues, and in vivo applications of tissue specific scaffolds have shown promise in treating injured organs such as the heart [123, 192, 203], lung [88], and liver [85] using heart, lung, and liver ECM, respectively. This success has prompted studies characterizing and comparing homologous vs. non-homologous ECM scaffold implementation in vivo and in vitro, but an often overlooked variable is the effect of the decellularization methods used to isolate the ECM. Adequate decellularization is necessary to avoid an adverse immune response [129, 261], and so decellularization standards have been established to ensure that excess cellular material has been removed from the tissue [74].

However, every decellularization treatment inevitably affects ECM structure and/or composition, and this phenomenon has been previously shown for multiple ECM scaffolds [181, 241]. Removal of ECM sequestered growth factors and partial protein denaturation are common sequelae of decellularization methods that involve strong ionic detergents, enzymes, or organic solvents, which are necessary to fully decellularize certain tissues [241]. Distinctive tissue characteristics, such as diffusion and mechanical properties, often necessitate tissue specific decellularization strategies. This creates difficulties in directly comparing ECM derived from different tissues because the ECM scaffold is a product of both the decellularization method as well as its source tissue.

Several previous studies have investigated M-ECM for use as a tissue specific scaffold for muscle repair. The results of these studies have been mixed, and a clear advantage for an M-ECM scaffold over non-muscle scaffolds for in vivo VML repair has not yet been established [176-178]. The outcome of several series of studies has shown minimal myogenesis after acellular M-ECM implantation for muscle repair. However, myogenic potential and functional improvements were realized for these scaffolds when seeded and cultured with stem cells prior to implantation [92, 93, 101]. These prior studies have either not compared M-ECM to non-muscle ECM, or have not controlled for the effect of the decellularization method by using the same muscle decellularization method on the non-muscle tissue. The present study is the first comparison of a non-muscle (small intestinal derived ECM) that is decellularized using the same method as M-ECM such that the only difference between the scaffolds is the source tissue.

This is also the first report that extends the tissue specific hypothesis to cardiac tissue. Though both skeletal and cardiac muscle are striated muscle tissues, they have very different injury responses. Skeletal muscle has a well characterized, highly regenerative response to

injury. It is only when the injury is of a relatively large critical size, such as in VML, that these natural regeneration mechanisms are unable to compensate [10, 56, 177]. This high capacity to recover after injury is in large part due to the abundant resident stem cell population, the satellite cell, and its robust capacity to proliferate and differentiate into de novo muscle fibers. Cardiac tissue in contrast does not possess a similar resident stem cell or regenerative capacity, and its injury response is characterized by fibrosis and progressive loss of function over time [3]. Whether the native cardiac ECM component plays a role in this response remains unknown. It was also unknown how the cardiac ECM would perform when transplanted into a regenerative location such as skeletal muscle, and if the cardiac ECM is sufficiently distinct to initiate a different remodeling outcome. The results of this study do not demonstrate a difference between C-ECM and M-ECM scaffolds, indicating similar potential of these ECM sources.

Several remodeling characteristics were affected by ECM treatment. Implantation of each ECM scaffold was accompanied by rapid infiltration with mononuclear cells and angiogenesis, which is consistent with previous studies of ECM mediated muscle repair. This remodeling effect persisted until the final 180 day time point, in which scaffold remnants and high cellularity were still observed. There were some notable differences between ECM groups. The muscle ECM, though similar in appearance to other groups at both early time points, was more degraded than C-ECM and SIS-M after 180 days. The M-ECM group also corresponded to greater cellularity, though there were no observed differences in angiogenesis or innervation. M-ECM and C-ECM groups also presented a greater number of desmin and myosin heavy chain positive myofibers within the remodeling defect than SIS-M. Untreated defects, in contrast, appeared to have fully remodeled with only loose connective tissue and adipose tissue by the 56 day time point, which was also the response after 180 days.

An important outcome when evaluating muscle repair, is the in vivo effect on the restoration of muscle function. Functional muscle tissue cannot be assessed solely on histologic observation, since multiple events must occur in addition to muscle cell formation. Muscle fiber alignment, mature nerve formation, and neuromuscular junction formation are muscle repair processes that are necessary for muscle tissue to produce usable force [39]. The present study performed EMG recordings within the VML defect as a method of evaluating muscle function, which accounts for mature muscle formation as well as innervation under nervous system control. Therefore, EMG analysis only measures mature muscle that has also been functionally innervated. Innervation is necessary for not only proper function, but also for survival of the skeletal muscle, and cannot be confirmed by histologic methods alone. The present study showed that muscle and non-muscle ECM treatments were similarly effective in improving muscle recruitment metrics including the amplitude of the response ( $V_{PP}$  and  $V_{RMS}$ ) and the threshold of stimulation. The maximum amplitude is the result of the total muscle activity evoked by supramaximal stimulation and is correlated to the total amount of innervated muscle present within the recording area. Increased muscle activity may be the result of either increased myogenesis and innervation and/or improved survival of surrounding muscle fibers following defect creation since the electrodes were placed in the same anatomic location for each animal. Stimulation threshold is related the efficacy of stimulation, and larger diameter nerves have a lower threshold of applied electrical stimulation and correspondingly. The lowered threshold could be the result of an increased number of myofibers available for generation of a detectable response rather than nerve diameter. EMG provides a quantitative assessment of muscle function that is dependent on both muscle and nerve function, but it is not necessarily correlated with

force production. Muscle alignment, ECM attachment, and continuity with adjacent muscle fibers are all factors that will affect force production and are not detectable with EMG.

Multiple histologic and EMG characteristics are improved with ECM treatment compared to an untreated VML defect. The functional results of each ECM treatment, though an improvement over non-treated animals, were not statistically different from each other. There may have been a trend for improved EMG responses for M-ECM, though this was not significant. Also, the degree of improvement was likely small relative to non-muscle ECM and would not justify its use over clinically available non-muscle ECM such as SIS.

The ECM device preparation method used in the present study (i.e. molded ECM particulate devices) fully disrupted the native three dimensional structure of the ECM. This approach has been shown to be useful for two dimensional ECM (such as SIS sheets) that would not otherwise fill a three dimensional defect [56, 105, 195]. However, these methods may abrogate the instructive structural and mechanical cues in the ECM microenvironment and cannot be discounted. Even the M-ECM and C-ECM processing methods used in the present study substantially changed ECM structure. Cross-sectional sheets, though preserving microscale architecture, could not recapitulate the continuous tubular basement membrane structure found in native muscle ECM. The advantage to using a particulate device is that all ECM devices are able to be prepared in the same manner, controlling for architectural differences. The present study therefore isolated the effects of composition differences between ECMs, rather than structure.

Since robust differences between ECMs from different tissue sources were not observed *in vivo*, ECM structure may indeed play a significant role in the host response, necessitating future studies that examine ECM scaffolds with minimally disrupted architecture. Whole organ decellularization is currently the most effective method for preserving structure. Perfusion

methods have already been described for cardiac decellularization [151, 179, 202], though skeletal muscle is more challenging. Unlike the heart, which has natural large diameter inlets/outlets for perfusion (e.g. the aorta and pulmonary artery); skeletal muscle circulation is supported by multiple small vessels. The collateral circulation in skeletal muscle is advantageous in living tissue by enabling rapid increases in transport during high metabolic activity and allowing other vessels to compensate during infarction, but it presents a challenge for perfusion. Such small vessels are numerous and difficult to cannulate due to their small diameter (unpublished observations). Furthermore, while the heart is a compartmentalized organ, skeletal muscle has insertion points where perfusion solution may leak if it is dissected from the bone. As a result, there have been no descriptions of perfusion decellularized skeletal muscle to date. Intact skeletal muscle ECM has been prepared via immersion decellularization in rodents, primarily due to the small size of these tissues. Diffusion limitations make immersion decellularization ineffective for large animal muscle tissue sources, limiting clinical potential. The present study investigated porcine tissue, since this is the species used in many clinical products [74], including the commercially available SIS scaffold. Though, the structural contributions of muscle ECM can potentially be investigated in rodent animal models, novel methods of whole muscle decellularization would be needed in order to translate these results to large animal models and humans.

A limitation of the present study is the assumption that the decellularization treatments have equivalent effects upon the matrix structure and composition. The same tissue differences that necessitate different decellularization methods may also affect ECM exposure to each chemical. Therefore, small intestinal ECM, in which mild treatment is adequate for positive remodeling responses, may be more greatly affected than a dense tissue such as skeletal and

cardiac muscle. The chemicals required to decellularize muscle tissue is potentially a limitation in itself. The strong detergents and enzymatic treatments, though necessary for adequate cell removal, may remove factors in the matrix that are vital for a tissue specific response. In other words, the ECM scaffolds resulting from decellularization with the muscle ECM method may be too similar in composition due to removal of muscle specific factors to observe a difference. Another limitation of the present study is that remodeling had not yet concluded for all treatment groups. The C-ECM, SIS-M, SIS, and to a lesser extent M-ECM, all had visible scaffold remnants remaining on histologic analysis. This suggests that ECM degradation and remodeling has not concluded, and further functional improvements may be apparent at later time points. Previous studies have shown that remodeling and maturation of new muscle tissue can occur after the ECM has appeared to have fully degraded histologically [105, 107]. It is also unknown how gait biomechanics were affected by each treatment. Gait characteristics are not only a functional outcome, but may also affect remodeling. For example, if mice tend to unload their injured hindlimb in a particular treatment group due to pain or weakness, this would change the biomechanical forces felt by the area of remodeling. Previous studies have shown that mechanical loading environment greatly affects ECM remodeling outcome [75]

This aim has established that ECM implantation results in functional improvement after VML injury. ECM scaffolds are infiltrated by host mononuclear cells, are vascularized and innervated along the periphery, and encourage the formation of islands of skeletal muscle. Conclusive tissue specific effects were not observed, with each scaffold having similar effects on function as determined by EMG analysis. Nuanced differences in remodeling were observed, such as increased degradation for M-ECM scaffolds, though this did not result in a significant improvement from other ECM scaffolds.

## 5.0 SYNOPSIS, CONCLUSIONS, AND FUTURE DIRECTIONS

### 5.1 SYNOPSIS

The work presented in this dissertation characterized the composition, *in vitro* stem cell response, and *in vivo* remodeling characteristics of skeletal and cardiac muscle ECM for use as a bioinductive scaffold to restore functional muscle tissue after injury. The hypothesis of this study stated that the microenvironmental factors present in a muscle ECM scaffold would subsequently provide muscle specific signals and positively influence functional restoration following injury to a greater extent than a non-muscle scaffold. This was extended to both skeletal and cardiac ECM sources to determine whether striated muscle ECM in general possesses similar capacity to promote functional recovery. The effect of the muscle decellularization method upon the matrix was evaluated by comparing the muscle protocol to a milder method, which is sufficient for small intestinal submucosa decellularization only.

The first aim of this study was to develop a method of skeletal muscle decellularization from a large animal source that: (1) attained full decellularization according to previously established criteria, and (2) retained ECM specific components. This objective was achieved by chemically decellularizing skeletal muscle sheets using primarily trypsin, sodium deoxycholate, triton X-100, and peracetic acid. The resultant M-ECM contained only small amounts of low molecular weight DNA fragments, while preserving ECM components such as elastin,

glycosaminoglycans, growth factors, fibronectin, Types I, III, and IV collagen, and laminin. The M-ECM scaffold supported muscle progenitor cell growth *in vitro* and facilitated a constructive remodeling response *in vivo*. This decellularization method was also successfully applied to cardiac muscle and small intestinal submucosa, which preserved ECM biochemical and structural factors to a similar extent as M-ECM. SIS (decellularized with a single chemical exposure) retained the greatest proportions of these factors, confirming that the M-ECM method is more disruptive to the native ECM.

The second aim sought to characterize the effect of degradation products produced from muscle and non-muscle ECM scaffolds on PVSC proliferation and differentiation. PVSCs were isolated from both skeletal and cardiac muscle tissues; and thus each was derived from a skeletal or cardiac ECM microenvironmental niche. In the absence of serum mitogens in the culture medium, ECM degradation products from any source did not significantly affect PVSC proliferation in a tissue specific manner. Also, all ECM treatments were shown to inhibit proliferation in the presence of serum in the media. Following differentiation, PVSCs from skeletal muscle exhibited an immature myogenic phenotype, expressing both skeletal and cardiac muscle markers. ECM degradation products, but not Type I collagen, increased skeletal muscle PVSC differentiation in a non-tissue specific manner. Cardiac PVSCs did not effectively differentiate past an early cardiac phenotype, and did not respond to any ECM treatment.

The third and final aim characterized ECM remodeling in a murine model of VML. Implanted ECM underwent a remodeling process that included mononuclear cell infiltration within the ECM, degradation, angiogenesis, innervation, and early myogenesis. M-ECM was shown to cellularize and degrade more quickly on histologic evaluation than all other ECM scaffolds. ECM treatment improved the amount and stimulation capacity of skeletal muscle

within the VML defect compared to untreated animals as determined with EMG. However, there were not significant differences between different ECM types.

## **5.2 CONCLUSIONS**

The results of this dissertation do not support the hypothesis that a tissue specific M-ECM scaffold provides a positive benefit for muscle restoration applications. The decellularization method developed in this dissertation was effective at retaining ECM components relevant to muscle, though these did not influence tissue specific PVSCs in vitro or differentially affect functional recovery of a VML injury in vivo. Non-tissue specific ECM scaffolds composed of small intestinal submucosa are adequate to promote functional muscle remodeling.

## **5.3 FUTURE DIRECTIONS**

Though tissue specific effects were not observed in skeletal muscle tissue, there are other potential applications that would be relevant for skeletal and cardiac muscle repair as described below.

### **5.3.1 Hydrogel formulations of M-ECM and C-ECM**

Injectable, *in situ* polymerizing hydrogels are being used with increasing frequency for biomedical applications such as cell delivery, drug delivery, and/or as a scaffold for reconstruction of injured tissue [262]. Injectable hydrogels have several desirable features for

therapeutic applications including targeted delivery by minimally invasive techniques, ease of repeated delivery, ability to quickly fill an irregularly shaped space, and polymerization to form a support structure suitable for host cell infiltration and remodeling. Most of the investigated injectable hydrogels have been synthetic polymers with defined structural, chemical, and mechanical properties finely tuned for a desired application. However, there have been a number of recent descriptions of injectable hydrogels derived from naturally occurring biologic materials with purported superior biocompatibility and bioactivity compared to their synthetic counterparts. Common constituents of biologic hydrogels include Type I collagen, hyaluronic acid, or other proteins such as laminin as found in Matrigel [263].

It has been shown that biologic scaffold materials composed of the extracellular matrix (ECM) of decellularized tissues can be partially digested with pepsin, solubilized, and polymerized *in situ* to form a hydrogel [114, 120, 175, 250, 253, 264-266]. Intact ECM scaffold materials retain numerous molecular constituents found in the native tissue such as cell adhesion proteins, growth factors [223], and glycosaminoglycans and these materials support a constructive, site appropriate, remodeling response when implanted in a variety of anatomic sites including skeletal muscle [105, 107, 108], cardiac tissue [117], and the peripheral nervous system [267]. It is possible that a hydrogel formed from enzymatically degraded and solubilized ECM may maintain some of the biologic activity found in the intact ECM.

Both M-ECM and C- ECM hydrogels may be prepared from ECM degradation products. C-ECM in particular, may be prepared from tissue slices or from intact porcine heart ECM (Figure 41). Hydrogel formation occurs rapidly for these materials resulting in a highly hydrated, viscoelastic material. These mechanical properties have been characterized for M-ECM and

compared to UBM using parallel plate rheometry to determine the kinetics of gelation (Figure 42A) and viscoelastic nature (Figure 42B,C) of the hydrogel.

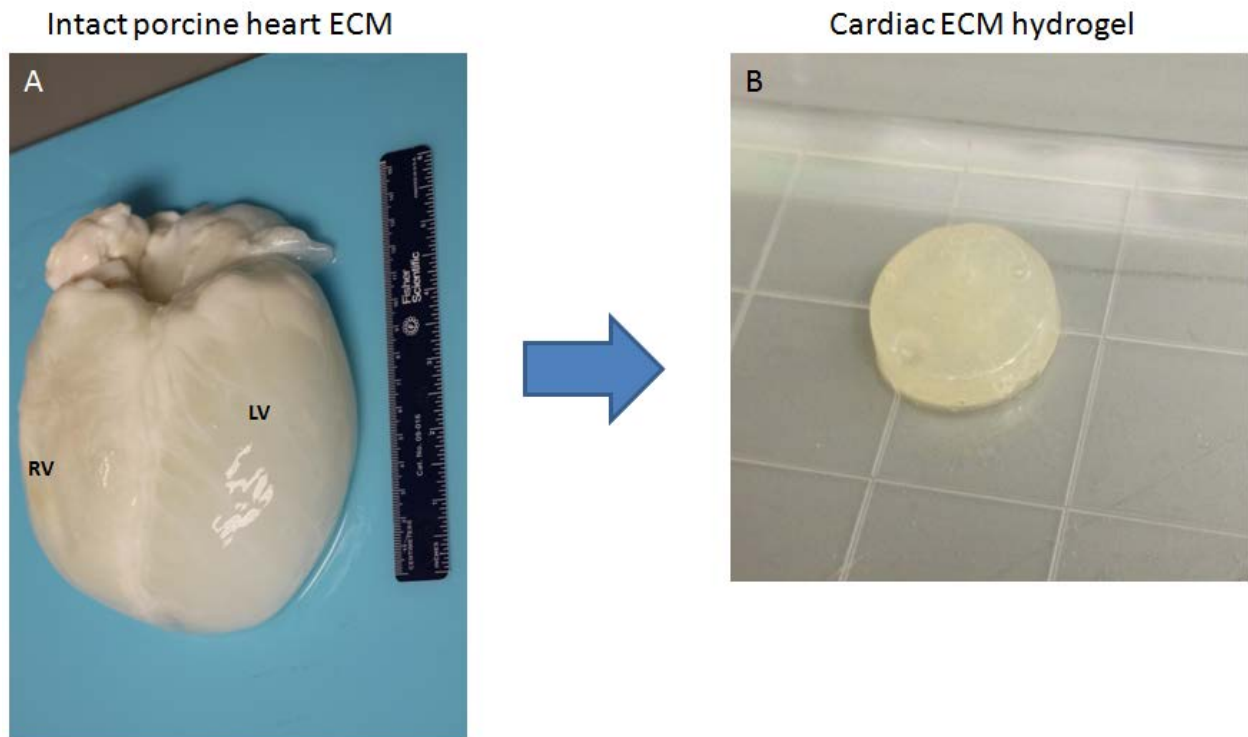


**Figure 42.** C- ECM (A) was prepared by decellularizing intact porcine hearts and then by performing pepsin digestion to prepare degradation products, which could then be used to create a C-ECM hydrogel (B) when brought to physiologic pH and temperature *in vitro*.

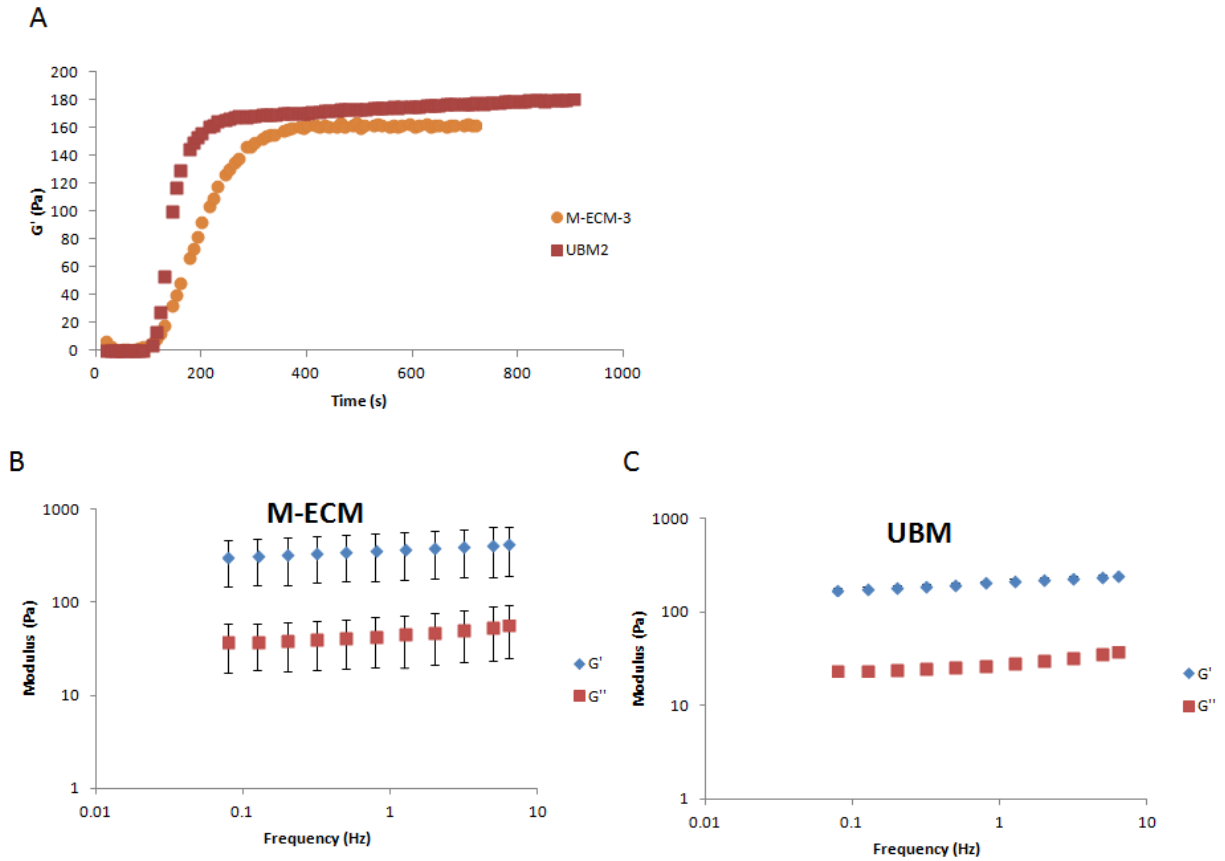


**Figure 43.** Rheological characterization of the mechanical properties of M-ECM and UBM hydrogels over time (A) and with varying shear stress frequency (B,C). Pepsin digested ECM was neutralized and brought to 37°C at time 0, and after a brief lag phase, storage modulus ( $G'$ ) rapidly increases, indicating hydrogel formation. The storage and loss modulus ( $G''$ ) was then characterized over a range of oscillatory shear strain frequencies.

### 5.3.2 ECM/Synthetic “biohybrid” devices for cardiac repair

The *in vivo* portion of this study compared muscle ECMs in a skeletal muscle injury location only. The logical corollary to this work would involve a determination of ECM tissue specificity in a cardiac repair model. As described previously, the cardiac wound healing environment is

very different from skeletal muscle, and may respond in a different manner to ECM. Furthermore, this allows direct testing of C-ECM in a cardiac location as compared to M-ECM using these same decellularization methods.

One such application is the development and use of tissue specific ECM biohybrid devices. Such devices are composed of both synthetic polymers and ECM scaffolds. The objective in developing these materials is to combine the advantages of synthetic materials, such as highly controllable mechanical properties, with the biologic activity inherent to the ECM. This approach has already tested for electrospun poly(ester urethane)urea (PEUU)/ECM hydrogel materials. [100, 265, 268]. PEUU is a biodegradable, elastomeric polymer that has been successfully incorporated with UBM and dermal ECM hydrogels, which improves *in vivo* remodeling characteristics such as cellular infiltration compared to the acellular polymer device. Preliminary studies are underway to fabricate C-ECM/PEUU hybrid scaffolds for use as a cardiac patch for support following MI (Figure 43). The electrospinning conditions have been optimized to provide anisotropic behavior matching native heart tissue, which has been shown to provide improved cardiac functional outcomes.

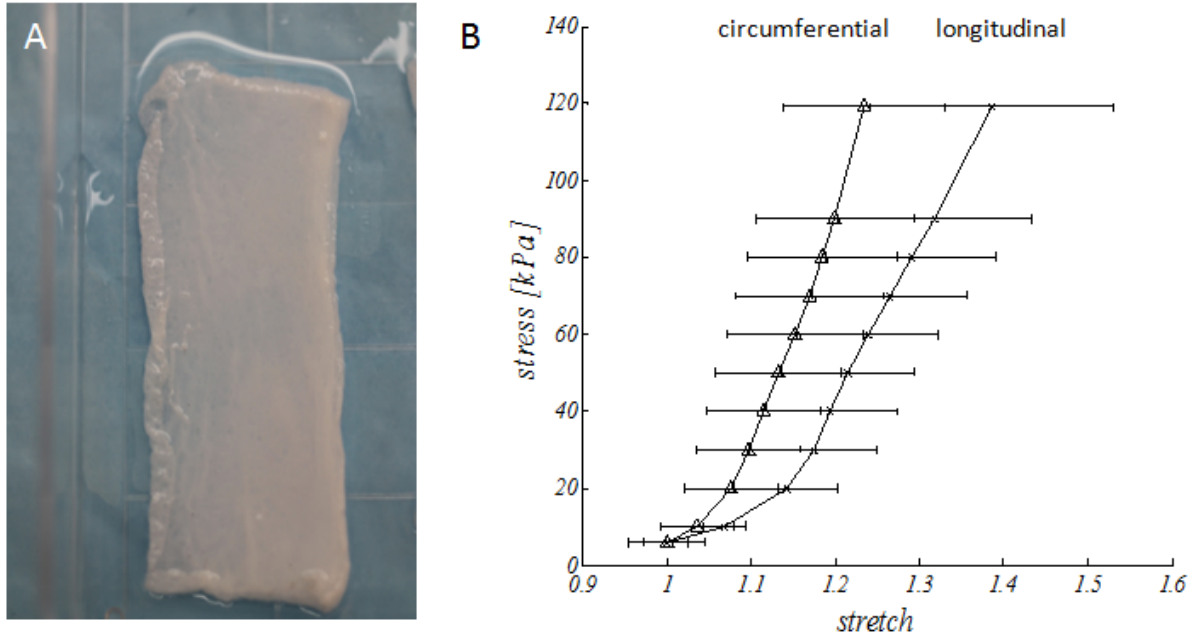


**Figure 44.** An ECM-PEUU biohybrid device for cardiac repair. (A) PEUU was electrospun concurrently with electrospayed dermal ECM pepsin digest, which formed an ECM hydrogel component of the device. (B) Electrospinning parameters were optimized to provide anisotropic biaxial mechanical properties such as those seen in the native heart. Images and mechanics courtesy of a collaboration with Dr. Antonio D'Amore and the Wagner lab.

## APPENDIX A

### IMAGEJ SCRIPT USED FOR BRDU QUANTIFICATION

```
//BrdU well counter v2.txt
//author: Matt Wolf
//Version 2. 7-1-13
```

```
dir1 = getDirectory("Choose Source Directory ");
list = getFileList(dir1);
setBatchMode(true);
```

```
//get inputs-----
Dialog.create("Well Counter Inputs for RGB Images");
```

```
Dialog.addMessage("\n\nThe parameters below need to be manually tested and validated for each
batch of staining. The blue channel is assumed to be nuclear. \n\nAll images in a group must be
imaged using the same fluorophores and exposure times. Each folder of images requires a
positive control image. Negative controls are recommended.");
```

```
Dialog.addMessage("1. Enter Channels to be analyzed. \n Blue, Green, or Red");
Dialog.addCheckboxGroup(1,3,newArray("Red","Green","Blue"),newArray(false,true,true));
```

```
Dialog.addMessage("1. Enter the ball radius (px) for background correction. \n Radius must be
greater than the radius of the largest object that is not background. (staining, exposure time, and
focus may alter image size) \n100X DAPI stained nuclei have an approximate max radius of 7-
12 px.");
```

```
Dialog.addNumber("Ball Radius:", 15,0,8,"px");
```

```
Dialog.addMessage("2. Apply Gaussian Blur and Watershed? \n Watershedding will split up 2
objects that touch each other, and gaussian blur prevents oversplitting.");
Dialog.addCheckbox("Apply blur and watershed?", true);
```

```
Dialog.addMessage("3. Enter the automatic thresholding method \nFrom least to most strict:  
Huang, Li, IsoData, Otsu");
```

```
Dialog.addChoice("Thresholding Method:", newArray("Li", "Huang", "IsoData", "Otsu"));
```

```
Dialog.addMessage("4. Enter the upper/lower limit for the size of the object. \n Objects  
smaller/larger than this value are ignored. 100X DAPI stained nuclei have an approximate area  
of 100-500 px^2 after blurring and thresholding");
```

```
Dialog.addNumber("Minimum Size:", 50,0,8,"px^2");
```

```
Dialog.addNumber("Maximum Size:", 3000,0,8,"px^2");
```

```
Dialog.addMessage("5. Enter the lower limit (between 0 and 1.0) for the circularity of the  
object. \n Objects below this circularity are ignored. 1.0 indicates a perfect circle.");
```

```
Dialog.addNumber("Minimum Circularity:", 0.7,2,8,"");
```

```
Dialog.addMessage("6. Show Outlines? \n Will save the masked image with each counted  
object numbered.");
```

```
Dialog.addCheckbox("Show and save outlines?", true);
```

```
Dialog.show();
```

```
// user inputs defined-----
```

```
redchan = Dialog.getCheckbox();
```

```
greenchan = Dialog.getCheckbox();
```

```
bluechan = Dialog.getCheckbox();
```

```
balla = Dialog.getNumber();
```

```
blurshed = Dialog.getCheckbox();
```

```
threshtype = Dialog.getChoice();
```

```
lowsize = Dialog.getNumber();
```

```
hisize = Dialog.getNumber();
```

```
lowcirc = Dialog.getNumber();
```

```
outliner = Dialog.getCheckbox();
```

```
//generate threshold from control-----
```

```
showMessage("Select a positive control image to set threshold limits");
```

```
open();
```

```
controlimage = getTitle();
```

```
run("Split Channels");
```

```
selectImage(1);
```

```
if (redchan==1){
```

```
run("Enhance Contrast", "saturated=0.5 normalize");
```

```
run("Subtract Background...", "rolling=" + balla);
```

```
if (blurshed==true) run("Gaussian Blur...", "sigma=2");
```

```
setAutoThreshold(threshtype + " dark");
```

```
getThreshold(RedMin, RedMax);
```

```
resetThreshold;}
```

```

else {
    RedMin = "NA"; RedMax = "NA";}

selectImage(2);
if (greenchan==1){
    run("Enhance Contrast", "saturated=0.5 normalize");
    run("Subtract Background...", "rolling=" + balla);
    if (blurshed==true) run("Gaussian Blur...", "sigma=2");
    setAutoThreshold(threshtype + " dark");
    getThreshold(GreenMin, GreenMax);
    resetThreshold;}
else {
    GreenMin = "NA"; GreenMax = "NA";}

selectImage(3);
if (bluechan==1){
    run("Enhance Contrast", "saturated=0.5 normalize equalize");
    run("Subtract Background...", "rolling=" + balla);
    if (blurshed==true) run("Gaussian Blur...", "sigma=2");
    setAutoThreshold(threshtype + " dark");
    getThreshold(BlueMin, BlueMax);
    resetThreshold;}
else {
    BlueMin = "NA"; BlueMax = "NA";}

//show parameters used during analysis-----
print("control image used:" + controlimage + "\nrolling ball radius = " + balla + "\nblur and
watershed? = " + blurshed + "\nthresholding method = " + threshtype + "\nlower particle size
limit = " + lowsize + "\nupper particle size = " + hisize + "\nlower limit of circularity = " +
lowcirc + "\nRed lower threshold = " + RedMin + "\nRed upper threshold = " + RedMax +
"\nGreen lower threshold = " + GreenMin + "\nGreen upper threshold = " + GreenMax + "\nBlue
lower threshold = " + BlueMin + "\nBlue upper threshold = " + BlueMax);
run("Close All");

//analyze each image in directory-----
for (i=0; i<list.length; i++) {
    showProgress(i+1, list.length);
    open(dir1+list[i]);
    wellcounter();
    run("Close All");
}

//primary function to count each image-----
function wellcounter() {

run("Split Channels");

```

```
//image preprocessing, thresholding, and counting for each channel-----
-----
if (greenchan==1){
    selectImage(2);
    run("Enhance Contrast", "saturated=0.5");
    run("Subtract Background...", "rolling=" + balla);
    if (blurshed==true) run("Gaussian Blur...", "sigma=2");
    setThreshold(GreenMin, GreenMax);
    run("Convert to Mask");
    resetThreshold();
    if (blurshed==true) run("Watershed");
    imagename2 = getTitle();
    if (outliner==false) {
        run("Analyze Particles...", "size=" + lowsize + "-" + hisize + " circularity=" +
lowcirc + "-1.00 show=Nothing summarize");
    }
    else {
        run("Analyze Particles...", "size=" + lowsize + "-" + hisize + " circularity=" +
lowcirc + "-1.00 show=[Overlay Masks] summarize");
        OutlineDir= dir1 + "\Outlines\\";
        File.makeDirectory(OutlineDir);
        saveAs("JPEG", OutlineDir + imagename2 + "-outline.tif");
    }
}

if (bluechan==1){
    selectImage(3);
    run("Enhance Contrast", "saturated=0.5 equalize");
    run("Subtract Background...", "rolling=" + balla);
    if (blurshed==true) run("Gaussian Blur...", "sigma=2");
    setThreshold(BlueMin, BlueMax);
    run("Convert to Mask");
    resetThreshold();
    if (blurshed==true) run("Watershed");
    imagename3 = getTitle();
    if (outliner==false) {
        run("Analyze Particles...", "size=" + lowsize + "-" + hisize + " circularity=" +
lowcirc + "-1.00 show=Nothing summarize");
    }
    else {
        run("Analyze Particles...", "size=" + lowsize + "-" + hisize + " circularity=" +
lowcirc + "-1.00 show=[Overlay Masks] summarize");
        OutlineDir= dir1 + "\Outlines\\";
        File.makeDirectory(OutlineDir);
        saveAs("JPEG", OutlineDir + imagename3 + "-outline.tif");
    }
}

```

```

    }
}

//colocalization of green and blue
if (bluechan==1 && greenchan==1){
    imageCalculator("and create",2,3);
    if (outliner==false) {
        run("Analyze Particles...", "size=" + lowsize + "-" + hisize + " circularity=" +
lowcirc + "-1.00 show=Nothing summarize");
    }
    else {
        run("Analyze Particles...", "size=" + lowsize + "-" + hisize + " circularity=" +
lowcirc + "-1.00 show=[Overlay Masks] summarize");
        OutlineDir= dir1 + "\Outlines\\";
        File.makeDirectory(OutlineDir);
        imagename23 = getTitle();
        saveAs("JPEG", OutlineDir + imagename23 + "-green blue colocal outline.tif");
    }
}

//colocalization of red and blue
if (bluechan==1 && redchan==1){
    imageCalculator("and create",1,3);
    if (outliner==false) {
        run("Analyze Particles...", "size=" + lowsize + "-" + hisize + " circularity=" +
lowcirc + "-1.00 show=Nothing summarize");
    }
    else {
        run("Analyze Particles...", "size=" + lowsize + "-" + hisize + " circularity=" +
lowcirc + "-1.00 show=[Overlay Masks] summarize");
        OutlineDir= dir1 + "\Outlines\\";
        File.makeDirectory(OutlineDir);
        imagename13 = getTitle();
        saveAs("JPEG", OutlineDir + imagename13 + "-red blue colocal outline.tif");
    }
}
}

```

## BIBLIOGRAPHY

- [1] Roger VL, Go AS, Lloyd-Jones DM, Benjamin EJ, Berry JD, Borden WB, et al. Heart disease and stroke statistics--2012 update: a report from the American Heart Association. *Circulation* 2012;125(1):e2-e220.
- [2] Zamilpa R, Lindsey ML. Extracellular matrix turnover and signaling during cardiac remodeling following MI: causes and consequences. *J Mol Cell Cardiol* 2010;48(3):558-63.
- [3] Burchfield JS, Xie M, Hill JA. Pathological ventricular remodeling: mechanisms: part 1 of 2. *Circulation* 2013;128(4):388-400.
- [4] Ozawa T, Mickle DA, Weisel RD, Koyama N, Wong H, Ozawa S, et al. Histologic changes of nonbiodegradable and biodegradable biomaterials used to repair right ventricular heart defects in rats. *J Thorac Cardiovasc Surg* 2002;124(6):1157-64.
- [5] Caimmi PP, Grossini E, Kapetanakis EI, Boido R, Coppo C, Scappellato F, et al. Double patch repair through a single ventriculotomy for ischemic ventricular septal defects. *Ann Thorac Surg* 2010;89(5):1679-81.
- [6] Givertz MM. Heart allocation in the United States: intended and unintended consequences. *Circ Heart Fail* 2012;5(2):140-3.
- [7] Wolfe RA, Roys EC, Merion RM. Trends in organ donation and transplantation in the United States, 1999-2008. *Am J Transplant* 2010;10(4 Pt 2):961-72.
- [8] Bruggink AH, van Oosterhout MF, de Jonge N, Ivangh B, van Kuik J, Voorbij RH, et al. Reverse remodeling of the myocardial extracellular matrix after prolonged left ventricular assist device support follows a biphasic pattern. *J Heart Lung Transplant* 2006;25(9):1091-8.
- [9] Park SJ, Milano CA, Tatooles AJ, Rogers JG, Adamson RM, Steidley DE, et al. Outcomes in advanced heart failure patients with left ventricular assist devices for destination therapy. *Circ Heart Fail* 2012;5(2):241-8.
- [10] Grogan BF, Hsu JR. Volumetric muscle loss. *J Am Acad Orthop Surg* 2011;19 Suppl 1:S35-7.

- [11] Clauser L, Curioni C, Spanio S. The use of the temporalis muscle flap in facial and craniofacial reconstructive surgery. A review of 182 cases. *J Craniomaxillofac Surg* 1995;23(4):203-14.
- [12] Fino P, Paolo F, Massera D, Amorosi V, Onesti MG. Nonsurgical treatment of a massive substance loss. *Case Rep Med* 2013;2013:716549.
- [13] Isik S, Sezgin M, Ozturk S, Selmanpakoglu N, Kutukcu Y. Free musculofasciocutaneous medial plantar flap for reconstruction of thenar defects. *Br J Plast Surg* 1997;50(2):116-20.
- [14] Lorenzetti F, Lazzeri D, Bonini L, Giannotti G, Piolanti N, Lisanti M, et al. Distally based peroneus brevis muscle flap in reconstructive surgery of the lower leg: Postoperative ankle function and stability evaluation. *J Plast Reconstr Aesthet Surg* 2010;63(9):1523-33.
- [15] Luck RP, Verbin S. Rhabdomyolysis: a review of clinical presentation, etiology, diagnosis, and management. *Pediatr Emerg Care* 2008;24(4):262-8.
- [16] Celikoz B, Sengezer M, Isik S, Turegun M, Deveci M, Duman H, et al. Subacute reconstruction of lower leg and foot defects due to high velocity-high energy injuries caused by gunshots, missiles, and land mines. *Microsurgery* 2005;25(1):3-14; discussion 5.
- [17] Champion HR, Bellamy RF, Roberts CP, Leppaniemi A. A profile of combat injury. *J Trauma* 2003;54(5 Suppl):S13-9.
- [18] Kumar AR, Grewal NS, Chung TL, Bradley JP. Lessons from the modern battlefield: successful upper extremity injury reconstruction in the subacute period. *J Trauma* 2009;67(4):752-7.
- [19] Ramasamy A, Hinsley DE, Edwards DS, Stewart MP, Midwinter M, Parker PJ. Skill sets and competencies for the modern military surgeon: lessons from UK military operations in Southern Afghanistan. *Injury* 2010;41(5):453-9.
- [20] Rodriguez ED, Bluebond-Langner R, Copeland C, Grim TN, Singh NK, Scalea T. Functional outcomes of posttraumatic lower limb salvage: a pilot study of anterolateral thigh perforator flaps versus muscle flaps. *J Trauma* 2009;66(5):1311-4.
- [21] Cross JD, Ficke JR, Hsu JR, Masini BD, Wenke JC. Battlefield orthopaedic injuries cause the majority of long-term disabilities. *J Am Acad Orthop Surg* 2011;19 Suppl 1:S1-7.
- [22] Masini BD, Waterman SM, Wenke JC, Owens BD, Hsu JR, Ficke JR. Resource utilization and disability outcome assessment of combat casualties from Operation Iraqi Freedom and Operation Enduring Freedom. *J Orthop Trauma* 2009;23(4):261-6.
- [23] Masini BD, Owens BD, Hsu JR, Wenke JC. Rehospitalization after combat injury. *J Trauma* 2011;71(1 Suppl):S98-102.

- [24] Pollak AN, Jones AL, Castillo RC, Bosse MJ, MacKenzie EJ. The relationship between time to surgical debridement and incidence of infection after open high-energy lower extremity trauma. *J Bone Joint Surg Am* 2010;92(1):7-15.
- [25] Pollak AN, Ficke CJ. Extremity war injuries: collaborative efforts in research, host nation care, and disaster preparedness. *J Am Acad Orthop Surg* 2010;18(1):3-9.
- [26] Branco BC, Inaba K, Barmparas G, Schnuriger B, Lustenberger T, Talving P, et al. Incidence and predictors for the need for fasciotomy after extremity trauma: a 10-year review in a mature level I trauma centre. *Injury* 2011;42(10):1157-63.
- [27] Mabvuure NT, Malahias M, Hindocha S, Khan W, Juma A. Acute compartment syndrome of the limbs: current concepts and management. *Open Orthop J* 2012;6:535-43.
- [28] Ritenour AE, Dorlac WC, Fang R, Woods T, Jenkins DH, Flaherty SF, et al. Complications after fasciotomy revision and delayed compartment release in combat patients. *J Trauma* 2008;64(2 Suppl):S153-61; discussion S61-2.
- [29] Waterman BR, Liu J, Newcomb R, Schoenfeld AJ, Orr JD, Belmont PJ, Jr. Risk factors for chronic exertional compartment syndrome in a physically active military population. *Am J Sports Med* 2013;41(11):2545-9.
- [30] Waterman BR, Laughlin M, Kilcoyne K, Cameron KL, Owens BD. Surgical treatment of chronic exertional compartment syndrome of the leg: failure rates and postoperative disability in an active patient population. *J Bone Joint Surg Am* 2013;95(7):592-6.
- [31] Adams JE, Kircher MF, Spinner RJ, Torchia ME, Bishop AT, Shin AY. Complications and outcomes of functional free gracilis transfer in brachial plexus palsy. *Acta Orthop Belg* 2009;75(1):8-13.
- [32] Adams WP, Jr., Lipschitz AH, Ansari M, Kenkel JM, Rohrich RJ. Functional donor site morbidity following latissimus dorsi muscle flap transfer. *Ann Plast Surg* 2004;53(1):6-11.
- [33] Barrie KA, Steinmann SP, Shin AY, Spinner RJ, Bishop AT. Gracilis free muscle transfer for restoration of function after complete brachial plexus avulsion. *Neurosurg Focus* 2004;16(5):E8.
- [34] Arnold PG, Pairolero PC. Chest-wall reconstruction: an account of 500 consecutive patients. *Plast Reconstr Surg* 1996;98(5):804-10.
- [35] Lee SL, Poulos ND, Greenholz SK. Staged reconstruction of large congenital diaphragmatic defects with synthetic patch followed by reverse latissimus dorsi muscle. *J Pediatr Surg* 2002;37(3):367-70.
- [36] Lin SJ, Butler CE. Subtotal thigh flap and bioprosthetic mesh reconstruction for large, composite abdominal wall defects. *Plast Reconstr Surg* 2010;125(4):1146-56.

- [37] Asher RA, Morgenstern DA, Moon LD, Fawcett JW. Chondroitin sulphate proteoglycans: inhibitory components of the glial scar. *Prog Brain Res* 2001;132:611-9.
- [38] Fawcett JW, Asher RA. The glial scar and central nervous system repair. *Brain Res Bull* 1999;49(6):377-91.
- [39] Charge SB, Rudnicki MA. Cellular and molecular regulation of muscle regeneration. *Physiol Rev* 2004;84(1):209-38.
- [40] Ciciliot S, Schiaffino S. Regeneration of mammalian skeletal muscle. Basic mechanisms and clinical implications. *Curr Pharm Des* 2010;16(8):906-14.
- [41] Zammit PS, Relaix F, Nagata Y, Ruiz AP, Collins CA, Partridge TA, et al. Pax7 and myogenic progression in skeletal muscle satellite cells. *J Cell Sci* 2006;119(Pt 9):1824-32.
- [42] Scharner J, Zammit PS. The muscle satellite cell at 50: the formative years. *Skelet Muscle* 2011;1(1):28.
- [43] Sambasivan R, Yao R, Kissenpfennig A, Van Wittenberghe L, Paldi A, Gayraud-Morel B, et al. Pax7-expressing satellite cells are indispensable for adult skeletal muscle regeneration. *Development* 2011;138(17):3647-56.
- [44] Lepper C, Partridge TA, Fan CM. An absolute requirement for Pax7-positive satellite cells in acute injury-induced skeletal muscle regeneration. *Development* 2011;138(17):3639-46.
- [45] Gunther S, Kim J, Kostin S, Lepper C, Fan CM, Braun T. Myf5-positive satellite cells contribute to pax7-dependent long-term maintenance of adult muscle stem cells. *Cell Stem Cell* 2013;13(5):590-601.
- [46] Kuang S, Kuroda K, Le Grand F, Rudnicki MA. Asymmetric self-renewal and commitment of satellite stem cells in muscle. *Cell* 2007;129(5):999-1010.
- [47] Conboy IM, Rando TA. The regulation of Notch signaling controls satellite cell activation and cell fate determination in postnatal myogenesis. *Dev Cell* 2002;3(3):397-409.
- [48] Seale P, Rudnicki MA. A new look at the origin, function, and "stem-cell" status of muscle satellite cells. *Dev Biol* 2000;218(2):115-24.
- [49] Huard J, Li Y, Fu FH. Muscle injuries and repair: current trends in research. *J Bone Joint Surg Am* 2002;84-A(5):822-32.
- [50] Mann CJ, Perdiguero E, Kharraz Y, Aguilar S, Pessina P, Serrano AL, et al. Aberrant repair and fibrosis development in skeletal muscle. *Skelet Muscle* 2011;1(1):21.
- [51] Delgado I, Huang X, Jones S, Zhang L, Hatcher R, Gao B, et al. Dynamic gene expression during the onset of myoblast differentiation in vitro. *Genomics* 2003;82(2):109-21.

- [52] Braun T, Gautel M. Transcriptional mechanisms regulating skeletal muscle differentiation, growth and homeostasis. *Nat Rev Mol Cell Biol* 2011;12(6):349-61.
- [53] Sanes JR, Lichtman JW. Induction, assembly, maturation and maintenance of a postsynaptic apparatus. *Nat Rev Neurosci* 2001;2(11):791-805.
- [54] Grounds MD, Sorokin L, White J. Strength at the extracellular matrix-muscle interface. *Scand J Med Sci Sports* 2005;15(6):381-91.
- [55] Kraft GH. Fibrillation potential amplitude and muscle atrophy following peripheral nerve injury. *Muscle Nerve* 1990;13(9):814-21.
- [56] Sicari BM, Agrawal V, Siu BF, Medberry CJ, Dearth CL, Turner NJ, et al. A murine model of volumetric muscle loss and a regenerative medicine approach for tissue replacement. *Tissue Eng Part A* 2012;18(19-20):1941-8.
- [57] Sussman M. Duchenne muscular dystrophy. *J Am Acad Orthop Surg* 2002;10(2):138-51.
- [58] Bergmann O, Bhardwaj RD, Bernard S, Zdunek S, Barnabe-Heider F, Walsh S, et al. Evidence for cardiomyocyte renewal in humans. *Science* 2009;324(5923):98-102.
- [59] Schlesinger J, Schueler M, Grunert M, Fischer JJ, Zhang Q, Krueger T, et al. The cardiac transcription network modulated by Gata4, Mef2a, Nkx2.5, Srf, histone modifications, and microRNAs. *PLoS Genet* 2011;7(2):e1001313.
- [60] Rutland CS, Polo-Parada L, Ehler E, Alibhai A, Thorpe A, Suren S, et al. Knockdown of embryonic myosin heavy chain reveals an essential role in the morphology and function of the developing heart. *Development* 2011;138(18):3955-66.
- [61] Grefte S, Kuijpers-Jagtman AM, Torensma R, Von den Hoff JW. Skeletal muscle development and regeneration. *Stem Cells Dev* 2007;16(5):857-68.
- [62] Schabort EJ, Myburgh KH, Wiehe JM, Torzewski J, Niesler CU. Potential myogenic stem cell populations: sources, plasticity, and application for cardiac repair. *Stem Cells Dev* 2009;18(6):813-30.
- [63] Barile L, Messina E, Giacomello A, Marban E. Endogenous cardiac stem cells. *Prog Cardiovasc Dis* 2007;50(1):31-48.
- [64] Bolli R, Tang XL, Sanganalmath SK, Rimoldi O, Mosna F, Abdel-Latif A, et al. Intracoronary delivery of autologous cardiac stem cells improves cardiac function in a porcine model of chronic ischemic cardiomyopathy. *Circulation* 2013;128(2):122-31.
- [65] Makkar RR, Smith RR, Cheng K, Malliaras K, Thomson LE, Berman D, et al. Intracoronary cardiosphere-derived cells for heart regeneration after myocardial infarction (CADUCEUS): a prospective, randomised phase 1 trial. *Lancet* 2012;379(9819):895-904.

- [66] Bissell MJ, Hall HG, Parry G. How does the extracellular matrix direct gene expression? *J Theor Biol* 1982;99(1):31-68.
- [67] Xu R, Boudreau A, Bissell MJ. Tissue architecture and function: dynamic reciprocity via extra- and intra-cellular matrices. *Cancer Metastasis Rev* 2009;28(1-2):167-76.
- [68] Bedossa P, Paradis V. Liver extracellular matrix in health and disease. *J Pathol* 2003;200(4):504-15.
- [69] Gullberg D, Tiger CF, Velling T. Laminins during muscle development and in muscular dystrophies. *Cell Mol Life Sci* 1999;56(5-6):442-60.
- [70] Pegoraro E, Marks H, Garcia CA, Crawford T, Mancias P, Connolly AM, et al. Laminin alpha2 muscular dystrophy: genotype/phenotype studies of 22 patients. *Neurology* 1998;51(1):101-10.
- [71] Gilbert TW, Stewart-Akers AM, Simmons-Byrd A, Badylak SF. Degradation and remodeling of small intestinal submucosa in canine Achilles tendon repair. *J Bone Joint Surg Am* 2007;89(3):621-30.
- [72] Gilbert TW, Stewart-Akers AM, Badylak SF. A quantitative method for evaluating the degradation of biologic scaffold materials. *Biomaterials* 2007;28(2):147-50.
- [73] Badylak SF, Freytes DO, Gilbert TW. Extracellular matrix as a biological scaffold material: Structure and function. *Acta Biomater* 2009;5(1):1-13.
- [74] Crapo PM, Gilbert TW, Badylak SF. An overview of tissue and whole organ decellularization processes. *Biomaterials* 2011;32(12):3233-43.
- [75] Boruch AV, Nieponice A, Qureshi IR, Gilbert TW, Badylak SF. Constructive Remodeling of Biologic Scaffolds is Dependent on Early Exposure to Physiologic Bladder Filling in a Canine Partial Cystectomy Model. *J Surg Res* 2009.
- [76] Nuininga JE, van Moerkerk H, Hanssen A, Hulsbergen CA, Oosterwijk-Wakka J, Oosterwijk E, et al. A rabbit model to tissue engineer the bladder. *Biomaterials* 2004;25(9):1657-61.
- [77] Reddy PP, Barrieras DJ, Wilson G, Bagli DJ, McLorie GA, Khoury AE, et al. Regeneration of functional bladder substitutes using large segment acellular matrix allografts in a porcine model. *J Urol* 2000;164(3 Pt 2):936-41.
- [78] Zhang Y, Kropp BP, Lin HK, Cowan R, Cheng EY. Bladder regeneration with cell-seeded small intestinal submucosa. *Tissue Eng* 2004;10(1-2):181-7.
- [79] Badylak SF, Vorp DA, Spievack AR, Simmons-Byrd A, Hanke J, Freytes DO, et al. Esophageal reconstruction with ECM and muscle tissue in a dog model. *J Surg Res* 2005;128(1):87-97.

- [80] Clough A, Ball J, Smith GS, Leibman S. Porcine small intestine submucosa matrix (Surgisis) for esophageal perforation. *Ann Thorac Surg* 2011;91(2):e15-6.
- [81] Nieponice A, Gilbert TW, Badylak SF. Reinforcement of esophageal anastomoses with an extracellular matrix scaffold in a canine model. *Ann Thorac Surg* 2006;82(6):2050-8.
- [82] Nieponice A, McGrath K, Qureshi I, Beckman EJ, Luketich JD, Gilbert TW, et al. An extracellular matrix scaffold for esophageal stricture prevention after circumferential EMR. *Gastrointest Endosc* 2009;69(2):289-96.
- [83] Urita Y, Komuro H, Chen G, Shinya M, Kaneko S, Kaneko M, et al. Regeneration of the esophagus using gastric acellular matrix: an experimental study in a rat model. *Pediatr Surg Int* 2007;23(1):21-6.
- [84] Soto-Gutierrez A, Zhang L, Medberry C, Fukumitsu K, Faulk D, Jiang H, et al. A whole-organ regenerative medicine approach for liver replacement. *Tissue Eng Part C Methods* 2011;17(6):677-86.
- [85] Uygun BE, Soto-Gutierrez A, Yagi H, Izamis ML, Guzzardi MA, Shulman C, et al. Organ reengineering through development of a transplantable recellularized liver graft using decellularized liver matrix. *Nat Med* 2010;16(7):814-20.
- [86] Zhou P, Lessa N, Estrada DC, Severson EB, Lingala S, Zern MA, et al. Decellularized liver matrix as a carrier for the transplantation of human fetal and primary hepatocytes in mice. *Liver Transpl* 2011;17(4):418-27.
- [87] Brizzola S, de Eguileor M, Brevini T, Grimaldi A, Congiu T, Neuenschwander P, et al. Morphologic features of biocompatibility and neoangiogenesis onto a biodegradable tracheal prosthesis in an animal model. *Interact Cardiovasc Thorac Surg* 2009;8(6):610-4.
- [88] Ott HC, Clippinger B, Conrad C, Schuetz C, Pomerantseva I, Ikonomou L, et al. Regeneration and orthotopic transplantation of a bioartificial lung. *Nat Med* 2010;16(8):927-33.
- [89] Remlinger NT, Czajka CA, Juhas ME, Vorp DA, Stolz DB, Badylak SF, et al. Hydrated xenogeneic decellularized tracheal matrix as a scaffold for tracheal reconstruction. *Biomaterials* 2010;31(13):3520-6.
- [90] Agrawal V, Brown BN, Beattie AJ, Gilbert TW, Badylak SF. Evidence of innervation following extracellular matrix scaffold-mediated remodelling of muscular tissues. *J Tissue Eng Regen Med* 2009;3(8):590-600.
- [91] Clarke KM, Lantz GC, Salisbury SK, Badylak SF, Hiles MC, Voytik SL. Intestine submucosa and polypropylene mesh for abdominal wall repair in dogs. *J Surg Res* 1996;60(1):107-14.
- [92] Conconi MT, Bellini S, Teoli D, de Coppi P, Ribatti D, Nico B, et al. In vitro and in vivo evaluation of acellular diaphragmatic matrices seeded with muscle precursors cells and coated

with VEGF silica gels to repair muscle defect of the diaphragm. *J Biomed Mater Res A* 2009;89(2):304-16.

[93] Conconi MT, De Coppi P, Bellini S, Zara G, Sabatti M, Marzaro M, et al. Homologous muscle acellular matrix seeded with autologous myoblasts as a tissue-engineering approach to abdominal wall-defect repair. *Biomaterials* 2005;26(15):2567-74.

[94] Daly KA, Stewart-Akers AM, Hara H, Ezzelarab M, Long C, Cordero K, et al. Effect of the alphaGal epitope on the response to small intestinal submucosa extracellular matrix in a nonhuman primate model. *Tissue Eng Part A* 2009;15(12):3877-88.

[95] De Coppi P, Bellini S, Conconi MT, Sabatti M, Simonato E, Gamba PG, et al. Myoblast-acellular skeletal muscle matrix constructs guarantee a long-term repair of experimental full-thickness abdominal wall defects. *Tissue Eng* 2006;12(7):1929-36.

[96] Desai KM, Diaz S, Dorward IG, Winslow ER, La Regina MC, Halpin V, et al. Histologic results 1 year after bioprosthetic repair of paraesophageal hernia in a canine model. *Surg Endosc* 2006;20(11):1693-7.

[97] Franklin ME, Jr., Trevino JM, Portillo G, Vela I, Glass JL, Gonzalez JJ. The use of porcine small intestinal submucosa as a prosthetic material for laparoscopic hernia repair in infected and potentially contaminated fields: long-term follow-up. *Surg Endosc* 2008;22(9):1941-6.

[98] Gamba PG, Conconi MT, Lo Piccolo R, Zara G, Spinazzi R, Parnigotto PP. Experimental abdominal wall defect repaired with acellular matrix. *Pediatr Surg Int* 2002;18(5-6):327-31.

[99] Gilbert TW, Nieponice A, Spievack AR, Holcomb J, Gilbert S, Badylak SF. Repair of the thoracic wall with an extracellular matrix scaffold in a canine model. *J Surg Res* 2008;147(1):61-7.

[100] Hong Y, Takanari K, Amoroso NJ, Hashizume R, Brennan-Pierce EP, Freund JM, et al. An elastomeric patch electrospun from a blended solution of dermal extracellular matrix and biodegradable polyurethane for rat abdominal wall repair. *Tissue Eng Part C Methods* 2012;18(2):122-32.

[101] Merritt EK, Cannon MV, Hammers DW, Le LN, Gokhale R, Sarathy A, et al. Repair of traumatic skeletal muscle injury with bone-marrow-derived mesenchymal stem cells seeded on extracellular matrix. *Tissue Eng Part A* 2010;16(9):2871-81.

[102] Merritt EK, Hammers DW, Tierney M, Suggs LJ, Walters TJ, Farrar RP. Functional assessment of skeletal muscle regeneration utilizing homologous extracellular matrix as scaffolding. *Tissue Eng Part A* 2010;16(4):1395-405.

[103] Smith MJ, Paran TS, Quinn F, Corbally MT. The SIS extracellular matrix scaffold-preliminary results of use in congenital diaphragmatic hernia (CDH) repair. *Pediatr Surg Int* 2004;20(11-12):859-62.

- [104] Tottey S, Johnson SA, Crapo PM, Reing JE, Zhang L, Jiang H, et al. The effect of source animal age upon extracellular matrix scaffold properties. *Biomaterials* 2011;32(1):128-36.
- [105] Turner NJ, Yates AJ, Jr., Weber DJ, Qureshi IR, Stolz DB, Gilbert TW, et al. Xenogeneic extracellular matrix as an inductive scaffold for regeneration of a functioning musculotendinous junction. *Tissue Eng Part A* 2010;16(11):3309-17.
- [106] Valentin JE, Badylak JS, McCabe GP, Badylak SF. Extracellular matrix bioscaffolds for orthopaedic applications. A comparative histologic study. *J Bone Joint Surg Am* 2006;88(12):2673-86.
- [107] Valentin JE, Turner NJ, Gilbert TW, Badylak SF. Functional skeletal muscle formation with a biologic scaffold. *Biomaterials* 2010;31(29):7475-84.
- [108] Wolf MT, Daly KA, Reing JE, Badylak SF. Biologic scaffold composed of skeletal muscle extracellular matrix. *Biomaterials* 2012;33(10):2916-25.
- [109] Zardo P, Zhang R, Wiegmann B, Haverich A, Fischer S. Biological materials for diaphragmatic repair: initial experiences with the PeriGuard Repair Patch(R). *Thorac Cardiovasc Surg* 2011;59(1):40-4.
- [110] Badylak S, Obermiller J, Geddes L, Matheny R. Extracellular matrix for myocardial repair. *Heart Surg Forum* 2003;6(2):E20-6.
- [111] Badylak SF, Kochupura PV, Cohen IS, Doronin SV, Saltman AE, Gilbert TW, et al. The use of extracellular matrix as an inductive scaffold for the partial replacement of functional myocardium. *Cell Transplant* 2006;15 Suppl 1:S29-40.
- [112] Kelly DJ, Rosen AB, Schuldt AJ, Kochupura PV, Doronin SV, Potapova IA, et al. Increased myocyte content and mechanical function within a tissue-engineered myocardial patch following implantation. *Tissue Eng Part A* 2009;15(8):2189-201.
- [113] Kochupura PV, Azeloglu EU, Kelly DJ, Doronin SV, Badylak SF, Krukenkamp IB, et al. Tissue-engineered myocardial patch derived from extracellular matrix provides regional mechanical function. *Circulation* 2005;112(9 Suppl):I144-9.
- [114] Okada M, Payne TR, Oshima H, Momoi N, Tobita K, Huard J. Differential efficacy of gels derived from small intestinal submucosa as an injectable biomaterial for myocardial infarct repair. *Biomaterials* 2010;31(30):7678-83.
- [115] Ota T, Gilbert TW, Badylak SF, Schwartzman D, Zenati MA. Electromechanical characterization of a tissue-engineered myocardial patch derived from extracellular matrix. *J Thorac Cardiovasc Surg* 2007;133(4):979-85.
- [116] Ota T, Gilbert TW, Schwartzman D, McTiernan CF, Kitajima T, Ito Y, et al. A fusion protein of hepatocyte growth factor enhances reconstruction of myocardium in a cardiac patch derived from porcine urinary bladder matrix. *J Thorac Cardiovasc Surg* 2008;136(5):1309-17.

- [117] Quarti A, Nardone S, Colaneri M, Santoro G, Pozzi M. Preliminary experience in the use of an extracellular matrix to repair congenital heart diseases. *Interact Cardiovasc Thorac Surg* 2011;(6):569-72.
- [118] Robinson KA, Li J, Mathison M, Redkar A, Cui J, Chronos NA, et al. Extracellular matrix scaffold for cardiac repair. *Circulation* 2005;112(9 Suppl):I135-43.
- [119] Scholl FG, Boucek MM, Chan K, Valdes-Cruz L, Perryman R. Preliminary Experience With Cardiac Reconstruction Using Decellularized Porcine Extracellular Matrix Scaffold Human Applications in Congenital Heart Disease. *World Journal for Pediatric and Congenital Heart Surgery* 2010;1(1):5.
- [120] Singelyn JM, DeQuach JA, Seif-Naraghi SB, Littlefield RB, Schup-Magoffin PJ, Christman KL. Naturally derived myocardial matrix as an injectable scaffold for cardiac tissue engineering. *Biomaterials* 2009;30(29):5409-16.
- [121] Singelyn JM, Sundaramurthy P, Johnson TD, Schup-Magoffin PJ, Hu DP, Faulk DM, et al. Catheter-deliverable hydrogel derived from decellularized ventricular extracellular matrix increases endogenous cardiomyocytes and preserves cardiac function post-myocardial infarction. *J Am Coll Cardiol* 2012;59(8):751-63.
- [122] Tan MY, Zhi W, Wei RQ, Huang YC, Zhou KP, Tan B, et al. Repair of infarcted myocardium using mesenchymal stem cell seeded small intestinal submucosa in rabbits. *Biomaterials* 2009;30(19):3234-40.
- [123] Wainwright JM, Hashizume R, Fujimoto KL, Remlinger NT, Pesyna C, Wagner WR, et al. Right ventricular outflow tract repair with a cardiac biologic scaffold. *Cells Tissues Organs* 2012;195(1-2):159-70.
- [124] Allman AJ, McPherson TB, Badylak SF, Merrill LC, Kallakury B, Sheehan C, et al. Xenogeneic extracellular matrix grafts elicit a TH2-restricted immune response. *Transplantation* 2001;71(11):1631-40.
- [125] Badylak SF, Gilbert TW. Immune response to biologic scaffold materials. *Semin Immunol* 2008;20(2):109-16.
- [126] Allman AJ, McPherson TB, Merrill LC, Badylak SF, Metzger DW. The Th2-restricted immune response to xenogeneic small intestinal submucosa does not influence systemic protective immunity to viral and bacterial pathogens. *Tissue Eng* 2002;8(1):53-62.
- [127] Badylak SF, Valentin JE, Ravindra AK, McCabe GP, Stewart-Akers AM. Macrophage phenotype as a determinant of biologic scaffold remodeling. *Tissue Eng Part A* 2008;14(11):1835-42.
- [128] Valentin JE, Stewart-Akers AM, Gilbert TW, Badylak SF. Macrophage participation in the degradation and remodeling of extracellular matrix scaffolds. *Tissue Eng Part A* 2009;15(7):1687-94.

- [129] Keane TJ, Londono R, Turner NJ, Badylak SF. Consequences of ineffective decellularization of biologic scaffolds on the host response. *Biomaterials* 2012;33(6):1771-81.
- [130] Gilbert TW, Freund JM, Badylak SF. Quantification of DNA in biologic scaffold materials. *J Surg Res* 2009;152(1):135-9.
- [131] Feola A, Barone W, Moalli P, Abramowitch S. Characterizing the ex vivo textile and structural properties of synthetic prolapse mesh products. *Int Urogynecol J* 2012.
- [132] Klosterhalfen B, Junge K, Klinge U. The lightweight and large porous mesh concept for hernia repair. *Expert Rev Med Devices* 2005;2(1):103-17.
- [133] Hernandez-Gascon B, Pena E, Melero H, Pascual G, Doblare M, Ginebra MP, et al. Mechanical behaviour of synthetic surgical meshes: finite element simulation of the herniated abdominal wall. *Acta Biomater* 2011;7(11):3905-13.
- [134] Chu CC, Welch L. Characterization of morphologic and mechanical properties of surgical mesh fabrics. *J Biomed Mater Res* 1985;19(8):903-16.
- [135] Cobb WS, Kercher KW, Heniford BT. The argument for lightweight polypropylene mesh in hernia repair. *Surg Innov* 2005;12(1):63-9.
- [136] Klinge U, Klosterhalfen B, Muller M, Schumpelick V. Foreign body reaction to meshes used for the repair of abdominal wall hernias. *Eur J Surg* 1999;165(7):665-73.
- [137] Di Vita G, D'Agostino P, Patti R, Arcara M, Caruso G, Davi V, et al. Acute inflammatory response after inguinal and incisional hernia repair with implantation of polypropylene mesh of different size. *Langenbecks Arch Surg* 2005;390(4):306-11.
- [138] Leber GE, Garb JL, Alexander AI, Reed WP. Long-term complications associated with prosthetic repair of incisional hernias. *Arch Surg* 1998;133(4):378-82.
- [139] Brown CN, Finch JG. Which mesh for hernia repair? *Ann R Coll Surg Engl* 2010;92(4):272-8.
- [140] Garcia-Urena MA, Vega Ruiz V, Diaz Godoy A, Baez Perea JM, Marin Gomez LM, Carnero Hernandez FJ, et al. Differences in polypropylene shrinkage depending on mesh position in an experimental study. *Am J Surg* 2007;193(4):538-42.
- [141] Costello CR, Bachman SL, Ramshaw BJ, Grant SA. Materials characterization of explanted polypropylene hernia meshes. *J Biomed Mater Res B Appl Biomater* 2007;83(1):44-9.
- [142] Brandt CJ, Kammer D, Fiebeler A, Klinge U. Beneficial effects of hydrocortisone or spironolactone coating on foreign body response to mesh biomaterial in a mouse model. *J Biomed Mater Res A* 2011;99(3):335-43.
- [143] Ansaloni L, Catena F, Coccolini F, Gazzotti F, D'Alessandro L, Pinna AD. Inguinal hernia repair with porcine small intestine submucosa: 3-year follow-up results of a randomized

controlled trial of Lichtenstein's repair with polypropylene mesh versus Surgisis Inguinal Hernia Matrix. *Am J Surg* 2009;198(3):303-12.

[144] Medberry CJ, Tottey S, Jiang H, Johnson SA, Badylak SF. Resistance to Infection of Five Different Materials in a Rat Body Wall Model. *J Surg Res* 2010.

[145] Holton LH, 3rd, Chung T, Silverman RP, Haerian H, Goldberg NH, Burrows WM, et al. Comparison of acellular dermal matrix and synthetic mesh for lateral chest wall reconstruction in a rabbit model. *Plast Reconstr Surg* 2007;119(4):1238-46.

[146] Hiles M, Record Ritchie RD, Altizer AM. Are biologic grafts effective for hernia repair?: a systematic review of the literature. *Surg Innov* 2009;16(1):26-37.

[147] Cortiella J, Niles J, Cantu A, Brettler A, Pham A, Vargas G, et al. Influence of acellular natural lung matrix on murine embryonic stem cell differentiation and tissue formation. *Tissue Eng Part A* 2010;16(8):2565-80.

[148] Sellaro TL, Ranade A, Faulk DM, McCabe GP, Dorko K, Badylak SF, et al. Maintenance of human hepatocyte function in vitro by liver-derived extracellular matrix gels. *Tissue Eng Part A* 2010;16(3):1075-82.

[149] Sellaro TL, Ravindra AK, Stolz DB, Badylak SF. Maintenance of hepatic sinusoidal endothelial cell phenotype in vitro using organ-specific extracellular matrix scaffolds. *Tissue Eng* 2007;13(9):2301-10.

[150] Zhang Y, He Y, Bharadwaj S, Hammam N, Carnagey K, Myers R, et al. Tissue-specific extracellular matrix coatings for the promotion of cell proliferation and maintenance of cell phenotype. *Biomaterials* 2009;30(23-24):4021-8.

[151] Ott HC, Matthiesen TS, Goh SK, Black LD, Kren SM, Netoff TI, et al. Perfusion-decellularized matrix: using nature's platform to engineer a bioartificial heart. *Nat Med* 2008;14(2):213-21.

[152] Cheng NC, Estes BT, Awad HA, Guilak F. Chondrogenic differentiation of adipose-derived adult stem cells by a porous scaffold derived from native articular cartilage extracellular matrix. *Tissue Eng Part A* 2009;15(2):231-41.

[153] Macchiarini P, Jungebluth P, Go T, Asnaghi MA, Rees LE, Cogan TA, et al. Clinical transplantation of a tissue-engineered airway. *Lancet* 2008;372(9655):2023-30.

[154] Schaner PJ, Martin ND, Tulenko TN, Shapiro IM, Tarola NA, Leichter RF, et al. Decellularized vein as a potential scaffold for vascular tissue engineering. *J Vasc Surg* 2004;40(1):146-53.

[155] Kuttan R, Spall RD, Duhamel RC, Sipes IG, Meezan E, Brendel K. Preparation and composition of alveolar extracellular matrix and incorporated basement membrane. *Lung* 1981;159(6):333-45.

- [156] Lwebuga-Mukasa JS, Ingbar DH, Madri JA. Repopulation of a human alveolar matrix by adult rat type II pneumocytes in vitro. A novel system for type II pneumocyte culture. *Exp Cell Res* 1986;162(2):423-35.
- [157] Shamis Y, Hasson E, Soroker A, Bassat E, Shimoni Y, Ziv T, et al. Organ-specific scaffolds for in vitro expansion, differentiation and organization of primary lung cells. *Tissue Eng Part C Methods* 2011.
- [158] Bonvillain RW, Danchuk S, Sullivan DE, Betancourt AM, Semon JA, Eagle ME, et al. A nonhuman primate model of lung regeneration: detergent-mediated decellularization and initial in vitro recellularization with mesenchymal stem cells. *Tissue Eng Part A* 2012;18(23-24):2437-52.
- [159] Jensen T, Roszell B, Zang F, Girard E, Matson A, Thrall R, et al. A rapid lung decellularization protocol supports embryonic stem cell differentiation in vitro and following implantation. *Tissue Eng Part C Methods* 2012;18(8):632-46.
- [160] Daly AB, Wallis JM, Borg ZD, Bonvillain RW, Deng B, Ballif BA, et al. Initial binding and recellularization of decellularized mouse lung scaffolds with bone marrow-derived mesenchymal stromal cells. *Tissue Eng Part A* 2012;18(1-2):1-16.
- [161] Bonenfant NR, Sokocevic D, Wagner DE, Borg ZD, Lathrop MJ, Lam YW, et al. The effects of storage and sterilization on de-cellularized and re-cellularized whole lung. *Biomaterials* 2013;34(13):3231-45.
- [162] Luque T, Melo E, Garreta E, Cortiella J, Nichols J, Farre R, et al. Local micromechanical properties of decellularized lung scaffolds measured with atomic force microscopy. *Acta Biomater* 2013;9(6):6852-9.
- [163] Longmire TA, Ikonomou L, Hawkins F, Christodoulou C, Cao Y, Jean JC, et al. Efficient derivation of purified lung and thyroid progenitors from embryonic stem cells. *Cell Stem Cell* 2012;10(4):398-411.
- [164] Price AP, England KA, Matson AM, Blazar BR, Panoskaltsis-Mortari A. Development of a decellularized lung bioreactor system for bioengineering the lung: the matrix reloaded. *Tissue Eng Part A* 2010;16(8):2581-91.
- [165] Song JJ, Kim SS, Liu Z, Madsen JC, Mathisen DJ, Vacanti JP, et al. Enhanced in vivo function of bioartificial lungs in rats. *Ann Thorac Surg* 2011;92(3):998-1005; discussion -6.
- [166] Hall S. Axonal regeneration through acellular muscle grafts. *J Anat* 1997;190 ( Pt 1):57-71.
- [167] Wang L, Johnson JA, Chang DW, Zhang Q. Decellularized musculofascial extracellular matrix for tissue engineering. *Biomaterials* 2013;34(11):2641-54.
- [168] Gillies AR, Smith LR, Lieber RL, Varghese S. Method for decellularizing skeletal muscle without detergents or proteolytic enzymes. *Tissue Eng Part C Methods* 2011;17(4):383-9.

- [169] London E, Khorana HG. Denaturation and renaturation of bacteriorhodopsin in detergents and lipid-detergent mixtures. *J Biol Chem* 1982;257(12):7003-11.
- [170] Otzen D. Protein-surfactant interactions: a tale of many states. *Biochim Biophys Acta* 2011;1814(5):562-91.
- [171] Gratzner PF, Harrison RD, Woods T. Matrix alteration and not residual sodium dodecyl sulfate cytotoxicity affects the cellular repopulation of a decellularized matrix. *Tissue Eng* 2006;12(10):2975-83.
- [172] Fishman JM, Ansari T, Sibbons P, De Coppi P, Birchall MA. Decellularized rabbit cricoarytenoid dorsalis muscle for laryngeal regeneration. *Ann Otol Rhinol Laryngol* 2012;121(2):129-38.
- [173] Fishman JM, Lowdell MW, Urbani L, Ansari T, Burns AJ, Turmaine M, et al. Immunomodulatory effect of a decellularized skeletal muscle scaffold in a discordant xenotransplantation model. *Proc Natl Acad Sci U S A* 2013;110(35):14360-5.
- [174] DeQuach JA, Lin JE, Cam C, Hu D, Salvatore MA, Sheikh F, et al. Injectable skeletal muscle matrix hydrogel promotes neovascularization and muscle cell infiltration in a hindlimb ischemia model. *Eur Cell Mater* 2012;23:400-12; discussion 12.
- [175] DeQuach JA, Mezzano V, Miglani A, Lange S, Keller GM, Sheikh F, et al. Simple and high yielding method for preparing tissue specific extracellular matrix coatings for cell culture. *PLoS One* 2010;5(9):e13039.
- [176] Chen XK, Walters TJ. Muscle-derived decellularised extracellular matrix improves functional recovery in a rat latissimus dorsi muscle defect model. *J Plast Reconstr Aesthet Surg* 2013;66(12):1750-8.
- [177] Wu X, Corona BT, Chen X, Walters TJ. A standardized rat model of volumetric muscle loss injury for the development of tissue engineering therapies. *Biores Open Access* 2012;1(6):280-90.
- [178] Corona BT, Wu X, Ward CL, McDaniel JS, Rathbone CR, Walters TJ. The promotion of a functional fibrosis in skeletal muscle with volumetric muscle loss injury following the transplantation of muscle-ECM. *Biomaterials* 2013;34(13):3324-35.
- [179] Wainwright JM, Czajka CA, Patel UB, Freytes DO, Tobita K, Gilbert TW, et al. Preparation of Cardiac Extracellular Matrix from an Intact Porcine Heart. *Tissue Eng Part C Methods* 2009.
- [180] Sarig U, Au-Yeung GC, Wang Y, Bronshtein T, Dahan N, Boey FY, et al. Thick acellular heart extracellular matrix with inherent vasculature: a potential platform for myocardial tissue regeneration. *Tissue Eng Part A* 2012;18(19-20):2125-37.
- [181] Akhyari P, Aubin H, Gwanmesia P, Barth M, Hoffmann S, Huelsmann J, et al. The quest for an optimized protocol for whole-heart decellularization: a comparison of three popular and a

novel decellularization technique and their diverse effects on crucial extracellular matrix qualities. *Tissue Eng Part C Methods* 2011;17(9):915-26.

[182] Witzenburg C, Raghupathy R, Kren SM, Taylor DA, Barocas VH. Mechanical changes in the rat right ventricle with decellularization. *J Biomech* 2012;45(5):842-9.

[183] Schulte JB, Simionescu A, Simionescu DT. The acellular myocardial flap: a novel extracellular matrix scaffold enriched with patent microvascular networks and biocompatible cell niches. *Tissue Eng Part C Methods* 2013;19(7):518-30.

[184] Wang B, Borazjani A, Tahai M, Curry AL, Simionescu DT, Guan J, et al. Fabrication of cardiac patch with decellularized porcine myocardial scaffold and bone marrow mononuclear cells. *J Biomed Mater Res A* 2010;94(4):1100-10.

[185] Wang B, Tedder ME, Perez CE, Wang G, de Jongh Curry AL, To F, et al. Structural and biomechanical characterizations of porcine myocardial extracellular matrix. *J Mater Sci Mater Med* 2012;23(8):1835-47.

[186] Oberwallner B, Brodarac A, Choi YH, Saric T, Anic P, Morawietz L, et al. Preparation of cardiac extracellular matrix scaffolds by decellularization of human myocardium. *J Biomed Mater Res A* 2013.

[187] Dai W, Gerczuk P, Zhang Y, Smith L, Kopyov O, Kay GL, et al. Intramyocardial injection of heart tissue-derived extracellular matrix improves postinfarction cardiac function in rats. *J Cardiovasc Pharmacol Ther* 2013;18(3):270-9.

[188] Eitan Y, Sarig U, Dahan N, Machluf M. Acellular cardiac extracellular matrix as a scaffold for tissue engineering: in vitro cell support, remodeling, and biocompatibility. *Tissue Eng Part C Methods* 2010;16(4):671-83.

[189] Duan Y, Liu Z, O'Neill J, Wan LQ, Freytes DO, Vunjak-Novakovic G. Hybrid gel composed of native heart matrix and collagen induces cardiac differentiation of human embryonic stem cells without supplemental growth factors. *J Cardiovasc Transl Res* 2011;4(5):605-15.

[190] Lu TY, Lin B, Kim J, Sullivan M, Tobita K, Salama G, et al. Repopulation of decellularized mouse heart with human induced pluripotent stem cell-derived cardiovascular progenitor cells. *Nat Commun* 2013;4:2307.

[191] Singelyn JM, Christman KL. Modulation of material properties of a decellularized myocardial matrix scaffold. *Macromol Biosci* 2011;11(6):731-8.

[192] Seif-Naraghi SB, Singelyn JM, Salvatore MA, Osborn KG, Wang JJ, Sampat U, et al. Safety and efficacy of an injectable extracellular matrix hydrogel for treating myocardial infarction. *Sci Transl Med* 2013;5(173):173ra25.

[193] Manni ML, Czajka CA, Oury TD, Gilbert TW. Extracellular matrix powder protects against bleomycin-induced pulmonary fibrosis. *Tissue Eng Part A* 2011;17(21-22):2795-804.

- [194] Badylak SF, Lantz GC, Coffey A, Geddes LA. Small intestinal submucosa as a large diameter vascular graft in the dog. *J Surg Res* 1989;47(1):74-80.
- [195] Turner NJ, Badylak JS, Weber DJ, Badylak SF. Biologic scaffold remodeling in a dog model of complex musculoskeletal injury. *J Surg Res* 2012;176(2):490-502.
- [196] Brown BN, Londono R, Tottey S, Zhang L, Kukla KA, Wolf MT, et al. Macrophage phenotype as a predictor of constructive remodeling following the implantation of biologically derived surgical mesh materials. *Acta Biomater* 2012;8(3):978-87.
- [197] Brown BN, Valentin JE, Stewart-Akers AM, McCabe GP, Badylak SF. Macrophage phenotype and remodeling outcomes in response to biologic scaffolds with and without a cellular component. *Biomaterials* 2009;30(8):1482-91.
- [198] Corona BT, Machingal MA, Criswell T, Vadhavkar M, Dannahower AC, Bergman C, et al. Further development of a tissue engineered muscle repair construct in vitro for enhanced functional recovery following implantation in vivo in a murine model of volumetric muscle loss injury. *Tissue Eng Part A* 2012;18(11-12):1213-28.
- [199] Machingal MA, Corona BT, Walters TJ, Kesireddy V, Koval CN, Dannahower A, et al. A tissue-engineered muscle repair construct for functional restoration of an irrecoverable muscle injury in a murine model. *Tissue Eng Part A* 2011;17(17-18):2291-303.
- [200] Corona BT, Ward CL, Baker HB, Walters TJ, Christ GJ. Implantation of in vitro tissue engineered muscle repair (TEMR) constructs and bladder acellular matrices (BAM) partially restore in vivo skeletal muscle function in a rat model of volumetric muscle loss (VML) injury. *Tissue Eng Part A* 2013.
- [201] Toeg HD, Tiwari-Pandey R, Seymour R, Ahmadi A, Crowe S, Vulesevic B, et al. Injectable small intestine submucosal extracellular matrix in an acute myocardial infarction model. *Ann Thorac Surg* 2013;96(5):1686-94.
- [202] Remlinger NT, Wearden PD, Gilbert TW. Procedure for decellularization of porcine heart by retrograde coronary perfusion. *J Vis Exp* 2012;(70):e50059.
- [203] Remlinger NT, Gilbert TW, Yoshida M, Guest BN, Hashizume R, Weaver ML, et al. Urinary bladder matrix promotes site appropriate tissue formation following right ventricle outflow tract repair. *Organogenesis* 2013;9(3):149-60.
- [204] Mase VJ, Jr., Hsu JR, Wolf SE, Wenke JC, Baer DG, Owens J, et al. Clinical application of an acellular biologic scaffold for surgical repair of a large, traumatic quadriceps femoris muscle defect. *Orthopedics* 2010;33(7):511.
- [205] Wyler von Ballmoos M, Murtaza G, Gasparri M, Masroor S. Reconstruction of the right atrium using an extracellular matrix patch in a patient with severe mediastinal aspergillosis. *Int J Surg Case Rep* 2013;4(3):290-2.

- [206] Stelly M, Stelly TC. Histology of CorMatrix Bioscaffold 5 Years After Pericardial Closure. *Ann Thorac Surg* 2013;96(5):e127-9.
- [207] Badylak SF. The extracellular matrix as a biologic scaffold material. *Biomaterials* 2007;28(25):3587-93.
- [208] Song JJ, Ott HC. Organ engineering based on decellularized matrix scaffolds. *Trends Mol Med* 2011;17(8):424-32.
- [209] Boruch AV, Nieponice A, Qureshi IR, Gilbert TW, Badylak SF. Constructive Remodeling of Biologic Scaffolds is Dependent on Early Exposure to Physiologic Bladder Filling in a Canine Partial Cystectomy Model. *J Surg Res* 2009;161(2):217-25.
- [210] Beattie AJ, Gilbert TW, Guyot JP, Yates AJ, Badylak SF. Chemoattraction of progenitor cells by remodeling extracellular matrix scaffolds. *Tissue Eng Part A* 2009;15(5):1119-25.
- [211] Reing JE, Zhang L, Myers-Irvin J, Cordero KE, Freytes DO, Heber-Katz E, et al. Degradation products of extracellular matrix affect cell migration and proliferation. *Tissue Eng Part A* 2009;15(3):605-14.
- [212] Vorotnikova E, McIntosh D, Dewilde A, Zhang J, Reing JE, Zhang L, et al. Extracellular matrix-derived products modulate endothelial and progenitor cell migration and proliferation in vitro and stimulate regenerative healing in vivo. *Matrix Biol* 2010;29(8):690-700.
- [213] Petersen TH, Calle EA, Zhao L, Lee EJ, Gui L, Raredon MB, et al. Tissue-engineered lungs for in vivo implantation. *Science* 2010;329(5991):538-41.
- [214] Stern MM, Myers RL, Hammam N, Stern KA, Eberli D, Kritchevsky SB, et al. The influence of extracellular matrix derived from skeletal muscle tissue on the proliferation and differentiation of myogenic progenitor cells ex vivo. *Biomaterials* 2009;30(12):2393-9.
- [215] Kurihara T, Nishizawa Y, Takahashi Y. The use of non-aqueous chloroform/methanol extraction for the delipidation of brain with minimal loss of enzyme activities. *Biochem J* 1977;165(1):135-40.
- [216] Lantz GC, Badylak SF, Coffey AC, Geddes LA, Sandusky GE. Small intestinal submucosa as a superior vena cava graft in the dog. *J Surg Res* 1992;53(2):175-81.
- [217] Crisan M, Yap S, Casteilla L, Chen CW, Corselli M, Park TS, et al. A perivascular origin for mesenchymal stem cells in multiple human organs. *Cell Stem Cell* 2008;3(3):301-13.
- [218] Sicari BM, Johnson SA, Siu BF, Crapo PM, Daly KA, Jiang H, et al. The effect of source animal age upon the in vivo remodeling characteristics of an extracellular matrix scaffold. *Biomaterials* 2012;33(22):5524-33.
- [219] Jarvinen TA, Jozsa L, Kannus P, Jarvinen TL, Jarvinen M. Organization and distribution of intramuscular connective tissue in normal and immobilized skeletal muscles. *An*

immunohistochemical, polarization and scanning electron microscopic study. *J Muscle Res Cell Motil* 2002;23(3):245-54.

[220] Light N, Champion AE. Characterization of muscle epimysium, perimysium and endomysium collagens. *Biochem J* 1984;219(3):1017-26.

[221] Fuchs E, Tumber T, Guasch G. Socializing with the neighbors: stem cells and their niche. *Cell* 2004;116(6):769-78.

[222] Hodde J, Janis A, Ernst D, Zopf D, Sherman D, Johnson C. Effects of sterilization on an extracellular matrix scaffold: part I. Composition and matrix architecture. *J Mater Sci Mater Med* 2007;18(4):537-43.

[223] Voytik-Harbin SL, Brightman AO, Kraine MR, Waisner B, Badylak SF. Identification of extractable growth factors from small intestinal submucosa. *J Cell Biochem* 1997;67(4):478-91.

[224] Hodde JP, Record RD, Liang HA, Badylak SF. Vascular endothelial growth factor in porcine-derived extracellular matrix. *Endothelium* 2001;8(1):11-24.

[225] Li S, Edgar D, Fassler R, Wadsworth W, Yurchenco PD. The role of laminin in embryonic cell polarization and tissue organization. *Dev Cell* 2003;4(5):613-24.

[226] Sanes JR. Laminin, fibronectin, and collagen in synaptic and extrasynaptic portions of muscle fiber basement membrane. *J Cell Biol* 1982;93(2):442-51.

[227] Hudson BG, Reeders ST, Tryggvason K. Type IV collagen: structure, gene organization, and role in human diseases. Molecular basis of Goodpasture and Alport syndromes and diffuse leiomyomatosis. *J Biol Chem* 1993;268(35):26033-6.

[228] Sanes JR. The basement membrane/basal lamina of skeletal muscle. *J Biol Chem* 2003;278(15):12601-4.

[229] Hodde JP, Badylak SF, Brightman AO, Voytik-Harbin SL. Glycosaminoglycan content of small intestinal submucosa: a bioscaffold for tissue replacement. *Tissue Eng* 1996;2(3):209-17.

[230] Langsdorf A, Do AT, Kusche-Gullberg M, Emerson CP, Jr., Ai X. Sulfs are regulators of growth factor signaling for satellite cell differentiation and muscle regeneration. *Dev Biol* 2007;311(2):464-77.

[231] Derwin KA, Badylak SF, Steinmann SP, Iannotti JP. Extracellular matrix scaffold devices for rotator cuff repair. *J Shoulder Elbow Surg* 2010;19(3):467-76.

[232] Zantop T, Gilbert TW, Yoder MC, Badylak SF. Extracellular matrix scaffolds are repopulated by bone marrow-derived cells in a mouse model of achilles tendon reconstruction. *J Orthop Res* 2006;24(6):1299-309.

- [233] Deeken CR, Melman L, Jenkins ED, Greco SC, Frisella MM, Matthews BD. Histologic and biomechanical evaluation of crosslinked and non-crosslinked biologic meshes in a porcine model of ventral incisional hernia repair. *J Am Coll Surg* 2011;212(5):880-8.
- [234] Zhang J, Wang GY, Xiao YP, Fan LY, Wang Q. The biomechanical behavior and host response to porcine-derived small intestine submucosa, pericardium and dermal matrix acellular grafts in a rat abdominal defect model. *Biomaterials* 2011;32(29):7086-95.
- [235] Bellows CF, Albo D, Berger DH, Awad SS. Abdominal wall repair using human acellular dermis. *Am J Surg* 2007;194(2):192-8.
- [236] Perez-Garcia A, del Mar Luis-Hidalgo M, Perales-Puchalt A. The effects of acellular dermal matrix in expander-implant breast reconstruction after total skin-sparing mastectomy. *Plast Reconstr Surg* 2013;131(2):278e-9e.
- [237] Billiar KL, Sacks MS. Biaxial mechanical properties of the native and glutaraldehyde-treated aortic valve cusp: Part II--A structural constitutive model. *J Biomech Eng* 2000;122(4):327-35.
- [238] Record RD, Hillegonds D, Simmons C, Tullius R, Rickey FA, Elmore D, et al. In vivo degradation of <sup>14</sup>C-labeled small intestinal submucosa (SIS) when used for urinary bladder repair. *Biomaterials* 2001;22(19):2653-9.
- [239] Wynn TA. Cellular and molecular mechanisms of fibrosis. *J Pathol* 2008;214(2):199-210.
- [240] Brown B, Lindberg K, Reing J, Stolz DB, Badylak SF. The basement membrane component of biologic scaffolds derived from extracellular matrix. *Tissue Eng* 2006;12(3):519-26.
- [241] Reing JE, Brown BN, Daly KA, Freund JM, Gilbert TW, Hsiong SX, et al. The effects of processing methods upon mechanical and biologic properties of porcine dermal extracellular matrix scaffolds. *Biomaterials* 2010;31(33):8626-33.
- [242] Seif-Naraghi SB, Horn D, Schup-Magoffin PA, Madani MM, Christman KL. Patient-to-patient variability in autologous pericardial matrix scaffolds for cardiac repair. *J Cardiovasc Transl Res* 2011;4(5):545-56.
- [243] Mott JD, Werb Z. Regulation of matrix biology by matrix metalloproteinases. *Curr Opin Cell Biol* 2004;16(5):558-64.
- [244] Davis GE, Bayless KJ, Davis MJ, Meininger GA. Regulation of tissue injury responses by the exposure of matricryptic sites within extracellular matrix molecules. *Am J Pathol* 2000;156(5):1489-98.
- [245] Agrawal V, Tottey S, Johnson SA, Freund JM, Siu BF, Badylak SF. Recruitment of progenitor cells by an extracellular matrix cryptic peptide in a mouse model of digit amputation. *Tissue Eng Part A* 2011;17(19-20):2435-43.

- [246] Agrawal V, Kelly J, Tottey S, Daly KA, Johnson SA, Siu BF, et al. An isolated cryptic peptide influences osteogenesis and bone remodeling in an adult mammalian model of digit amputation. *Tissue Eng Part A* 2011;17(23-24):3033-44.
- [247] Dellavalle A, Maroli G, Covarello D, Azzoni E, Innocenzi A, Perani L, et al. Pericytes resident in postnatal skeletal muscle differentiate into muscle fibres and generate satellite cells. *Nat Commun* 2011;2:499.
- [248] Gerlach JC, Over P, Turner ME, Thompson RL, Foka HG, Chen WC, et al. Perivascular mesenchymal progenitors in human fetal and adult liver. *Stem Cells Dev* 2012;21(18):3258-69.
- [249] Petter-Puchner AH, Fortelny RH, Walder N, Mittermayr R, Ohlinger W, van Griensven M, et al. Adverse effects associated with the use of porcine cross-linked collagen implants in an experimental model of incisional hernia repair. *J Surg Res* 2008;145(1):105-10.
- [250] DeQuach JA, Yuan SH, Goldstein LS, Christman KL. Decellularized porcine brain matrix for cell culture and tissue engineering scaffolds. *Tissue Eng Part A* 2011;17(21-22):2583-92.
- [251] Brennan EP, Tang XH, Stewart-Akers AM, Gudas LJ, Badylak SF. Chemoattractant activity of degradation products of fetal and adult skin extracellular matrix for keratinocyte progenitor cells. *J Tissue Eng Regen Med* 2008;2(8):491-8.
- [252] Clause KC, Tchao J, Powell MC, Liu LJ, Huard J, Keller BB, et al. Developing cardiac and skeletal muscle share fast-skeletal myosin heavy chain and cardiac troponin-I expression. *PLoS One* 2012;7(7):e40725.
- [253] Seif-Naraghi SB, Salvatore MA, Schup-Magoffin PJ, Hu DP, Christman KL. Design and characterization of an injectable pericardial matrix gel: a potentially autologous scaffold for cardiac tissue engineering. *Tissue Eng Part A* 2010;16(6):2017-27.
- [254] Lin P, Chan WC, Badylak SF, Bhatia SN. Assessing porcine liver-derived biomatrix for hepatic tissue engineering. *Tissue Eng* 2004;10(7-8):1046-53.
- [255] Petersen TH, Calle EA, Colehour MB, Niklason LE. Bioreactor for the LongTerm Culture of Lung Tissue. *Cell Transplant* 2010;20(7):1117-26.
- [256] Bibbo C. The porcine small intestinal submucosa (SIS) patch in foot and ankle reconstruction. *J Foot Ankle Surg* 2010;49(2):123-7.
- [257] Freytes DO, Badylak SF, Webster TJ, Geddes LA, Rundell AE. Biaxial strength of multilaminated extracellular matrix scaffolds. *Biomaterials* 2004;25(12):2353-61.
- [258] Brown BN, Barnes CA, Kasick RT, Michel R, Gilbert TW, Beer-Stolz D, et al. Surface characterization of extracellular matrix scaffolds. *Biomaterials* 2010;31(3):428-37.
- [259] Klimstra M, Zehr EP. A sigmoid function is the best fit for the ascending limb of the Hoffmann reflex recruitment curve. *Exp Brain Res* 2008;186(1):93-105.

- [260] Stein RB, Estabrooks KL, McGie S, Roth MJ, Jones KE. Quantifying the effects of voluntary contraction and inter-stimulus interval on the human soleus H-reflex. *Exp Brain Res* 2007;182(3):309-19.
- [261] Bryant SJ, Anseth KS. Hydrogel properties influence ECM production by chondrocytes photoencapsulated in poly(ethylene glycol) hydrogels. *J Biomed Mater Res* 2002;59(1):63-72.
- [262] Van Vlierberghe S, Dubruel P, Schacht E. Biopolymer-based hydrogels as scaffolds for tissue engineering applications: a review. *Biomacromolecules* 2011;12(5):1387-408.
- [263] Tibbitt MW, Anseth KS. Hydrogels as extracellular matrix mimics for 3D cell culture. *Biotechnol Bioeng* 2009;103(4):655-63.
- [264] Freytes DO, Martin J, Velankar SS, Lee AS, Badylak SF. Preparation and rheological characterization of a gel form of the porcine urinary bladder matrix. *Biomaterials* 2008;29(11):1630-7.
- [265] Hong Y, Huber A, Takanari K, Amoroso NJ, Hashizume R, Badylak SF, et al. Mechanical properties and in vivo behavior of a biodegradable synthetic polymer microfiber-extracellular matrix hydrogel biohybrid scaffold. *Biomaterials* 2011;32(13):3387-94.
- [266] Young DA, Ibrahim DO, Hu D, Christman KL. Injectable hydrogel scaffold from decellularized human lipoaspirate. *Acta Biomater* 2011;7(3):1040-9.
- [267] Nagao RJ, Lundy S, Khaing ZZ, Schmidt CE. Functional characterization of optimized acellular peripheral nerve graft in a rat sciatic nerve injury model. *Neurol Res* 2011;33(6):600-8.
- [268] Stankus JJ, Freytes DO, Badylak SF, Wagner WR. Hybrid nanofibrous scaffolds from electrospinning of a synthetic biodegradable elastomer and urinary bladder matrix. *J Biomater Sci Polym Ed* 2008;19(5):635-52.